A PHENOMENOLOGICAL MODEL OF THE UNSTABLE PLANETARY BOUNDARY LAYER

by

David William Heinold

B.S., Fairleigh Dickinson University

(1973)

M.S., State University of New YOrk at Albany

(1975)

Submitted in partial fulfillment of the

requirements for the degree of

MASTER OF SCIENCE

at the

MASSACHUSETTS INSTITUTE OF TECHNOLOGY

August, 1978

Signature of Author ....
Department of Meteorology, 11 August, 1978

Certified by .....
Thesis Supervisor

Accepted by .....
Lindgren Chairman, Departmental Committee

A PHENOMENOLOGICAL MODEL OF THE UNSTABLE PLANETARY BOUNDARY LAYER

By

David William Heinold

Submitted to the Department of Meteorology on August 11, 1978 in partial fulfillment of the requirements for the degree of Master of Science.

ABSTRACT

The planetary boundary layer during periods of strong surface heating is characterized by plume-type elements hundreds of meters in diameter. By simulating the major aspects of these heat and momentum transporting eddies, a straightforward boundary layer parameterization is formulated. Two plume models developed by Manton (1975, 1976) are adapted to simulate the vertical heat transport from the surface to the inversion. Forms for the mechanical stresses are obtained from the moment-closure model of Wyngaard, et. al., (1974). Various features of the mean boundary layer, fluxes, and the individual plumes are diagnosed in addition to the boundary layer heating rate and inversion rise rate.

The model is applied to the Wangara Day 33 (Clarke, et. al., 1971) data. The model output compared favorably to observations and calculations from Deardorff's (1974) three-dimensional numerical model and Wyngaard and Cote's (1974) moment-closure model. The shortcomings of the present formulation point to the need for a more refined shear stress parameterization and a physically realistic closure for the mean stability. Possible improvements to the model are suggested to enhance verification with observations without significantly decreasing the utility.

Thesis Supervisor: Erik Mollo-Christensen
Title: Professor of Oceanography

ACKNOWLEDGEMENTS

In the course of my studies at Massachusetts Institute of Technology there are many people who have contributed to my "education". I would like to thank Professor Erik Mollo-Christensen for suggesting this topic and providing encouragement and insight during these past several months. Many helpful discussions and words of encouragement were also provided by Lee Branscome. Thanks also go to Isabelle Kole who deftly drafted the figures. Above all I extend love and appreciation to my wife Jerilyn who not only typed the manuscript but who has been my source of inspiration throughout my graduate career.

This research has been undertaken with the support of grants NSF 6-76-20070 ATM and NSFgDES 7424405.

TABLE OF CONTENTS

LIST OF FIGURES

INTRODUCTION

Theoretical investigations of the planetary boundary layer which began several decades past with Prandtl's mixing length theory have progressed to three dimensional numerical simulations. The complexity of turbulence under various degrees of surface heating and cooling through the diurnal cycle make a general similarity theory for the entire boundary layer quite elusive. The demand for horizontal homogeneity and stationarity implies that the turbulent mechanism has a response time short in comparison to advective or local changes. Figure 1 displays the diurnal cycle showing the growth and decay of the unstable surface layer and the rapid transition to a low level inversion during the first few hours of darkness. Kuo and Sun (1976) find that their two-dimensional numerical model equilibrates in approximately 10 minutes such that the atmospheric turbulence is always in step with diurnal variations. Therefore, except p rhaps during the abrupt convective breakdown shown at 2000 LST the local boundary conditions determine the state of the boundary layer.

K theory is based upon the unfounded principle that turbulent transport, of a quantity, like molecular diffusion, occurs in response to a gradient of that quantity. Because turbulence may be driven by an instability that is not directly related to the local mean gradient of that quantity, "negative viscosity" phenomena are common in geophysical turbulence. By letting the transport coefficients vary with height, the mean wind

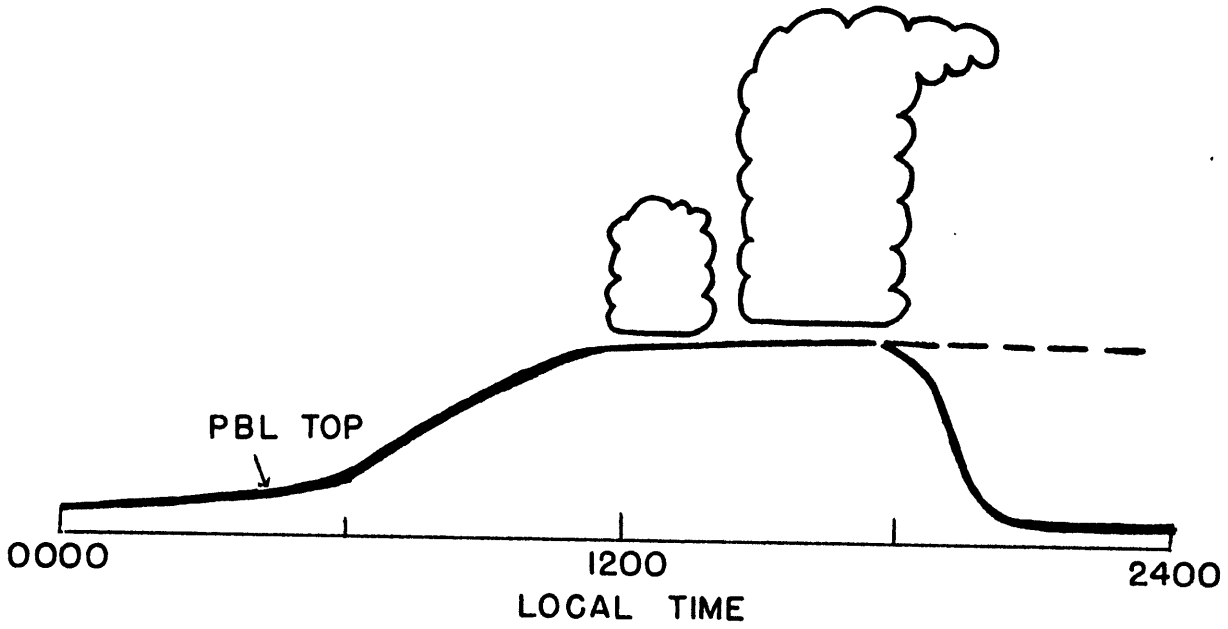

Figure 1. Diurnal variation of the depth of the planetary boundary layer (from Randall, 1976).

profiles under various stability conditions can be duplicated. Even though the artificiality of this method is obvious, it can be easily incorporated into any numerical prediction model that is unaffected by the nature of the turbulence or its transports.

While Monin-Obukov similarity theory has been successful within the surface layer, the extension to the entire mixed Ekman layer does not bear up to close scrutiny (Tennekes, 1973). For the unstable mixed layer the slab-symetric models offer a logical alternative, and they have been utilized in planetary and meso-scale weather prediction models. A surface layer with constant stress and heat flux is capped by a layer of uniform mean velocity, heating rate, and stress gradient extending to an elevated inversion. These simple and reasonable assumptions allow the model to incorporate various interactions with the free atmosphere such as stratus clouds (Randall, 1976), cumulus c. oud roots (Stuart, 1977), and entrainment (Stull, 1975). Such mixed layer models, however expedient, provide little insight into the nature of the turbulent elements that cause the fluxes that are modeled. Weather prediction models that utilize only the bulk properties of the planetary boundary layer find the slab-type parameterization to be superior to K theory.

By employing suitable closure assumptions on the third order moments, the flux profiles can be determined. The moment closure models of Wyngaard et. al. (1974) and Yamada and Mellor (1975) show considerable success in simulating the mean features

of the boundary layer observed during the Wangara Experiment (Clark et. al., 1971). Verification of the momentum flux profiles remains a problem, because the few available measurements in the mixed layer are insufficiently accurate. Although this method involves considerable effort and computation time, it is simultaneously more efficient and elegant than brute-force, direct numerical simulation. The constants required by the closure schemes (Donaldson, 1973), are difficult to determine experimentally and the vertical resolution near the surface and the inversion must be sufficient to resolve near discontinuities in temperature and velocity. Apparently, the theory must wait for the observations to approach the same precision as afforded by moment closure models.

Direct three dimensional simulation is most useful as a tool to investigate the real nature of the atmospheric turbulence as well as its statistical properties. The underlying assumptions become increasingly obscure as the models "progress" but they still affect the solution in subtle ways. For instance, a horizontal grid mesh of 100 meters requires a sophisticated sub-grid scale subroutine, while similarity theory is unjustifyably used to compute the instantaneous surface stress. Also, periodic boundary conditions produce an obviously artificial scale selection in fractions of 2.5 kilometers. In light of the absence of comparable observational detail this costly exercise provides a measure against which to test less fundamental parameterizations.

Following the suggestion by Howard (1964) to incorporate

the phenomenological aspects of the turbulent elements into a thermal boundary layer parameterization, I propose a thermal plume representation. Several of the observed features of atmospheric convection are supplemented by results gleaned from the more sophisticated simulations described previously. The model produces the vertical profiles of the mean wind, virtual potential temperature, average plume vertical and horizontal velocities, and temperature perturbations. These in turn predict the vertical fluxes of heat and momentum, plume translation velocity and intermittency mixed layer heating rate, inversion strengthening rate, and rate of increase of boundary layer depth. The strength of the formulation lies in its straightforward assumptions, analytical solutions, agreement with observations and flexibility in light of better plume data. While a detailed description of properties of the turbulent eddies may not be essential to large-scale numerical simulations, this model may provide a link to the initiation of fair weather cumulus which form when energetic eddies are able to protrude an inversion to the lifting condensation level. On a local level, the scale of the wind variability is indicated by the distribution of plumes and their momentum deficit. Atmospheric diffusion under unstable conditions may be studied by computing the trajectories of an array of tagged parcels (ingested into an idealized plume array) emitted from sources of various configurations. The model is not intended to compete in rigorous pursuit of the true nature of the unstable

planetary boundary layer but it offers significant information on both the bulk and elemental properties while requiring a relatively modest effort.

CHAPTER I

THE NATURE OF BUOYANT THERMAL ELEMENTS

Turbulent shear flows over a range of Reynold's numbers are dominated by large eddy-type structures which develop and interact in a highly non-linear fashion. Eddies within heated jets and atmospheric boundary layers display a similar "saw-tooth" temperature trace as shown in Figure 2. The plume concept developed by Priestly (1959) has been identified as a geophysical manifestation of a turbulent burst. Consequently, Antonia (1977) has found that the atmospheric burst-sweep cycle measured a few meters above a wheat canopy is remarkably similar to the laboratory phenomenon. Table 1 (Antonia, 1977) shows the occupancy time and stress contribution of four types of air motion: I. outward interaction, II. burst, III. wall-ward interaction, and IV. sweep. It is noteworthy that the plume ($w' > 0$, $\theta' > 0$) and environment ($w' < 0$, $\theta' > 0$) are the dominant modes of momentum and heat transport. The negatively contributing interaction evants which are observed to be less organized and of a considerably smaller scale can be conceived of as the entraining eddies at the downwind plume- environment interface. Figure 2 illustrates the ramp-like temperature structure forming as the plume translates with a elevated "steering level". The forward edge undergoes continual mixing with the environment, while the most buoyant surface air accelerates upward. Near the rear of the plume a temperature

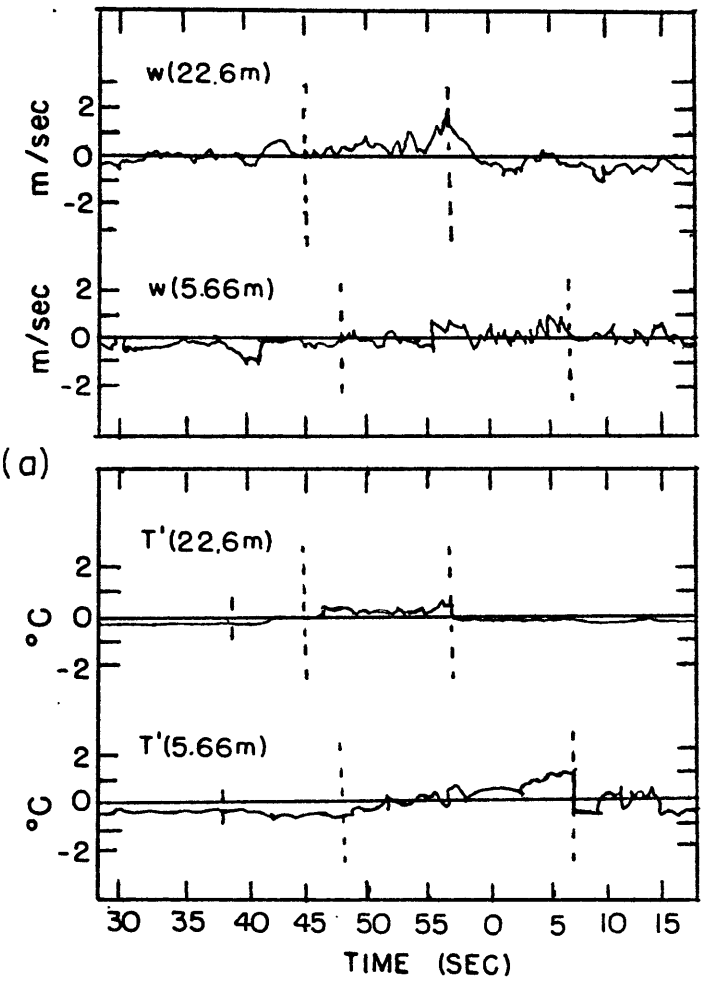

Figure 2.
a) The temporal traces of vertical velocity and temperature during a plume passage.

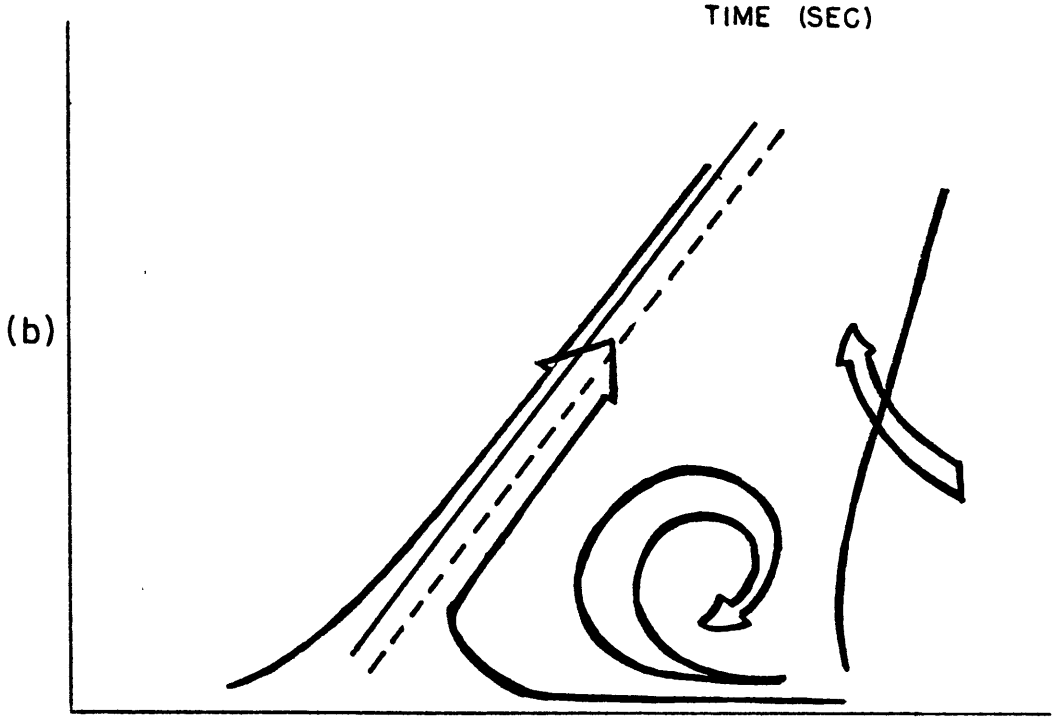

Figure 2.
b) A schematic of lower plume structure (from Kaimal and Businger, 1970).

TABLE 1

Contribution of bursts, sweeps, and interaction terms to heat flux and momentum stress near a heated planetary surface

	Quadrant:	I	II	III	IV
Stress	(x y)	$x > 0, y > 0$	$x < 0, y > 0$	$x < 0, y < 0$	$x > 0, y < 0$
contribution	u w	-15.4	66.7	-18	66.7
(percent)	u θ	-44	72	-20	92
	$-\theta$ w	-26.9	76.9	-34.6	84.6
Occupancy	u w	.17	.32	.16	.35
time	u θ	.23	.31	.16	.30
	$-\theta$ w	.17	.32	.22	.29
		outward interaction	burst	wallward interaction	sweep

discontinuity develops. The plume region contains much more turbulent kinetic energy on sub-plume scales than the environment. Khalsa and Businger (1977) have successfully used this criterion to selectively sample plume versus environmental properties in the trade-wind boundary layer. Figures 3 and 4 are a summary of findings for slightly, moderately and highly unstable surface layers. The presence of interaction events and the sampling technique are responsible for the overlapping between the plume and environment. The typical plume has a high turbulent energy due to rising parcels of heated air. Near the surface the parcels in the plume updraft have a significant momentum deficit. Manton (1977) finds that in the lower mixed layer ($z < 100$ m) that plume-scale motions ($l \sim 100$ m) account for 70 percent of the total heat flux. The remainder is a result of the turbulent bubbles that Ting and Hay (1977) have observed to be the members of the plume family. The predominance of sub-plume scales is indicated by Figure 5.

Although plumes appear to be vertically contiguous for several hundred meters, their life span as witnessed by radar and glider pilots does not exceed several minutes. A configuration of close-packed thermal elements is demonstrated in Figure 6 which is the streamfunction from a two-dimensional model by Kuo and Sun (1976). Since atmospheric plumes do not occur in isolation, they become elongated as the familiar circular vortex ring circulation becomes distorted vertically. Konrad (1970) is able to detect the upper levels of plumes

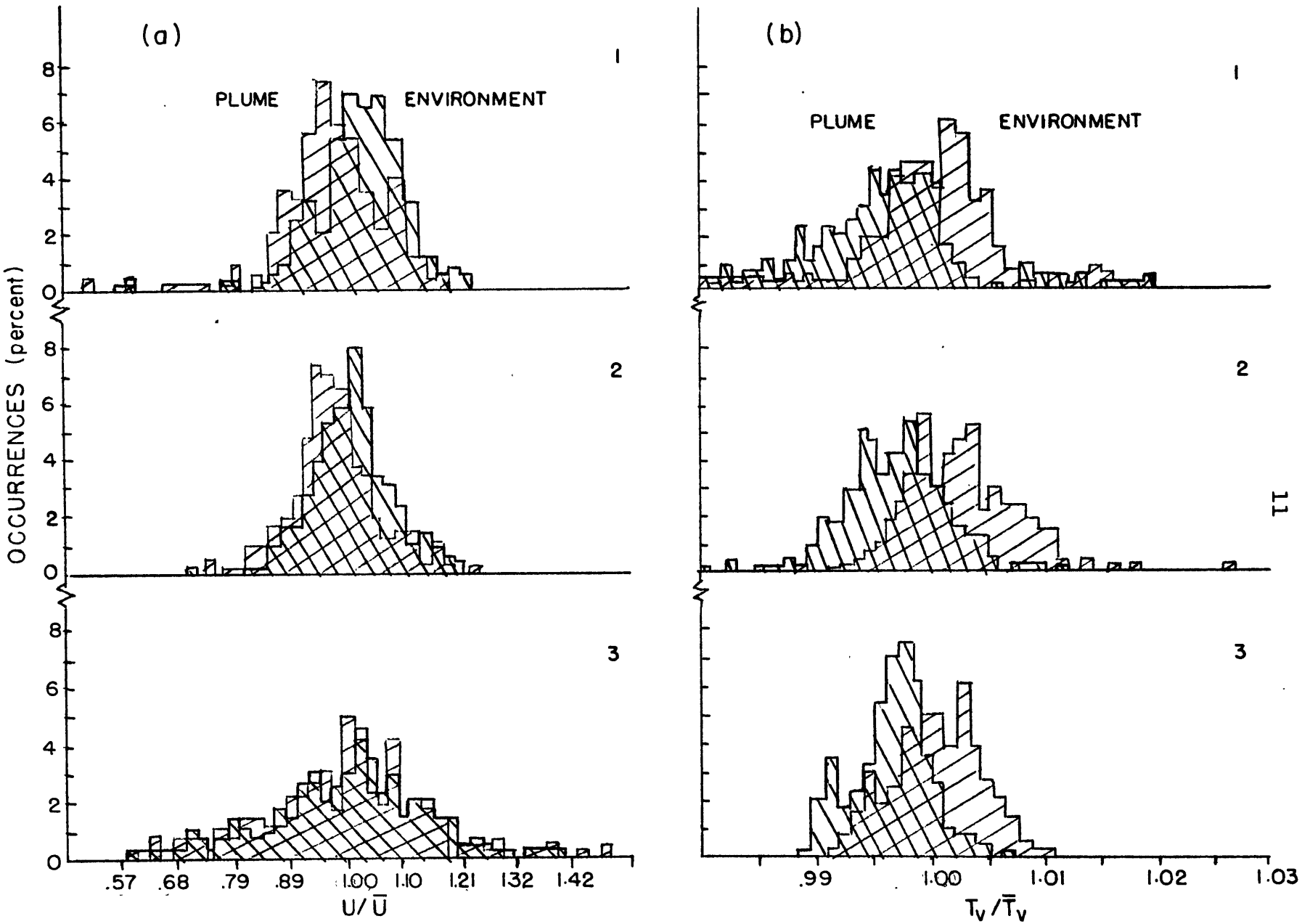

Figure 3. Frequency distributions of a) normalized wind speed and b) virtual temperature for slightly,1; moderately, 2; and highly unstable, 3, conditions (from Khalsa and Businger, 1977).

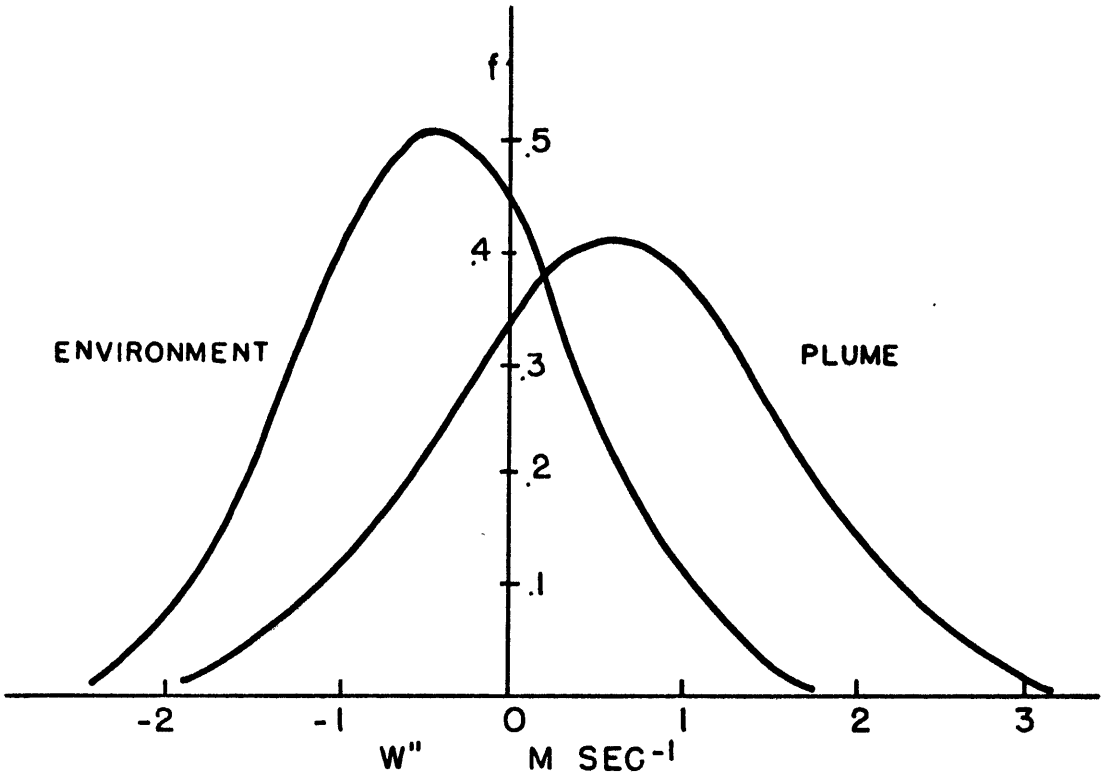

Figure 4. Normalized frequency distribution of vertical velocity (from Manton, 1977).

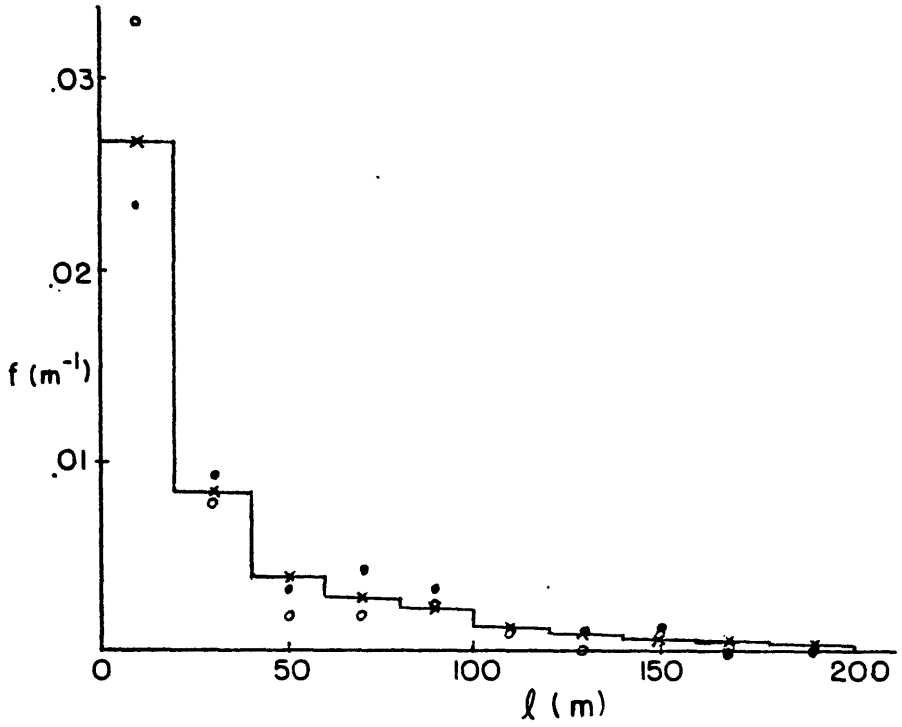

Figure 5. Frequency distribution function for the "burst length" in the temperature signal (from Manton, 1977). (x - average stability; highly unstable; weakly unstable)

impinging upon an elevated inversion using radar. The trace which appears as a continuous row of inverted "U's" is remarkably similar to Figure 6.

As these plumes (depleted of buoyancy but not momentum) are decelerated by the stable lapse rate aloft, they exchange mass and act to further deepen the mixed layer. Various investigators (Lenschow, 1970; Frisch and Businger, 1973; Davison, 1975) have found that the horizontal cross sections of plumes are elongated in an elliptical fashion in the direction of the mean wind shear. Even though the shapes of individual plumes can change with height, the total area covered by plume updrafts appears invariant with height. This need not necessarily mean that the average individual plume radius does not increase but that because of intermittency, coalescence, and vertical acceleration, the number of parcels encountered decreases with increasing height.

In the laboratory, Pshnay-Severin (1970) reports that the plume remains attached to the surface about 20 percent of the time with the rest of the time required for the surface layer to become critically unstable. A similar auto-oscillation mechanism is likely to occur in the atmosphere because the plume is a highly effective heat transporter (Kaimal and Businger, 1970). If the turbulent mechanisms become active only sporatically and likewise if these features do not move with the local mean wind then Taylor's hypothesis and the traditional way of measuring fluxes becomes less meaningful.

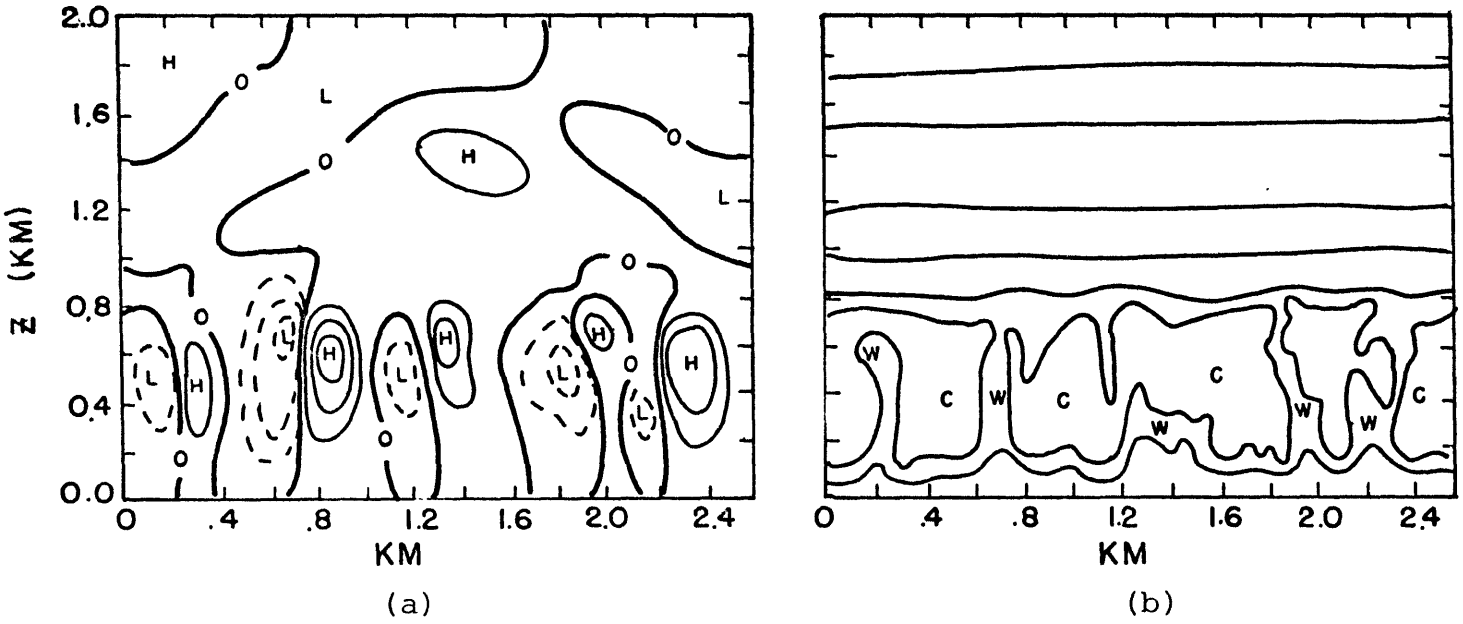

Figure 6. Fields of a) streamfunction, and b) temperature for 900 LST (from Kuo and Sun, 1976).

In other words, the average state is not realizable when the turbulent eddies are either in an active or a passive mode. It appears, therefore, that a phenomenological model which can account for intermittency of the real fluxes will be more successful than many traditional approaches.

CHAPTER II

STRUCTURE OF THE PROPOSED MODEL

A. The Properties of the Convection

The model recognizes three distinct regions, classified by the source of their burbulent kinetic energy. Zilitinkevich (1973) terms the region ($z \sim 0.1$ L; $L \equiv \frac{u_*^2 \theta_0}{\theta_* g k}$) the shear convection zone where the longitudinal and transverse velocity perturbations are generated by velocity shear; while the vertical velocities are governed by buoyancy forces. The model considers this to be the stage of plume formation. This is where Monji (1973) reports that the scale of w rapidly increases with height. The saw-tooth temperature trace is apparent in the region $0.1L < z < 0.5L$ accompanied by an increase in the heat flux. Therefore, $0 < z < 0.1L$ is the height interval region where small turbulent "bubbles" of hot air are gathered by mechanical eddies and accelerated by buoyancy up into the plume formation zone, which in turn extends over the height interval ($0.1L < z < 0.5L$). This discussion will not be concerned with the precise nature of these shear generated eddies which are discussed extensively by Townsend (1976) and Willmarth (1975).

The height where buoyancy generation begins to dominate at $z=L/2$ will be considered to be the base of the plume-type convective eddies. At this level the saw-tooth temperature and velocity time dependence is evident in Figure 2.

Higher up, the differences in plume propagation and in the mean wind shear cause the plumes to become erect while the temperature and vertical velocity fluctuations become symetric in shape. The rapid oscillations within the plume continues as the updraft is comprised of continuously interacting, turbulent elements of considerably smaller scale. The air which is not forced directly by buoyancy forces (except, perhaps near the inversion) is quiesent and is characterized by gentle, steady subsidence. (Within the plume formation zone the "sweep" event is likely to be instrumental in initiating the burst cycle. However, within the plume region the environmental subsidence is quite passive.) The entrainment along the plume-environment interface (interaction events) results in an exchange of heat, mass and momentum causing, for example, the mean plume to become cooler and less buoyant. According to observations taken throughout the mixed layer, the average percent cross-sectional area covered by plume updrafts remains nearly constant with height with an average of between 0.40 and 0.45. To maintain mass the downdraft is only slightly weaker than the mean plume updraft. There are, however, regions within the plume where the local updraft may exceed the average plume velocity at that height due to enhanced turbulence activity within the updraft region.

The plume impinges upon a very stable elevated inversion which has formed due to previous hours of surface heating in an initially stable atmosphere. The decelerating plumes mix

with the overlying air in a complex fashion. Figure 7 shows schematically a process where Kelvin-Helmholtz billows form in response to a local increase in vertical wind shear. Through entrainment the mixed layer is deepened and the inversion rises until the surface heating diminishes.

B. Determination of Model Parameters from the Initially Given State

The parameters that serve as externally determined input for the model are displayed in Table 2. In order to find the corresponding values for the surface stress the geostrophic drag laws for diabatic boundary layers is taken from Tennekes (1973).

Define: Surface Rossby no: $R_o \equiv \frac{G}{f z_o}$; Ekman length $\lambda \equiv \frac{k u_*}{f}$

$\mu \equiv + \frac{\lambda}{L}$; L = Monin-Obukov length

$u_* \equiv$ friction velocity ; $k \equiv$ von Karman constant

The geostrophic departure angle is given by:

$$\sin \varphi = \frac{A(\mu)}{k} \frac{u_*}{G}$$

The friction velocity can be obtained from the geostrophic wind, G through:

$$\ln R_o = B(\mu) + \ln \frac{G}{u_*} + \left[\frac{k^2 G^2}{u_*^2} - A^2(\mu) \right]^{1/2}.$$

Likewise the surface temperature scale, θ_* is obtained from:

$$\frac{\Delta\theta}{\theta_*} = (0.7) \left[\ln \left(R_o \frac{u_*}{G} \right) - C(\mu) \right]$$

where $\Delta\theta \equiv |\theta_{z_i} - \theta_{z_o}|$.

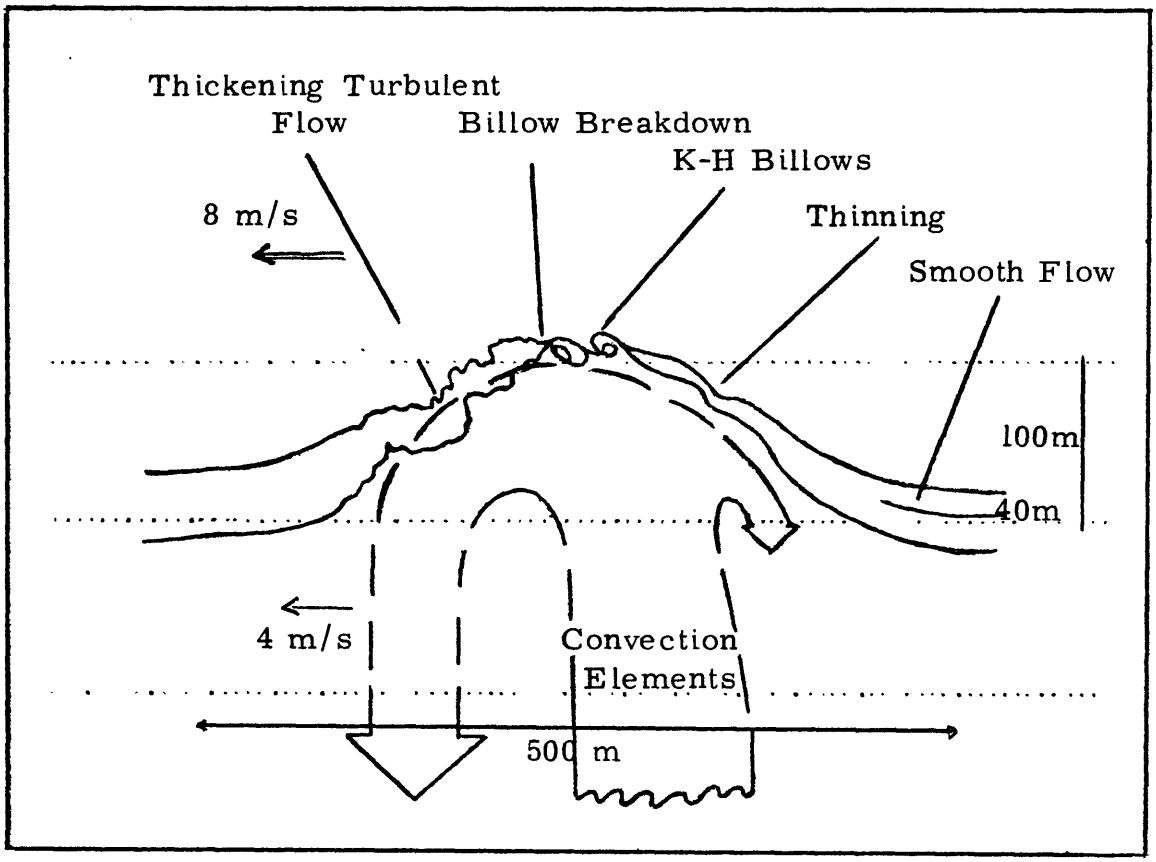

Figure 7. Schematic of the entrainment process at the plume-inversion interface (from Randall, 1976).

TABLE 2

External Input Parameters

Parameter	Symbol	Representative value (units)
Roughness length	z_o	0.05 (m)
Inversion height	z_i	10^3 (m)
Mean surface pressure	P_o	10^3 (mb)
Mean surface potential temperature	θ_o	300 (^oK)
Mean Boundary Layer		
Geostrophic Wind	V_g, U_g, G	5 (m/s)
Thermal wind across the boundary layer	ΔV_g, ΔU_g	1 (m/s)
Lower surface layer lapse rate	γ_2	0.2 (^oK/m)

This theory, based upon asymptotic invariance, cannot be used in this case for several reasons. $\Delta\theta$ cannot be chosen beforehand, as the potential temperature profile is one of the model results. More importantly, there appears to be a significant amount of scatter in the values of A,B, and C presented by Tennekes. For all unstable lapse rates, $A \simeq 5$, $B \simeq 7$ are representative but tests show that the variation with $\mu (\equiv \frac{k u_*}{f L})$ may be sufficient to make a proper solution of u_* and θ_* less than straightforward.

Alternatively, following Garrat (1978), one can use surface layer similarity theory to find suitable values for the drag and heat transfer coefficients at $z=L/2$.
For momentum transfer, this gives:

$$(C_{D,\,L/2})^{1/2} = \frac{-qh + q^{1/2}}{qh^2 - 1} \qquad (1a)$$

where: $h \equiv \Psi_M / k$, $q \equiv \frac{k^2}{\left(\ln\left(\frac{1}{2}\frac{L}{z_0}\right)\right)^2}$

and $\Psi_M = 2\ln\left(\frac{1+x}{2}\right) + \ln\left(\frac{1+x^2}{2}\right) - 2\tan^{-1}x + \pi/2$

where:

$$x = \varphi_M^{-1}$$

and

$$\varphi_m = (1 + 15 z/L)^{-1/4}$$

note: L is defined here as positive above a heated surface.

For heat transfer:

$$C_{H,L/2} = \frac{p}{1-jp} \qquad (1b)$$

where $$p = \frac{k^2}{\ln\left(\frac{1}{2}\frac{L}{z_0}\right)\ln\left(\frac{1}{2}\frac{L}{z_T}\right)} \cdot \left(1 + \frac{1}{k}(C_{D,L/2})^{1/2}\psi_M\right)$$

and $$j = \frac{1}{k} C_D^{-1/2} \psi_H$$

where $$\psi_H = 2\ln\left(\frac{1+y}{2}\right)$$

and $$y^{-1} = \varphi_H = (1+16\, z/L)^{1/2}.$$

To solve for C_D, L/2 and C_H, L/2, L/z_o, L/z_T must be estimated to a fair degree of accuracy. For surfaces such as orchards with large roughness elements, Garrat estimates $z_o/z_T = 10$ whereas over smooth surfaces, $z_o/z_T = 4$. Rough surfaces can reasonably be identified with $L/z_o = 10^2$ and smooth surfaces with $L/z_o = 10^3$. Using these limits the bounds in Table 3 are obtained. Generally, neither the Monin-Obukov nor the roughness length is known a priori. However, if the results from this calculation do not correspond reasonably with the drag coefficients employed, the process is iterated with a new initial value of L/z_o (and L/z_T).

After initial values of C_D, C_H are chosen, the surface stress and heat flux are found from:

$$u_*^2 = U_{L/2}^2 \; C_{D,L/2} \qquad (2a)$$

and

$$u_* \theta_* = U_{L/2} \; C_{H,L/2} \; (\theta_{z_0} - \theta_{L/2}) \qquad (2b)$$

TABLE 3

Surface Layer Drag Coefficients

		$C_{D',\ L/2}$	$C_{H',\ L/2}$
"Rough"	$L/z_o = 100$	15.5×10^{-3}	8.1×10^{-3}
"Smooth"	$L/z_o = 1000$	6.0×10^{-3}	4.5×10^{-3}

The next step is to find the mean wind speed at a height of L/2. Following Wyngaard, et. al. (1974), by defining the pressure gradient in terms of the geostrophic wind, the steady state mean field momentum equations may be written:

$$U - U_g = -\frac{1}{f}\frac{\partial}{\partial z}(\overline{vw})\Big|_{L/2} \qquad (3a)$$

$$V - V_g = \frac{1}{f}\frac{\partial}{\partial z}(\overline{uw})\Big|_{L/2} \qquad (3b)$$

(lower case denotes perturbation quantities)

When the inversion is approximated by an impervious lid bounding the mixed layer, the profiles of the fluxes acquire a universal form as a function of z/z_i. Figure 8 indicates that the stress profiles from a moment-closure model are curiously a function of wind direction. Especially odd is that in the convective limit, $z_i/L = 500$, $\overline{vw} < 0$ for a westerly surface wind and slightly positive for the other three wind directions. Observations are not of sufficient quality within the mixed layer to verify the model calculations. If the fluxes are assumed to be justifyably accurate, then it would be well to have the output profiles for discrete values of z_i/L from 40 to the convective limit. The direction of the surface wind can be approximated as 20^o to the left of the geostrophic direction; the same value of L as above can be used to find the proper z_i/L. An interpolated flux profile can be used on the right hand side of equations (3a,b). Combining (3a) and (3b) with the component of U

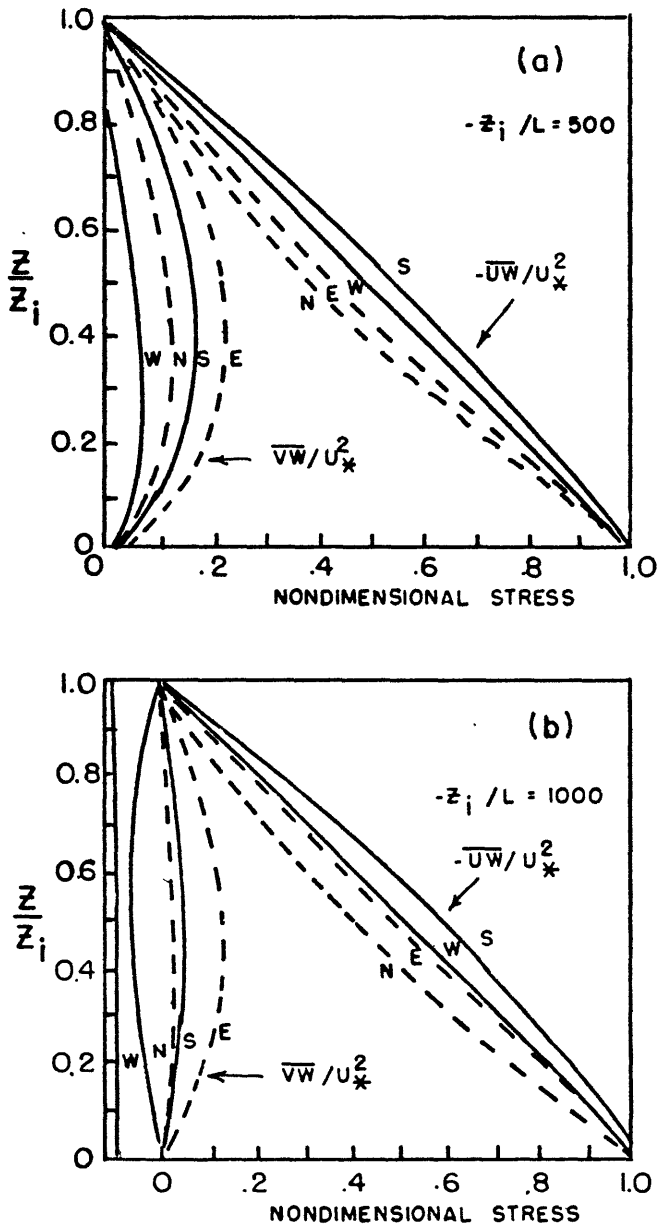

Figure 8. Stress profiles for a) $z_i/L = 50$, and b) $z_i/L = 500$ and for the four orthogonal surface wind directions (from Wyngaard, et. al., 1974).

along the wind in the surface layer yields:

$$U_{L/2} - U_{g\,L/2} = \frac{1}{\alpha} V_{g\,L/2} \qquad (4)$$

where $\alpha \equiv -\frac{\partial}{\partial z}(\overline{uw}) \Big/ \frac{\partial}{\partial z}(\overline{vw})$.

Combining (4) and (2a) and introducing G, the magnitude of the geostrophic wind, produces an equation for V_g: (dropping subscripts)

$$\left(\frac{-f z_i \mu}{C_D G}\right) - \left((1-\mu^2)^{1/2} + \frac{1}{\alpha}\mu\right)^2 = 0 \qquad (5)$$

where $\mu \equiv V_g / G$.

In the northern hemisphere the surface wind is sub-geostrophic when $\alpha > 0$, $\mu < 0$ while in the southern hemisphere $\alpha < 0$, $\mu > 0$. Equation (5) is readily solved using an iterative procedure such that the angle of geostrophic departure is given by (6).

$$\varphi = \sin^{-1}\mu \qquad (6)$$

The above relations allow direct solution of the entire set of flow and flux parameters.

$$\begin{aligned} U_g &= G\cos\varphi \\ V_g &= G\mu \\ U &= U_g + \frac{1}{\alpha} V_g \\ u_* &= C_{D,L/2}^{1/2}\, U \\ L^2 &= \frac{z\,\Theta_0\,u_*^3}{\gamma_2 k g U C_{H,L/2}} \quad \text{where } \gamma_2 \equiv \int_{z_0}^{L/2} \frac{\partial\Theta}{\partial z}\,dz \\ \Theta_* &= \frac{u_*^2\,\Theta_0}{k g L} \end{aligned} \qquad (7)$$

The values of L/z_o and z_i/L are subsequently checked to be in reasonable agreement with the value assumed at the onset.

C. Mechanical Stresses and the Mean Wind Profiles in the Surface and Mixed Layers

In its present state, the plume convection model is not capable of predicting the stress profile throughout the entire mixed layer. Once the surface stress vector has been determined with some certainty, the departure from the mean geostrophic wind can be calculated from the velocity flux profiles obtained from the moment-closure model. For this purpose, the velocity and fluxes are partitioned into mean geostrophic departure and thermal wind components. This is done as follows: Define the geostrophic departure as

$$U - \overline{U}_g^z = -\frac{1}{f}\frac{\partial}{\partial z}(\overline{vw})_{gd}$$
$$V - \overline{V}_g^z = \frac{1}{f}\frac{\partial}{\partial z}(\overline{uw})_{gd} \qquad (8)$$

and let the thermal wind components be:

$$\Delta U_g\,(z/z_i - 0.5) = \frac{1}{f}\frac{\partial}{\partial z}(\overline{vw})_T$$
$$\Delta V_g\,(z/z_i - 0.5) = -\frac{1}{f}\frac{\partial}{\partial z}(\overline{uw})_T$$

where $V_g = V_g + \Delta V_g\,(z/z_i - 0.5)$

$U_g = U_g + \Delta U_g\,(z/z_i - 0.5$

$\overline{uw} = (\overline{uw})_{gd} + (\overline{uw})_T$

$\overline{vw} = (\overline{vw})_{gd} + (\overline{vw})_T$.

Wyngaard, et. al. (1974) shows that for the differentiated form of equation (8) the thermal wind terms often are dominant. The assumption implies that the shear of the geostrophic wind greatly alters the mechanical stress but has no measurable effect upon the observed wind shear. Parcels of air within the convective boundary layer rise from the surface to the inversion in about 10 minutes and the result is that the horizontal wind does not respond geostrophically to the mean horizontal pressure gradient at each height. However, the average pressure gradient that is generated over many plume cycles is balanced by the mean geostrophic winds within the boundary layer. The test of this reasoning lies with the application of the model to various baroclinic situations.

Figure 9a displays approximate flux profiles at z_i/L for an easterly surface flow and for the average of all wind directions. The "average" wind profile (Figure 9b) shows a substantial decrease in the wind shear with height in the mixed layer. Although the U component exceeds its geostrophic counterpart, its magnitude is sub-geostrophic because the longitudinal stress profile allows virtually no turning with height. The moment closure and the slab-type mixed layer models agree in that $V \sim 0$ throughout an unstable boundary layer. The wind profile for surface easterlies displays significantly more shear in the lower mixed layer. It will be interesting to observe the extent, if any, to which this behavior is verified. Within the surface layer

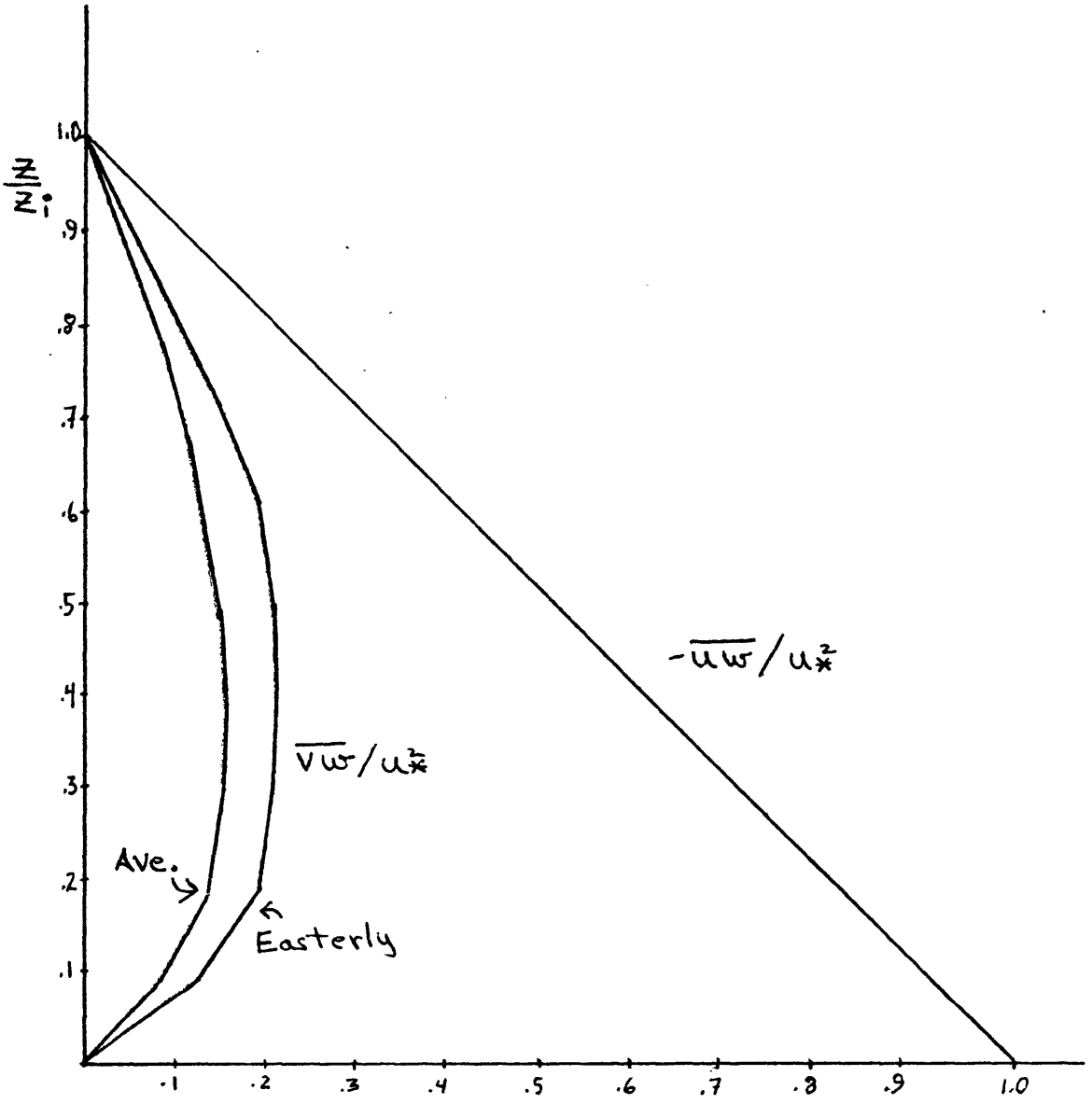

Figure 9.
a) Assumed flux profiles derived from Wyngaard's moment-closure model for $z_i/L = 50$.

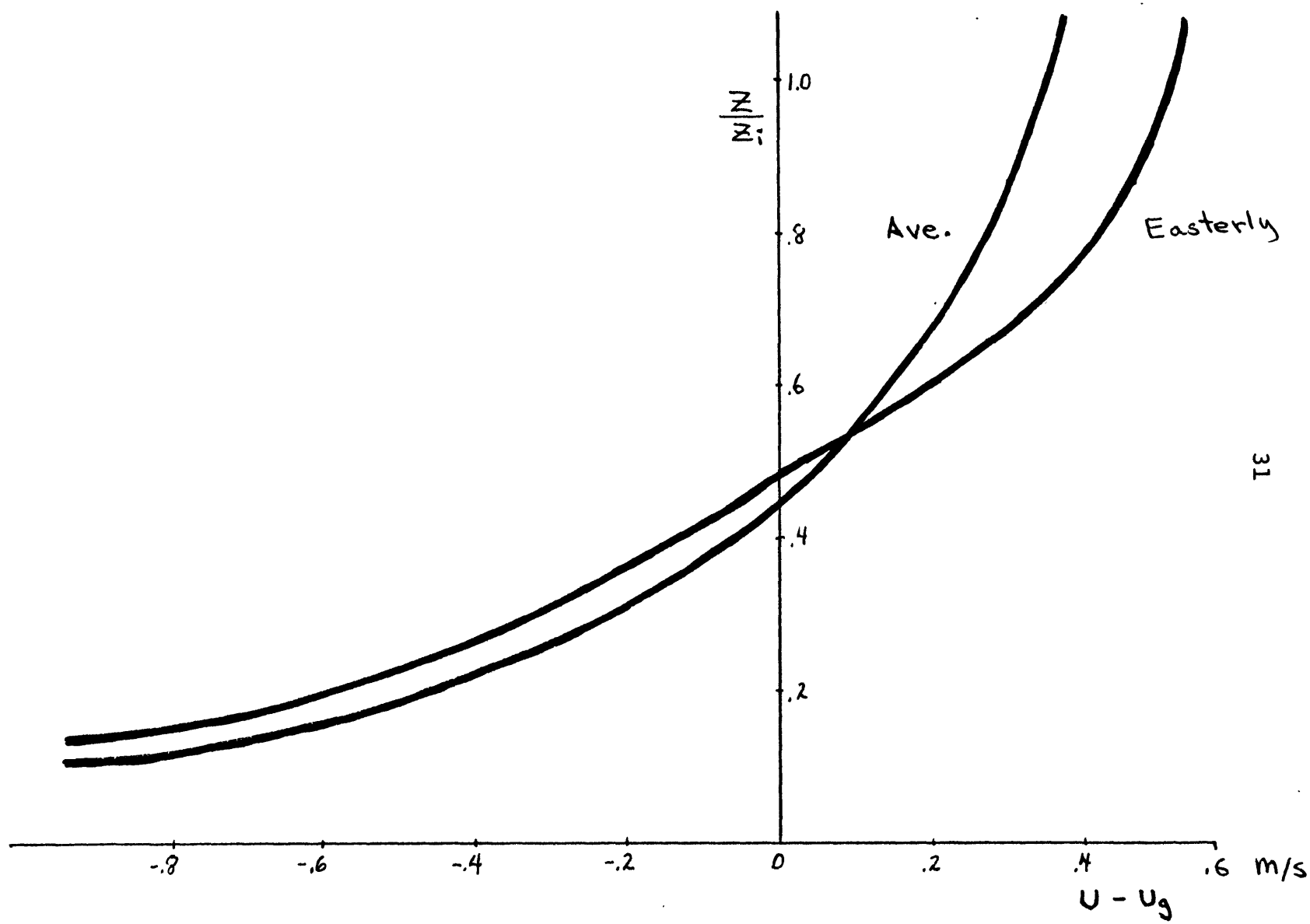

Figure 9.
b) Geostrophic departure associated with stress profiles in Figure 9a).

the mean wind profile follows similarity theory up to the height where it matches the profile of the mixed layer.

D. Structure of the Convection Model

1. Mixed layer convection

The convective elements within the surface and mixed layers are modeled after Manton (1975, 1976). The pertinent steps of the derivations will be outlined but a more complete discussion can be found in the original references. The equations for conservation of momentum and mass for a thermal plume may be written as:

$$\frac{D}{Dt}(\rho_p V w_p) = g(\rho_e - \rho_p) + \rho_e w_e \frac{DV}{Dt} \qquad (9a)$$

$$\frac{D}{Dt}(\rho_p V) = \rho_e \frac{DV}{Dt} \qquad (9b)$$

where $()_p \equiv$ plume variable, $()_e \equiv$ environmental variable

V= elemental plume volume, $\rho \equiv$ potential density.

The plume volume element is defined as the mean volume flux divided by the rate of plume generation per unit area: i.e.

$$V = A_p w_p / (N/\tau) \qquad (10)$$

where $A_p \equiv$ fraction of horizontal plane occupied by thermals

$N \equiv$ plumes per unit area at the base of convection

$\tau^{-1} \equiv$ rate of plume release.

Since the "free" convection within the mixed layer originates in the upper portion of the surface layer, the lower

boundary of the deep convection model is arbitrarily placed at z=4L. The vertical coordinate is $\zeta = z-4L$.

The lower boundary conditions are:

$$w_{pf} = w(z=4L)$$

$$\rho_{pf} = \overline{\rho_f}(1-S_f)$$

or

$$\theta_{pf} = \overline{\theta}_f(1+S_f)$$

According to observations $A_p \simeq 0.45$ throughout the mixed layer and as such will be taken as a constant. Employing this assumption in equations (9a,b) yield a characteristic length scale given by:

$$D_2 = (2-A_p) w_{pf}^2 / S_f g$$

The local response time of a thermal, D/w_{pf}, is much smaller than z_i/w_{pf}, the response time of the entire layer. The total time derivative, $\frac{D}{Dt}()$ in equation (9) is therefore dominated by vertical advection within the plume

Replacing ∇, equation (9) becomes:

$$[(\rho_p+\rho_e) w_p - \rho_e w_e] \frac{\partial w_p}{\partial z} = (\rho_e-\rho_p) g \qquad (11a)$$

$$w_p \frac{\partial}{\partial z} \rho_p = (\rho_e-\rho_p) \frac{\partial w_p}{\partial z} \qquad (11b)$$

Because the thermal elements are not isolated, A_p is constant and does not increase with altitude as does the turbulent plume of Morton, et. al. (1956). The right hand side of equation (11b) shows that the rate of entrainment is proportional to the vertical acceleration, rather than proportional to the updraft velocity; the latter is a common assumption for

turbulent jets.

The equations are written in terms of the normalized variables defined by:

$$w = \omega\, w_{pf}, \quad \rho_p = \bar{\rho}(1 - s_f s), \quad y = \frac{z - 4L}{D_2}.$$

chosen such that at $y=0$, $\omega=1$, $s=1$. Neglecting terms of order s_f, the mass flux balance requires that $w_e/w_f = -\omega \cdot \frac{A_p}{1-A_p}$. Equations (11a,b) transform to:

$$\omega \frac{\partial \omega}{\partial y} = s$$

$$\frac{\partial s}{\partial y} = -(1-A_p)^{-1}\left(\frac{s}{\omega}\right)\frac{\partial \omega}{\partial y} + \frac{1}{s_f \bar{\rho}}\frac{\partial \bar{\rho}}{\partial y} \qquad (12)$$

or

$$\frac{\partial s}{\partial y} = -(1-A_p)^{-1}\left(\frac{s}{\omega}\right)\frac{\partial \omega}{\partial y} + \frac{1}{s_f \bar{\Theta}}\frac{\partial \bar{\Theta}}{\partial y}$$

A mixed layer, by definition, is essentially isentropic even though the mixing is done by thermally generated turbulence. Setting $\partial\bar{\Theta}/\partial z \equiv 0$ makes possible the simple similarity solutions:

$$\omega = \left[1 + \frac{3-2A_p}{1-A_p}\, y\right]^{\frac{(1-A_p)}{(3-2A_p)}} \qquad (13)$$

$$s = \omega^{-\frac{1}{1-A_p}}$$

$$\bar{\Theta} = \bar{\Theta}_o(t)$$

For A_p=0.4 and 0.5, the normalized solutions are displayed in Figure 10. For $y >> 1$ the updraft increases as $z^{1/4}$ until the inversion is approached. However, Farmer (1975) reports that the velocities of thermals approach their asymptotic

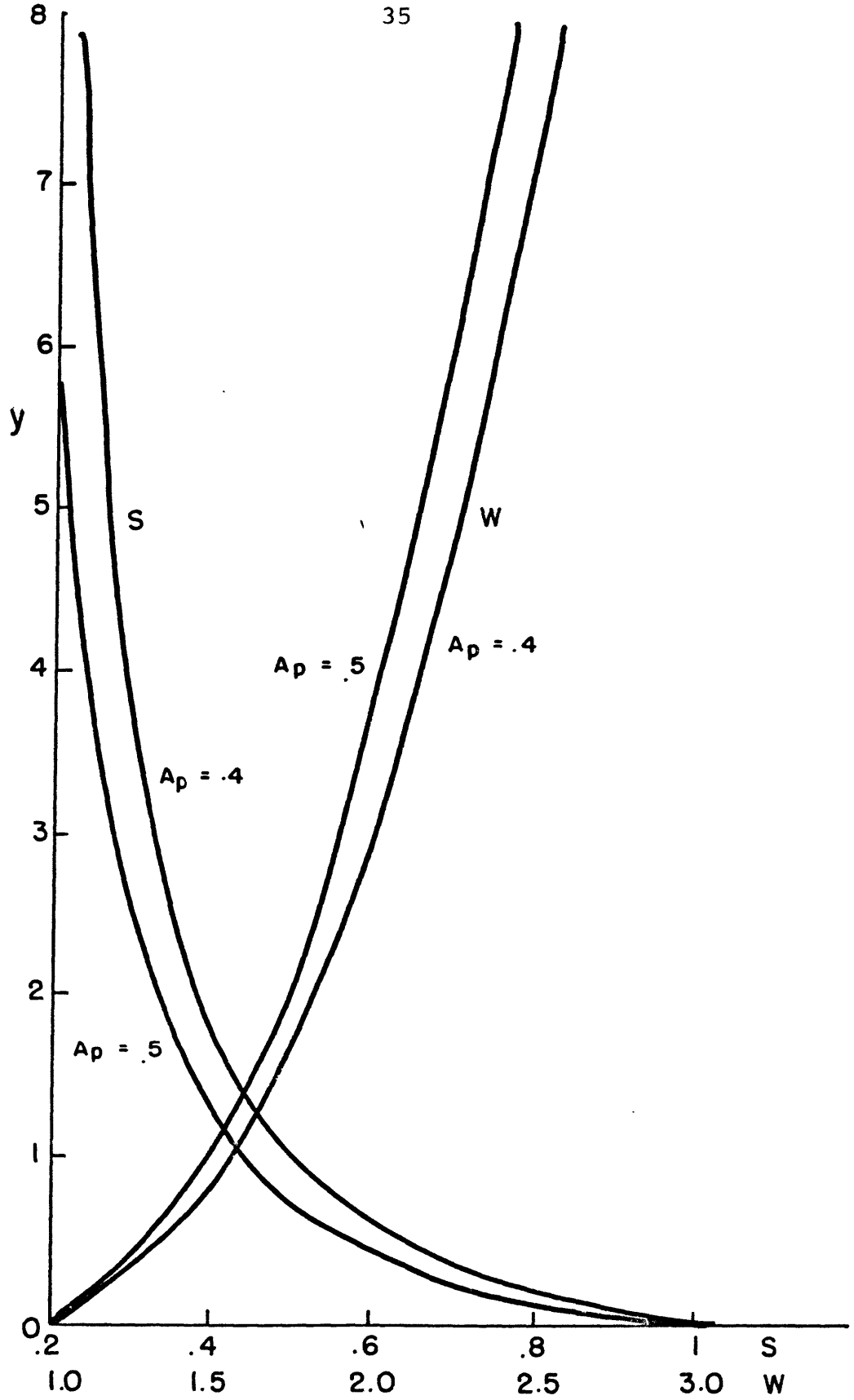

Figure 10. Profiles of the normalized vertical velocity, w, and buoyancy factor, S, as functions of $y=(z-z_b)/D_2$ for the neutrally stratified deep convection model.

limit at a level well within the mixed layer. This is most likely due to the decelerating effect of slightly stable lapse rates, observed to be about 0.2^{o}K. per kilometer (Warner and Telford, 1967). This stability is the result of the entrainment of warm air into the top of the mixed layer at the inversion. In order to close the system it is proposed that stable potential temperature gradients do not depend upon the local dynamics but only upon the magnitude of local temperature fluctuations; i.e.

$$\frac{\partial \bar{\theta}}{\partial y} = S_f S \bar{\theta} \sigma \quad \text{where} \quad \sigma = \text{const} = o(1) .$$

This states that the buoyancy of a thermal increases with increasing local stability. This is impossible in the surface layer where the lapse rate is superadiabatic. However, above a height of 4L, the stability, which is nearly neutral, changes little with height. This closure assumption allows the well behaved similarity solutions as shown by Manton (1975).

$$\omega = \left[1 + \left(\frac{3-2A_p}{\sigma(1-A_p)}\right)(1-e^{-\sigma y})\right]^{\frac{(1-A_p)}{(3-2A_p)}} \qquad (14a)$$

$$S = e^{-\sigma y}\,\omega^{-\frac{1}{(1-A_p)}}$$

$$\bar{\theta} = \bar{\theta}_f(t) \exp\left[\tfrac{1}{2} S_f \sigma (\omega^2 - 1)\right]$$

These have the asymptotic form for $y\cdot\sigma >> 1$:

$$\omega_\infty = \left[1 + \frac{3-2A_p}{\sigma(1-A_p)}\right]^{\left(\frac{1-A_p}{3-2A_p}\right)} \qquad (14b)$$

$$S = e^{-\sigma y}\,\omega_\infty^{-\frac{1}{(1-A_p)}}$$

$$\bar{\theta} = \bar{\theta}_0(t) \exp\left[\tfrac{1}{2} S_f \sigma (\omega^2 - 1)\right]$$

The asymptotic value of the plume updraft is inversely proportional to the buoyancy parameter, σ . Table 4 indicates that as w_{∞} increases this value is less likely to be approached within the mixed layer.

At the height of 4L the thermals have undergone a substantial acceleration and entrainment is likely to deplete their buoyancy rapidly with increasing height. The proper value of σ , therefore, depends upon the height (measured in L) that the free convection is assumed to commence. (For the present case, σ =0.1 appears to be reasonable.) The buoyancy factor, σ , as a function of the free convection height can be adjusted to better match observations of plumes within the mixed layer. The normalized solutions for σ =0.5 and 0.3, A_p=0.5 shown in Figure 11 indicates that the reduced entrainment and stability counteract one another to produce a nearly constant vertical velocity in the upper mixed layer. When the buoyancy factor, σ , is increased, the lower mixed layer becomes more stable. The importance of this effect in the convective boundary layer will be discussed in regard to the combined surface-mixed layer model.

E. The Structure of Convection Within the Surface Layer

The model of convection near the surface uses the same equations (9a,b) written in terms of the individual plume cross-sectional area, a_p .

TABLE 4

Model sensitivity to the buoyancy parameter,

for $A_p = 0.5$, $D_2 = 100$ m

σ	ω_∞	$y @ e^{-\sigma y} = 0.1$	Z (m)
4	1.19	.58	58
3	1.24	.77	77
2	1.30	1.15	115
1	1.49	2.3	230
.5	1.73	4.6	460
.3	1.95	7.6	760
.1	2.53	23.	2300

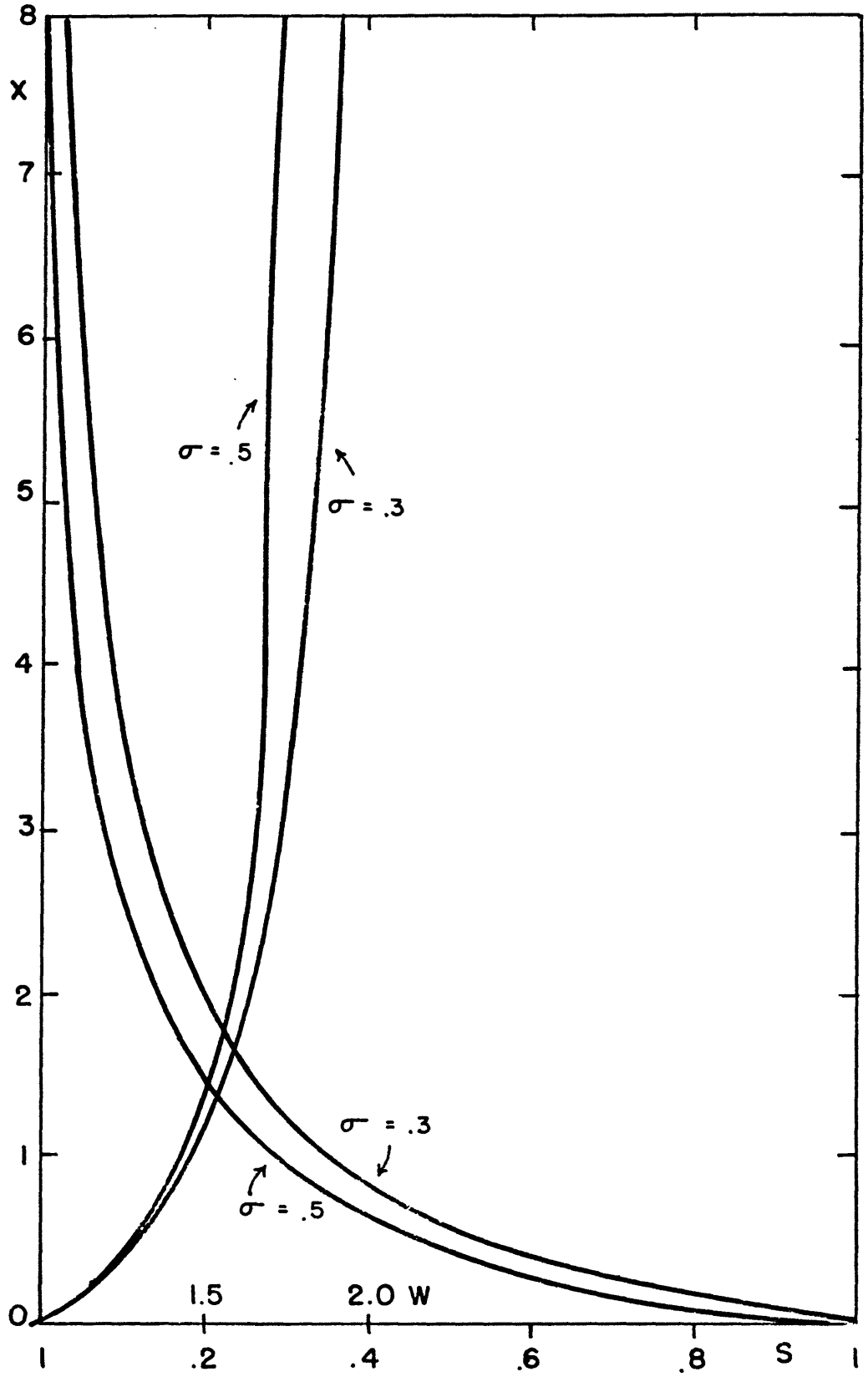

Figure 11.
a) Normalized solutions w,s, for the stable stratified deep convection model for σ = .5 and σ = .3.

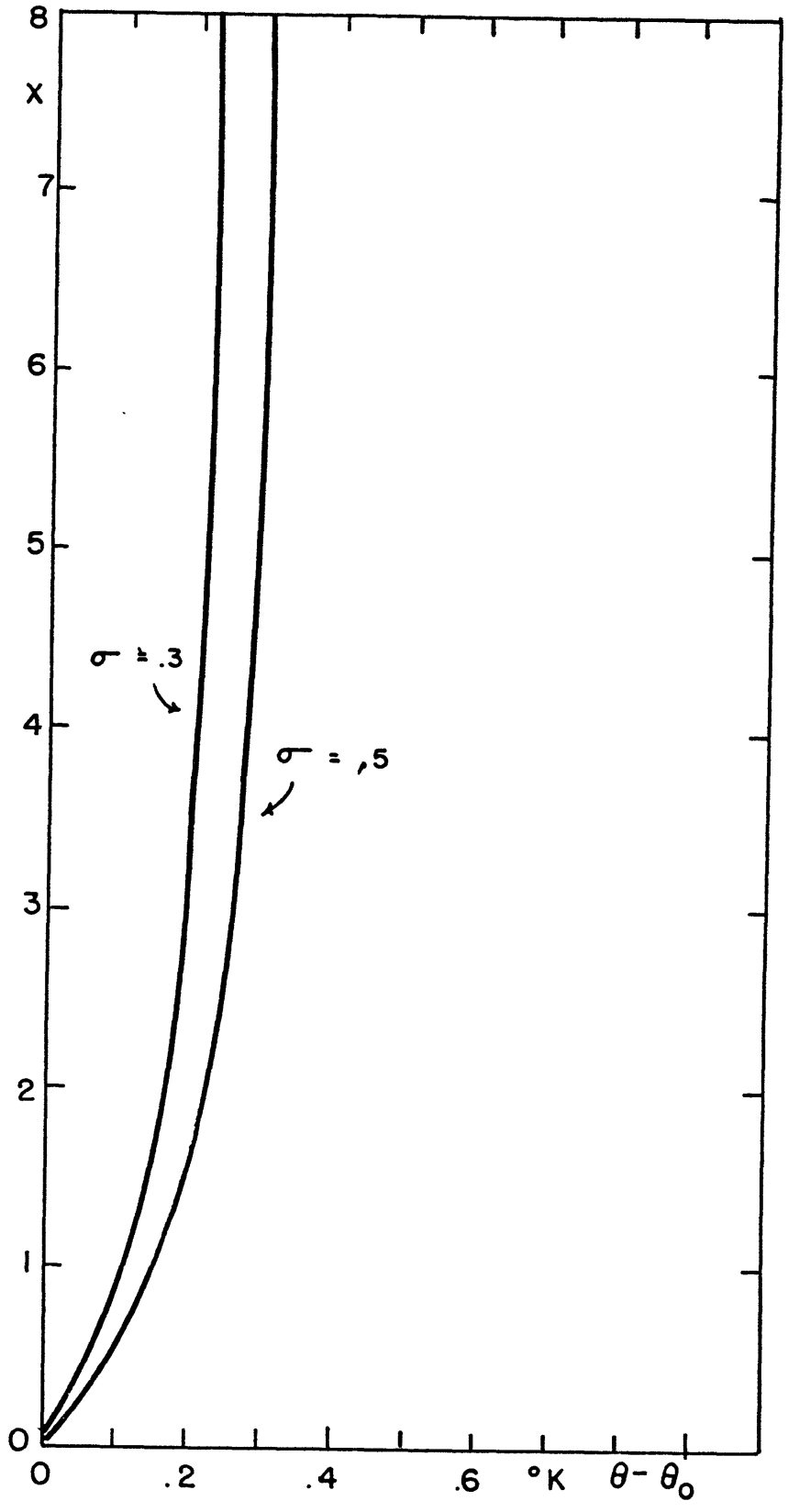

Figure 11.
b) Normalized solutions for $\theta - \theta_o$ for the stable stratified deep convection model for $\sigma = 0.5$ and $\sigma = .3$.

According to Manton (1976):

$$\frac{D}{Dt}(\rho_p a_p) = \rho_e \frac{D}{Dt} a_p$$

$$\frac{D}{Dt}(\rho_p a_p w_p) = (\rho_e - \rho_p) g a_p + \rho_e w_e \frac{D}{Dt} a_p \quad (15)$$

The area fraction of plumes is given by a constant A_p where

$$A_p = a_p n \quad (n \equiv \text{plume population density})$$

Once again, $-s$ is the density perturbation which is $O(10^{-3})$, so that vertical advection dominates the time derivative permitting equation (15) to be approximated by:

$$-\frac{1}{\bar{\theta}} \frac{\partial \bar{\theta}}{\partial z} = \frac{1}{\bar{\rho}} \frac{\partial \bar{\rho}}{\partial z} = \frac{\partial s}{\partial z} + \frac{s}{a_p(1-A_p)} \frac{\partial a_p}{\partial z} \quad (16)$$

$$\frac{1}{2} \frac{\partial \overline{w_p^2}}{\partial z} = \frac{s g}{(1-A_p)} - \frac{w^2}{a_p (1-A_p)} \frac{\partial a_p}{\partial z}$$

Within the constant stress layer, the surface heat flux is considered known, so that a characteristic vertical velocity and length are given by:

$$w_* = \frac{u_* \theta_*}{\bar{\theta}_0} \quad \text{and} \quad D_1 = w_*^2 / g$$

The non-dimensional governing equations with $x=z/D$, $\omega=w/w_*$ and $\alpha'=a_p/a_*$ then become:

$$-\frac{1}{\bar{\theta}} \frac{\partial \bar{\theta}}{\partial x} - \frac{\partial s}{\partial x} = \frac{s}{\alpha'} \frac{1}{(1-A_p)} \frac{\partial \alpha'}{\partial x} \quad (17)$$

$$\frac{1}{2}(1-A_p) \frac{\partial \omega^2}{\partial x} = s - \left(\frac{\omega^2}{\alpha'}\right) \frac{\partial \alpha'}{\partial x}$$

Convection within the surface layer should follow Monin-Obukov similarity. As the plumes we consider are not identifiable below a height of $z=L/2$, it is possible to apply free convective scaling to the basic plume model described in section (D). Following Manton (1976), assuming that potential temperature and vertical velocity fluctuations are independent of u_*, dimensional analysis yields:

$$\overline{\theta'^2} = c_\theta \left(\frac{\bar{\theta}_0 w_*}{u_*}\right)^2 (z/L)^{-2/3}$$
$$\overline{w'^2} = c_w u_*^2 (z/L)^{2/3} \qquad (18)$$

where we take the values $c_\theta = 0.90$ and $c_w = 3.6$ from observations. In the plume model the variances can be written explicitly in terms of plume variables, so for example,

$$\overline{w'^2} = A_p w_p^2 + (1-A_p) w_e^2$$
$$\doteq w_p^2 \left(A_p/(1-A_p) \right)$$

Applying (18) therefore restricts the similarity solutions for the thermal elements to have the dependences on $x=z/D$:

$$S = S_0 x^{-1/3}, \quad w = w_0 x^{1/3}, \quad \alpha' = x^m$$

where
$$S_0^2 = \frac{0.9(1-A_p)}{A_p k^{2/3}}$$
$$w_0^2 = 3.6 \frac{(1-A_p) k^{2/3}}{A_p} \qquad (19)$$
$$m = \frac{S_0}{w_0^2} - \frac{1}{3}(1-A_p)$$

The mean potential temperature gradient is given by:

$$-\frac{1}{\bar{\theta}}\frac{\partial \bar{\theta}}{\partial x} = \frac{1}{(1-A_p)} s_0 \left[\frac{s_0}{\omega_0^2} - \frac{2}{3}(1-A_p)\right] x^{-4/3}$$

The updraft velocity increases at a faster rate and s decreases at a slower rate than in the mixed layer aloft. The vertical variation of the plume variables s and w in Figure 12 show that the individual plume in the surface layer accelerates and spreads simultaneously. Therefore the number of plumes in any given area must decrease with height indicating that thermal elements coalesce as they rise within the surface layer.

F. Interpretation of the Model

1. Surface layer-mixed layer transition

In linking the surface layer and mixed layer plume convection models, $z=4L$ is chosen as the level above a heated surface where the mixed layer dynamics begin to take effect. Since the rising thermals do not suddenly change their structure, a transition zone in the range $5L < z < 10L$ is postulated where the solution is a combination of the two models. For $z < 4L$ only surface layer plumes exist and for $z > 11L$ deep convection plumes are the sole turbulent elements. The combination which need not be linear is formulated to allow smooth transition in all plume quantities between models.

2. Intermittency- Evaluation and effects

Convection in the atmosphere is intermittent because a

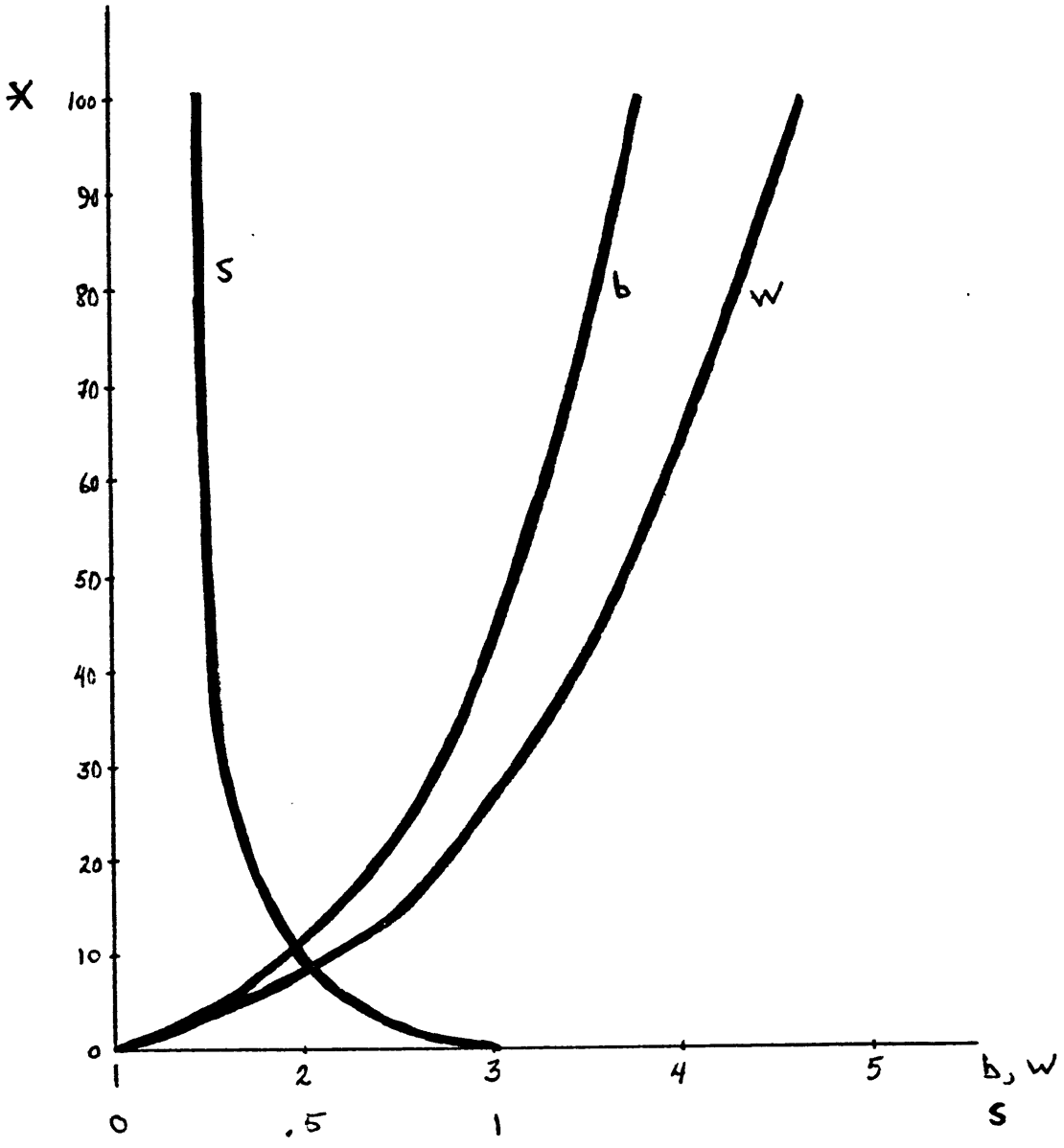

Figure 12. Normalized solutions to the surface layer plume model (w = vertical velocity; b = plume width; s = buoyancy factor).

plume circulation transports heat vertically at a faster rate than the average available from surface heating. The intermittency factor is defined at z=L/2 by:

$$I \equiv \frac{\tau_{active}}{\tau_{act.} + \tau_*} = \frac{\tau_{act.}}{\Upsilon}$$

where $\Upsilon \equiv$ total plume cycle time

$\tau_* \equiv$ time required for a critical lapse rate to develop immediately following plume termination at L/2

$\tau_{act.} \equiv$ time required for the plume turbulence to deplete the layer below L/2 of sufficiently buoyant air to maintain the convection

Pshenay-Severin (1970) has devised an auto-oscillating convection model where the quiescent and disturbed states are represented by mixing coefficients K, $\mathcal{K}$ respectively. From this model the intermittency can be computed from:

$$\frac{\tau_*}{\tau_{act}} = 16.54 \cdot \frac{\delta^2 \gamma_*^2}{\phi_o^2} \frac{K}{\mathcal{K}} \qquad (20)$$

and the intermittency is calculated from:

$$I^{-1} = \frac{\tau_*}{\tau_{act}} + 1$$

where $\delta \equiv \gamma_{final} / \gamma_*$

$\gamma_{f.} \equiv \gamma_{final}$ lapse rate immediately following the active stage

$\gamma_* \equiv$ critical lapse rate for plume formation

$\phi_o =$ surface heat flux / effective conductivity

The mixing coefficient during the quiescent period; K is assumed to be a known constant whereas K is obtained from:

$$K\,\overline{\gamma}_p = \frac{\overline{w'\theta'}(1/2)}{Ie} \quad \frac{u_*\theta_*}{Ie}$$

where Ie is the effective intermittency and $\overline{\gamma}_p$ is the average lapse rate in the sub-plume layer during the active phase. Here it is assumed that the heat transport between plume activity is negligible above a height of $z < 0.1L$. The heat flux divergence within the layer $z < 0.5L$ during quiescent periods causes the lapse rate to increase to γ_*. At this point the convective mixing commences and continues until the mean surface layer lapse rate is reduced to γ_{final}. Equations (20) and (21) give the intermittency that is associated with the mean heat flux at $z=L/2$.

$$\frac{1}{I} - 1 = C / Ie \qquad (22)$$

where $C = \overline{w\theta}\,(16.54)\,\delta^2\gamma_*^2 / (\varphi_0^2 K_0 \overline{\gamma}_p)$

By assuming that $\delta = \frac{1}{2}$, $\gamma_* = .5\ ^{\circ}K/m$, $\overline{\gamma}_p \simeq \gamma_2$

$$f_0 = 3 \cdot u_*\theta_* \ , \quad K_0 = 10^{-2}$$

the constant C can be written:

$$C = \frac{0.15}{(C_H C_D \bar{\theta}_0 \bar{U}^3 \gamma_2^3)^{1/2}}$$

The effective intermittency, Ie, appears in (21) because the average heat flux (at L/2) during the active stage is affected by intermittency. Consider the vertical cross section through an idealized field of plumes in Figure 13. In Figure 13a, due to intermittency only two of the four plume

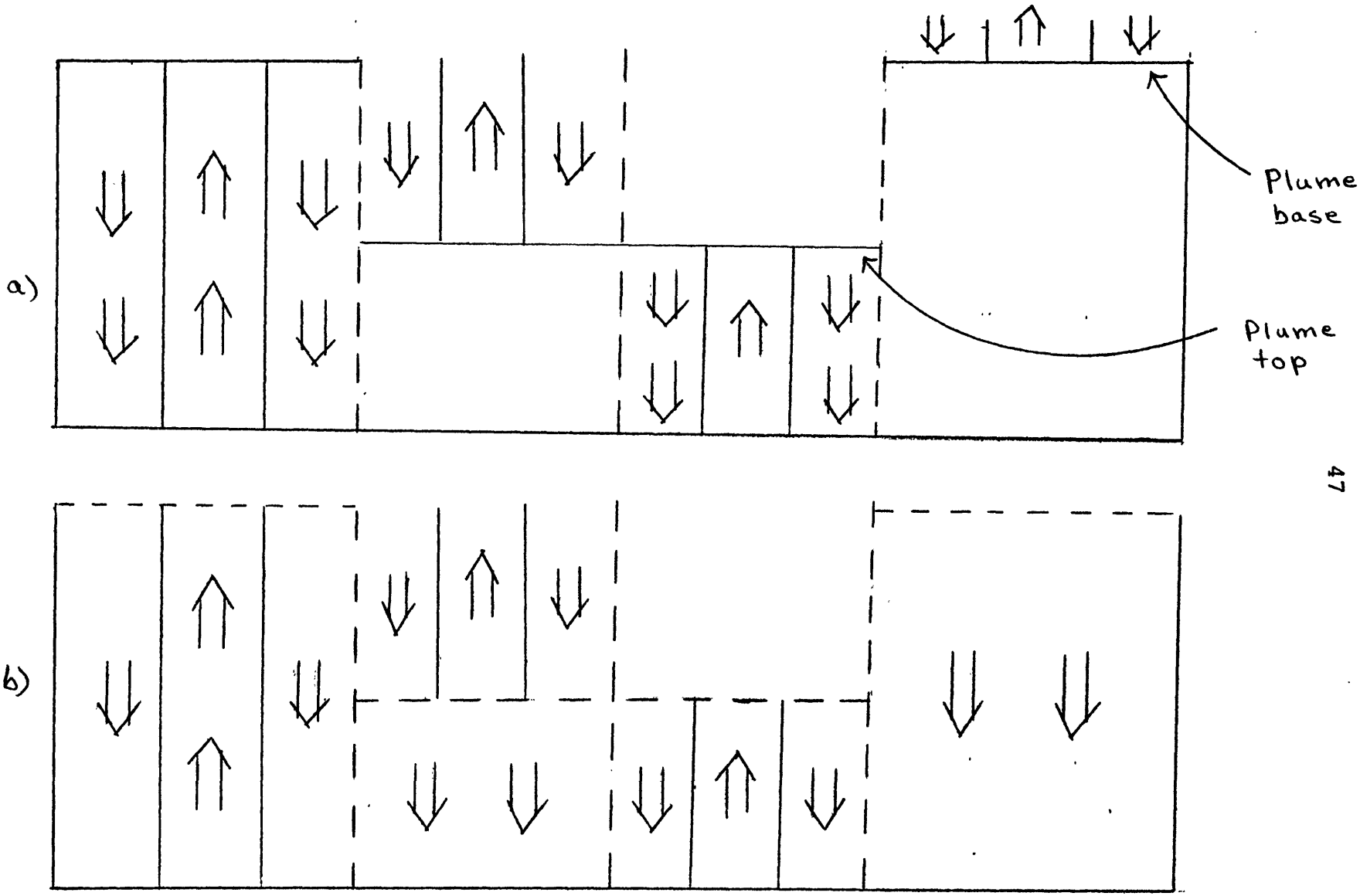

Figure 13. Schematic vertical cross-section of a plume field where a) $I = I_e = 0.5$ and for b) $I = 0.5$, $I_e = 1$.

cells are occupied by actively overturning convection. Therefore, the flux within the active plumes is $2\overline{w\theta}$. In the lower sketch, despite the intermittency the entire field is occupied by either a plume updraft or downdraft such that the time average flux per active area is $\overline{w\theta}$. Numerical simulations (Kuo and Sun, 1976) indicate that in natural convection plumes enroach upon one another's territory to a certain extent. $(1-\beta)$ measures the fraction of the area in a plume cell that is inactive; that is, when an updraft does not occupy the cell at that level. The velocity of the top and bottom of the thermal circulation are assumed to move with the updraft velocity such that the intermittency is uniform with height. Then at any height the mean real flux can be expressed as:

$$\overline{w\theta} = w_p \theta_p A_p + (I_e - A_p) u_e w_e$$

or

$$\frac{\overline{w\theta}}{I_e} = w_p \theta_p A_p' + (1 - A_p') u_e w_e \qquad (23)$$

where $A_p' \equiv A_p / I_e$

$$I_e = I(1-\beta) + \beta$$

Substituting for I_e in (21) gives the following equation for I:

$$I = \frac{\left[(1-2\beta) - C + \left[(1-2\beta-C)^2 + 4\beta(1-\beta)\right]^{1/2}\right]}{2(1-\beta)}$$

In the model, therefore, it is necessary to replace A_p with A_p^1, and this has the effect of increasing the updraft

area. Since $\beta \simeq 0.75$ appears to be in fair agreement with what little data there is, the effect of intermittency on plume variables is minor.

With the intermittency determined the cycle of plume formation can be approximated. According to Pshnay-Severin (1970) the time lag between thermals takes the form;

$$t_* = \frac{\pi \gamma_* L/2}{K \varphi_0^2} = \frac{\text{const.} \times L}{(u_* \theta_*)^2}$$

From which the plume residency time is:

$$t_{active} = I \Pi$$

and the cycle period is given by:

$$\Pi = t_* / (1-I)$$

While it is recognized that a turbulent field contains energy on an entire range of time and space scales, these represented by the model are responsible for much of the flux of heat and momentum.

Intermittent turbulence also occurs on scales smaller than the plumes. Manton (1977) estimates that plume-scale motions comprise only 60 percent of the measured heat flux in updrafts while in downdraft regions they account for 80 percent. Khalsa and Businger (1977) successfully use the fact that turbulence is modulated by plume updrafts to conditionally sample the trade wind boundary layer. A simple way to include this intermittent contribution is to write the modulated fluxes and variances as:

$$\overline{w^2} = I_e \left[w_p^2 (1+\eta) A_p' + w_e^2 (1+\xi)(1-A_p') \right]$$

$$\overline{w\theta} = I_e \left[w_p \theta_p (1+\eta') A_p' + w_e \theta_e (1+\xi')(1-A_p') \right]$$

The magnitudes of the plume velocity and buoyancy are altered as follows:

$$S_o^2 = \frac{0.9}{k^{2/3}} \frac{1}{I_e} \left[\frac{A_p'}{1-A_p'} + A_p' \left(\eta + \xi \frac{A_p'}{1-A_p'} \right) \right]^{-1}$$

$$w_o^2 = 3.6\, k^{2/3} \frac{1}{I_e} \left[\frac{A_p'}{1-A_p'} + A_p' \left(\eta + \xi \frac{A_p'}{1-A_p'} \right) \right]^{-1}$$

Only a portion of the turbulent energy is attributable to the modeled top-hat plume motions thereby decreasing the magnitude of plume variables. The model output is translated into average correlations by: (x,y represent any plume variables, e.g. θ,w)

$$\overline{xy} = I_e \left[\frac{A_p'}{1-A_p'} + A_p' \left(\eta + \xi \frac{A_p'}{1-A_p'} \right) \right] x_p y_p$$

In this way the model can be used to calculate the mean field, average fluxes, and characteristics of the thermal elements.

3. The array of plumes in the horizontal plane

The plume variables that arise from the model are ensemble averages, and their interpretation in terms of

individual thermal elements is ambiguous. The idealization employed is that the plumes encountered at a certain altitude are identical. In reality, there is a size distribution centered about the modeled scale. Asai (1970) shows that the inhibiting effect of shear causes the preferred mode of convection to be alligned with the mean wind shear vector. Near the surface, Davison (1975) observed the ratio of along wind to cross wind plume dimensions to be from five to eight under moderate wind conditions. Deep within the mixed layer where the mean wind shear is small, the free convection limit implies that the plumes become nearly symetric. The plume translation speed is uniform with height and equal to the velocity at some height within the mixed layer. An appropriate form for dimension ratio at z=L/2 is:

(r = plume length/plume width) $(U = [m/s])$

$$r = 1 + 0.3 (U_t - U_{L/10})$$

or

$$r = 1 + 0.3\ U_{tr}$$

where U_{tr} is the translation velocity relative to the buoyant bubbles originating at 0.1L.

Since unidirectional shear does not affect transverse motions, the cross wind dimension, b, of plumes is related only to the height of the plume formation, $D_p \equiv L/2$. An appropriate initial plume width is taken to be 10D=5L. A schematic of the horizontal plume field (Figure 14) shows a plausable array of updrafts, downdrafts and inactive regions.

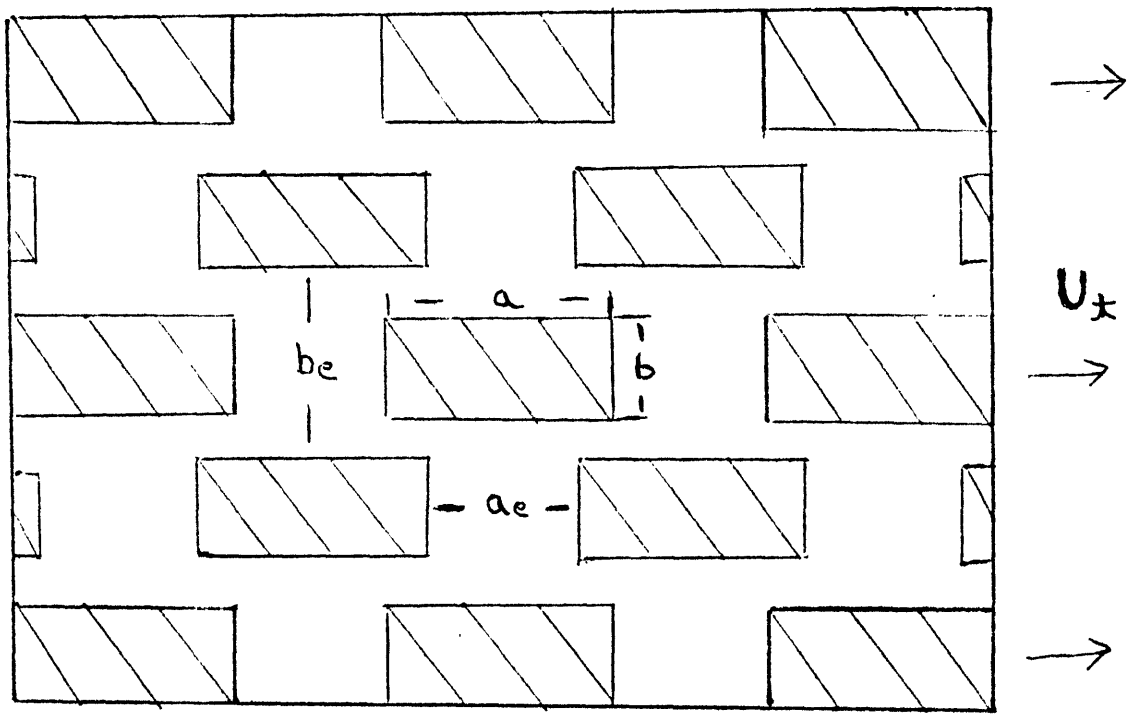

Figure 14. A schematic of a horizontal cross-section of a field of identical plumes. (blanks denote downdrafts; lines denote updrafts; and arrows indicate direction of plume motion)

To insure that the transverse dimension of a plume updraft does not exceed the dimensions of the environmental regions (downdraft plus inactive area), the length, a_e, and width b_e of the "environment" are given by:

$$a_e = r b \left[\frac{1-A_p}{A_p}\right]^{1/r}$$

$$b_e = b \left[\frac{1-A_p}{A_p}\right]^{(1-1/r)}$$

The time evolution of the array would show updrafts appearing for a period of t_{active} and then shutoff for t_* in such a fashion that $A_p(=na)$ remains constant.

4. The interpretation of the plume formation layer

The nature of the interaction between the burst and sweep at the surface associated with the plume is complicated and not well understood. In the height ($0 < z < L/2$) the plume gathers the buoyancy and momentum of turbulent bubbles which predominate in mixed convection. Davison (1974) devised a heuristic model of the lower plume structure and showed with some success that both the shape factor (r) and translation velocity (U_{tr}) can be uniquely chosen to maximize the heat transport. A similar model is employed here to find a unique relation between the surface layer heat flux, plume translation speed, plume vertical velocity and shape factor, r, evaluated at $z=L/2$.

Figure 15, a schematic cross section along the plume

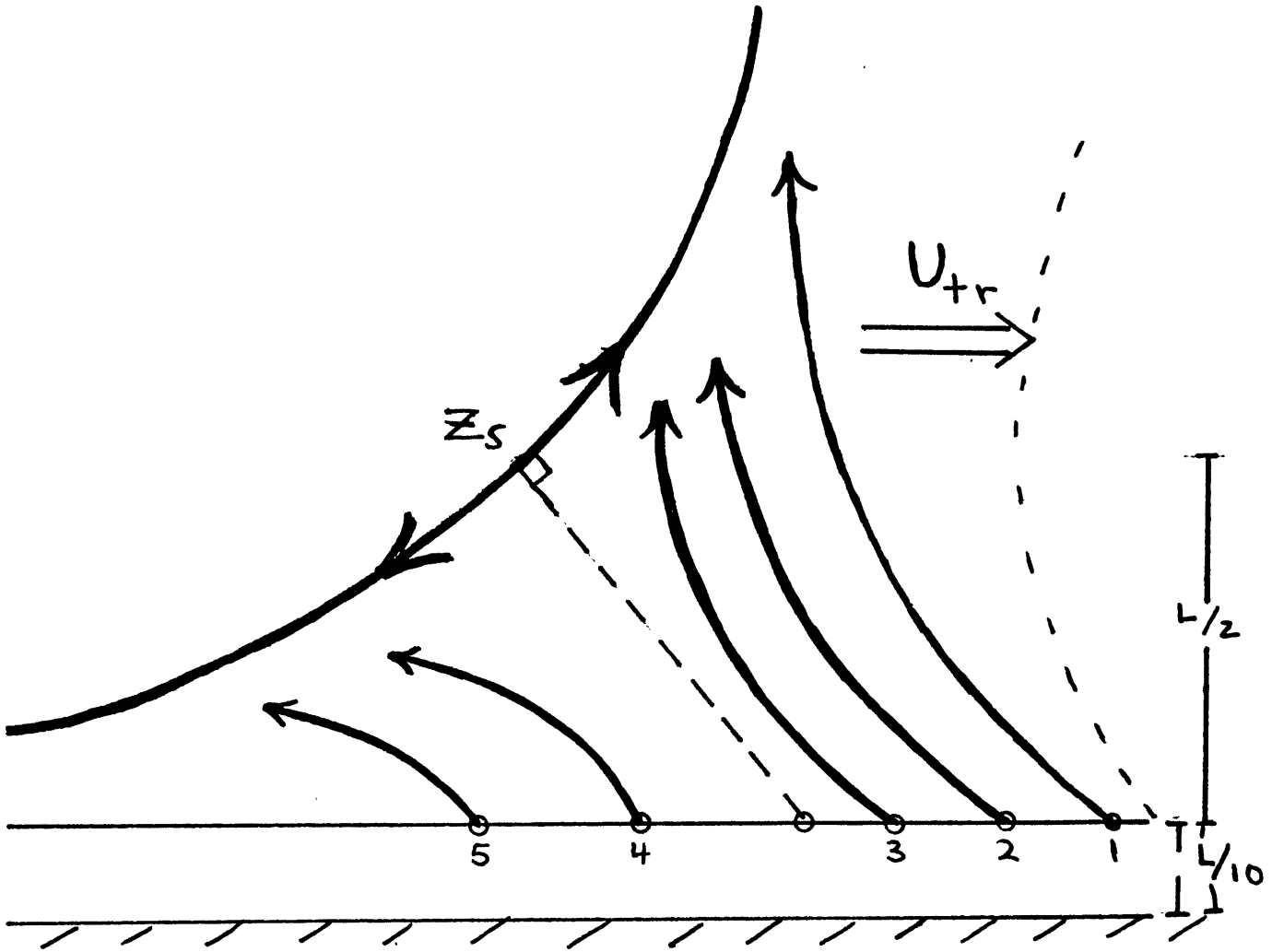

Figure 15. Vertical cross-section along a plume centerline with parcel trajectories drawn with respect to the plume translation.

centerline shows the trajectories of various parcels with respect to the translating plume. The passage of the plume triggers the release of potential energy near the surface due to the low pressure produced by vertical acceleration. The height where plume formation is complete (z=L/2), is also the level of the stagnation point that separates active air, flowing into the plume, and passive air, remaining near the surface. The numbered circles represent parcels of air whose trajectory relative to the translating plume is indicated. Parcel 1, having the greatest buoyancy of those tagged is the first to be drawn into the plume. Parcels 2 and 3 follow. However, parcels 4 and 5 do not have sufficient buoyancy and do not rise into the plume base. The trajectory normal to the plume surface at z_s represents a critical buoyancy level that separates active from passive parcels. This parameterization given a translation speed, plume separation, and surface heating rate predicts the fraction of available parcels that become activated.

Davison (1974) finds that most of the plume heat and mass flux is concentrated in a convergence zone of thickness ℓ parallel to the rearward edge, as shown in Figure 16. He finds from observations that the following relation holds for the majority of plumes sampled:

$$z_s \doteq 2(z_c - z_p)$$

where $z_c \equiv$ height of the convergence zone boundary perpendicular to the front at z_s. $z_p \equiv$ height of buoyant parcel

generation $\lesssim 0.1L$.

The convergence zone thickness is approximated by:

$$\ell = 2 \cdot \frac{\text{Area of convergence zone}}{\text{Perimeter of convergence zone}} = \frac{r \cdot b}{1+r}$$

From the geometry of Figure 16, one finds the slope of the rearward edge at the stagnation point:

With $z_s = L/2$ and $z_p = 0.05\,L$

$$\Phi_s = \sin^{-1}\left(\frac{0.2\,L}{\ell}\right)$$

$$= \sin^{-1}\left(\frac{0.2\,L\,(1+r)}{b\,r}\right)$$

In order for a parcel to become active, its trajectory must be steeper than the critical slope. Therefore,

$$\left|\frac{w_B}{U_{+r}}\right| \begin{matrix} < \\ = \\ > \end{matrix} \tan\Phi_s \qquad \begin{matrix} \text{inactive} \\ \text{critical} \\ \text{active} \end{matrix}$$

where the vertical bubble velocity w_b can be written:

$$w_b \doteq \frac{w_{b z_p}}{2} + \frac{1}{2}\left[w_{b z_p}^2 + 4g\frac{(z_s - z_p)}{\bar{\Theta}} T_b'\right]^{1/2}$$

The critical buoyancy can now be evaluated as:

$$T'_{bc} = \frac{(2 w_{bc} - w_{b z_p})^2 - w_{b z_p}^2}{4 (z_s - z_p) g / \bar{\Theta}_o}$$

or, since the initial vertical velocity is negligible,

$$T'_{bc} \doteq \frac{w_{bc}^2 \bar{\Theta}_o}{(z_s - z_p) g} = \frac{(U_{+r} \tan\Phi_s)^2 \bar{\Theta}_o}{g\,(0.495)\,L}$$

Take the bubble temperature perturbations as normally distributed about a mean which in turn is determined by the heating at the upper edge of the mechanically mixed region.

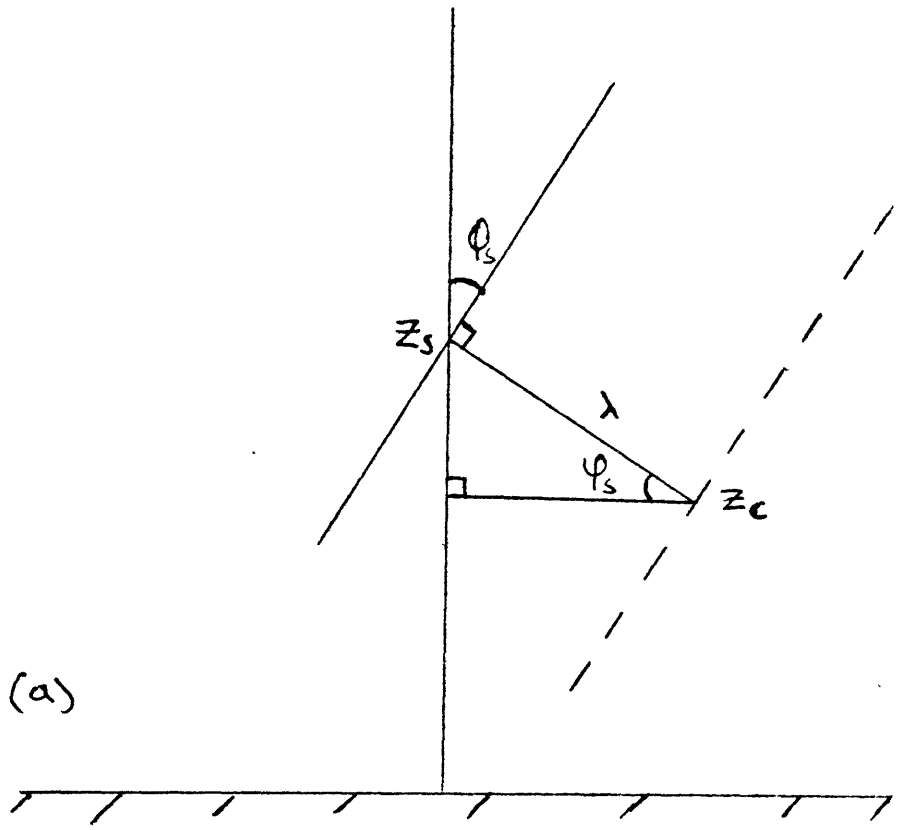

Figure 16.
a) Geometry of the convergence zone in the viscinity of z_s.

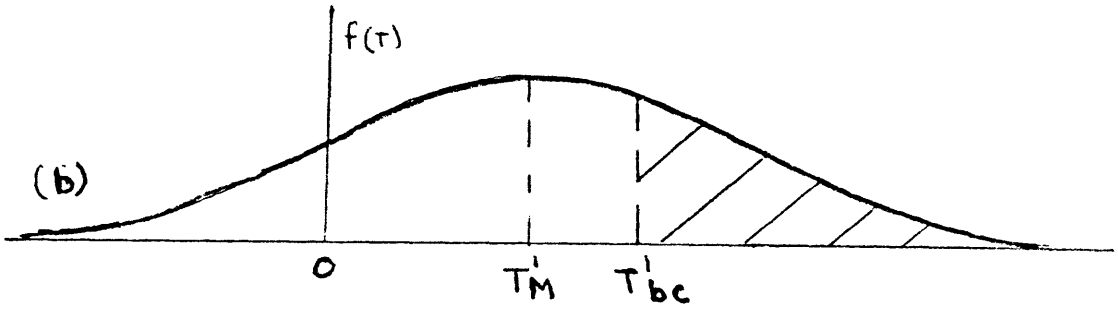

Figure 16.
b) A Gaussian distribution of parcel temperature perturbation centered about T'_M. The shaded portion ($T' > T'_{bc}$) is the fraction of active elements.

(Khalsa and Businger (1977) find a log-normal distribution of temperature within the surface layer. The gaussian is chosen here for simplicity but the method outlined can easily be extended.) The violent mixing due to plume passage renders the formation layer nearly neutral, so the bubble temperature perturbation is due principally to surface heating. The average bubble has an excess temperature of:

$$T_M' = \bar{\pi}^{1/2} f_o \lambda^{-1} h \left[\exp(-\hat{z}^2) - (\pi\hat{z})^{1/2} \operatorname{erfc} \hat{z}\right]$$

evaluated at z=0.1L,

where $h = 2(\kappa t')^{1/2}$

$\hat{z} = z/h$

$t' = a_e / U_{tr}$

The fraction of active parcels is expressed by the probability that the bubble temperature exceeds the critical perturbation. Specifically: (σ_T = standard temp. deviation)

$$Pr(T_b' > T_{bc}') = \qquad (24)$$

for $T_{bc}' > T_M$ $\quad \frac{1}{2}\left(1 - \operatorname{erf}\left(\frac{T_{bc}' - T_M'}{\sigma_T}\right)\right)$

for $T_{bc}' < T_M$ $\quad \frac{1}{2}\left(1 + \operatorname{erf}\left(\frac{T_{bc}' - T_M'}{\sigma_T}\right)\right)$

The probability calculation is displayed in Figure 16b. It appears that the faster the plume translates, the less the likelihood that any parcel will gain sufficient buoyancy to become active.

The bubble probability is extended to indicate the

fraction of available air that is ingested from the sub-layer into the plume. The conservation of volume (density variations are minor) requires that:

$$w_{p,L/2}\, a_p = D\, b\, U_{tr}\, P_r(T'_b > T'_{bc}) + u_R\, 2b(1+r)$$

The first term on the right represents the active bubbles while the second term arises from a vortex ring-like circulation. When the mean wind is very light, $U_{tr} \rightarrow 0$ and:

$$u_R \equiv u_o = \frac{w_{p\,L/2}\, a_p}{2bD\,(1+r)}$$

Since the vortex ring circulation decreases in strength at the surface as U_t increases from zero let:

$$u_R = u_o(1-\nu) \quad \text{where} \quad \nu = \frac{X}{c+X}, \; X = \frac{U_{tr}}{u_o}$$

An equation for U_{tr} is thereby obtained.

$$U_{tr} = r\, w_{p\,L/2}\, \frac{b}{D}\left(P_r^{-1}(T'_{bc} > T'_{bc}) - \frac{c}{2(1+r)}\right)$$

In order not to allow negative translation velocities, let $c=2(1+r)$ to yield:

$$U_{tr} = w_{p\,L/2}\, r\, \frac{b}{D}\left(P_r^{-1}(T'_b > T'_{bc}) - 1\right) \qquad (25)$$

Equations (24) and (25) comprise a closed set that enables a determination of the plume translation velocity. Equation (25) is self consistant because as U_{tr} goes to zero, $T_b{}^1$ increases without bound such that $Pr(T_b{}^1 > T_b{}^1{}_c)$ approaches unity.

G. Evolution of the Mixed Layer

The entrainment at the upper bounds of the mixed layer can be approximated following Manton (1975) from the plume velocity and lag time between successive thermal plumes. At the inversion, the plume has little (negative or positive) buoyancy and is travelling at the asymptotic velocity, w_∞. The deceleration of the updraft as it impinges upon the stable layer can be approximated by: (subscript p is dropped)

$$\frac{dw}{dt} \doteq \left(\frac{\bar{\theta}_\infty}{\theta_s} - 1\right) g$$

where θ_s = temperature within the stable layer.
Accordingly, the penetration distance, $\mathcal{L}$, is given by:

$$\frac{1}{2} w_\infty^2 = \int_{z_1}^{z_i + \mathcal{L}} \left(1 - \frac{\bar{\theta}_\infty}{\theta_s}\right) g \, dz \, .$$

For example, a thermal element may penetrate a distance of 15 meters into the stable layer in 30 seconds at which time it has a large negative buoyancy. It subsequently mixes with the air below a height of $z=z_i + \mathcal{L}$. Another thermal element arrives at the inversion at intervals of t_*. The region denoted by $z_i < z < z_i + \mathcal{L}$ will become well mixed if the penetration time is small with respect to the plume lag time.

The volume flux into the stable layer is $A_p w$ such that the inversion mixing time is given by τ_i where

$$\tau_i \doteq \frac{\mathcal{L}}{A_p w_\infty} \, .$$

If $\tau_i/t_* \ll 1$, then all of the stable air in the region $z_i < z < z_i + \mathcal{L}$ is flushed into the mixed layer and replaced by plume air. Thus, a sharp inversion is formed at $z_i + \mathcal{L}$ where buoyancy forces suppress vertical mixing. The horizontal variation of the inversion height undulates between z and $z + \mathcal{L}$ as the plumes arrive at discrete intervals. If $\tau_i/t_* \gtrsim 1$, the plumes pass through a partially mixed region and the inversion is diffuse. A sharp inversion forms only when a layer stable enough to make $\tau_i \ll t_*$ is formed.

From these considerations the mean rise rate of the inversion is given by:

$$\frac{dz_i}{dt} = \frac{\mathcal{L}}{t_*}$$

The ratio of downward heat flux to upward heat flux at the surface is: $(Q_0 = u_* \theta_*)$

$$\frac{Q_{zi}}{Q_0} = \frac{\left(\bar{\theta}_s(z_i) - \bar{\theta}_\infty\right)}{Q_0} \frac{dz_i}{dt} \qquad (25)$$

$$= \frac{\left(\bar{\theta}_s(z_i) - \bar{\theta}_\infty\right)}{Q_0} \frac{\mathcal{L}}{t_*} .$$

(This ratio is assumed to be constant in the majority of mixed layer models.) For the limit of a strong inversion (25) reduces to:

$$\frac{Q_{zi}}{Q_0} = \frac{\bar{\theta}_\infty w_*^2}{2 g t_* Q_0} \qquad (26a)$$

The mean heating rate of the mixed layer is therefore approximately:

$$\frac{d\bar{\theta}^z}{dt} \doteq \frac{u_* \theta_* \left(1 + Q_{zi}/Q_0\right)}{z_i} \qquad (26b)$$

For example, with $Q_H/Q_o = 0.2$, $Q_o = 0.1$ m°K/s, and $z_i = 1000$ m, the layer heats at a rate of 0.45°K per hour. Equation (26) is likely to be a slight overestimate when the inversion level is steadily increasing throughout the daylight hours.

If the stability of the inversion is given as $\Gamma \equiv \frac{1}{\theta_s} \frac{\partial \bar{\theta}_s}{\partial z}$ and the temperature jump is defined as $\Delta = \bar{\theta}_s - \theta_\infty$ then we can write:

$$\frac{d\Delta}{dt} = \frac{d\bar{\theta}_\infty}{dt} + \bar{\theta}_s \Gamma \frac{dz_i}{dt} \qquad (27)$$

For the case where $\Delta \to 0$, there is no inversion, such that from (26): $\frac{d\bar{\theta}_\infty}{dt} = \frac{Q_o}{z_i}$

The heat flux balance requires that:

$$z_i \frac{d\bar{\theta}_\infty}{dt} + Q_{z_i} + Q_o = 0$$

Therefore, in the limiting case of weak inversion the boundary layer rise rate is given by:

$$\frac{dz_i}{dt} = \frac{u_* \theta_*}{\bar{\theta}_s \Gamma z_i} \qquad (28)$$

For a distinct inversion the penetration depth, $\mathcal{L}$, can be approximated by assuming a linear temperature profile. Using

$$\mathcal{L} \doteq w_\infty / (\Gamma g)^{1/2}$$

and (27) we obtain the inversion strength rate equation:

$$\frac{d\Delta}{dt} = -\frac{u_* \theta_* (1 + Q_{z_i}/Q_o)}{z_i} + \frac{\bar{\theta}_\infty w_\infty}{z_*} \left(\frac{\Gamma}{g}\right)^{1/2} \qquad (29)$$

The inversion increases when:

$$\Gamma > \left(\frac{Q_o (1 + Q_{z_i}/Q_o)}{\bar{\theta}_\infty w_\infty}\right)^2 \left(\frac{g z_*}{z_i^2}\right)$$

implying that a less stable layer is needed to cap a deep mixed layer than a shallow one. The boundary layer rise rate for $\gamma_i << t_*$ is given by:

$$\frac{dz_i}{dt} = \frac{w_{*0}}{t_* (\Gamma g)^{1/2}} \qquad (30)$$

This rate is generally faster than the no inversion case governed by (28). In practice, the strong and weak inversion rise rates ((28) and (30)) provide limits that envelop the observed rise rate.

CHAPTER III

REAL DATA EVALUATION

To examine the performance of the plume model against observations and numerical simulations, we choose the data of Day 33 of the Wangara experiment (Clarke, et. al., 1971). Although the observational procedure was designed to detect changes in the meso-structure of mean field quantities, the models of Yamada and Mellor (1975), Deardorff (1974) and Wyngaard and Coté (1974) provide sufficient information about the turbulent properties on which to base a comparison. On day 33 the weather is fair with a gentle surface wind of 2 to 3 m/s. The output of various models is compared at times of 1100, 1400 and 1600 local standard time (LST). The early morning and late evening periods are excluded in this initial test because the formation and erosion of the inversion layer are complex processes which are only crudely simulated in the present plume model. Figure 17 indicates that the transition from a stable to an unstable boundary layer occurs between hours 10 and 11. After this time the gradual but steady increase in the inversion height indicates that the form of convection does not change significantly. (Hereafter, Wyngaard's moment-closure model will be referred to as "m-c" and Deardorff's model as "3-D".)

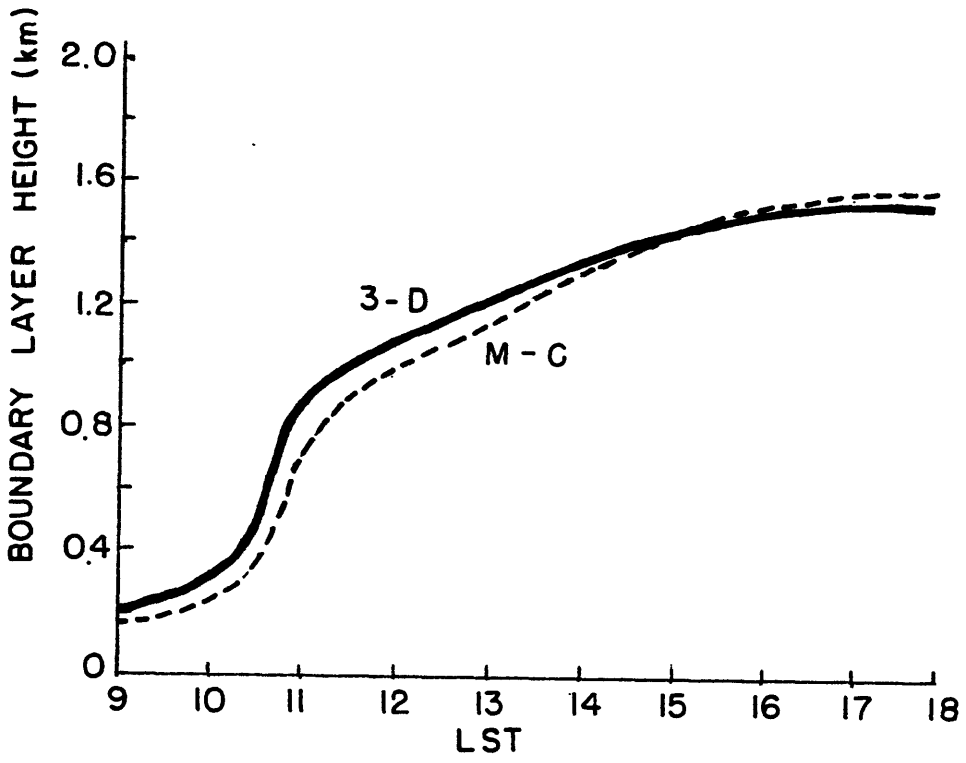

Figure 17. Boundary layer depth histories for the three dimensional (solid) and moment-closure (dashed) models on Day 33, Wangara (from Wyngaard and Cote, 1974).

A. The Evolution of the Mean Boundary Layer Structure

The plume model (or any parameterization) requires that the mean field quantities be stationary with respect to the time-scales associated with the convection. For example, the equations of horizontal motion can be written in terms of the mechanical stress.

$$\frac{dU}{dt} = -f(V-V_g) + \frac{\partial \overline{uw}}{\partial z}$$

$$\frac{dV}{dt} = f(U-U_g) + \frac{\partial \overline{vw}}{\partial z}$$

If the field is horizontally homogeneous and there is no mean vertical motion, then to parameterize the mean wind in terms of mechanical stresses requires that:

$$\left|\frac{\partial U}{\partial t}\right| << \left|f(V-V_g)\right| \simeq \left|\frac{\partial}{\partial z}\overline{uw}\right|$$

$$\left|\frac{\partial V}{\partial t}\right| << \left|f(U-U_g)\right| \simeq \left|\frac{\partial}{\partial z}\overline{vw}\right| \qquad (31)$$

For $|U-U_g| \sim 1$ m/s ; $f = 10^{-4}$ sec^{-1}

$$\left|\frac{\partial U}{\partial t}\right| << 10^{-4} \text{ m/s}^2 = 0.36 \text{ m/s/hour}$$

This condition is not generally met especially when geostrophic wind shear is such that a deepening of the mixed layer causes the entrainment of higher momentum air. On Day 33, $\frac{\partial}{\partial t}(U,V)$ happens to be small. In a numerical weather prediction model the time rate of change of the wind at each level can be ascertained from the previous time-step so that this term

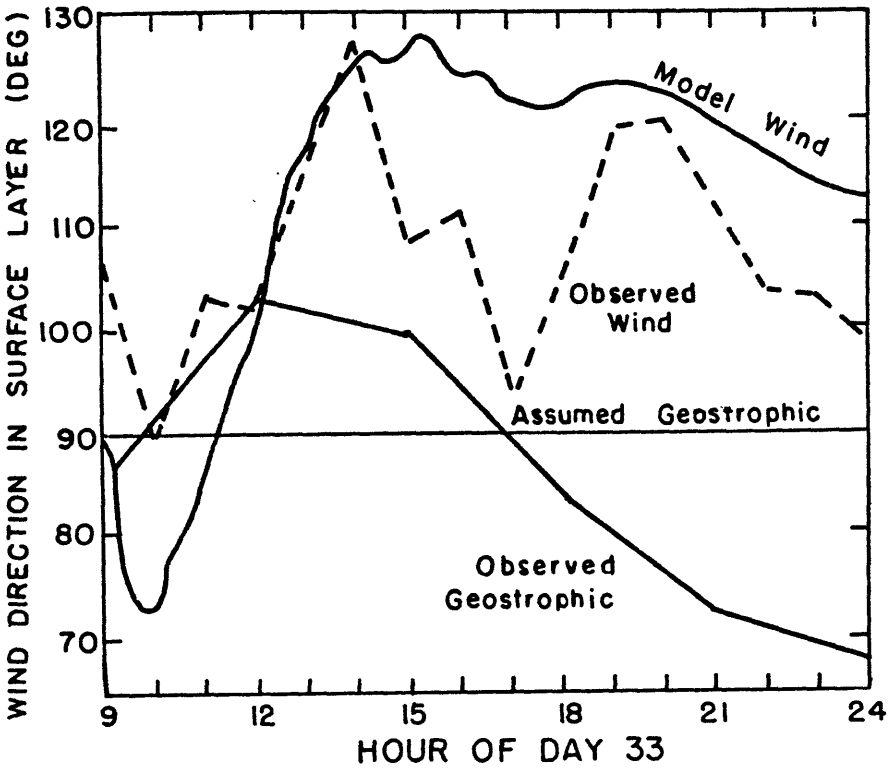

Figure 18. Surface wind direction (degrees from north) during Day 33, (from Deardorff, 1974a).

need not be an operational source of error.

The partition of the stresses into geostrophic departure and geostrophic shear components may also be fallacious. Figure 19 (taken from m-c models) shows that within the mixed layer there is very little vertical shear of a 2.4 m/s wind. According to equation (31) and Figure 20, the geostrophic departure of the longitudinal velocity, $U - U_g$, is zero about midway through the mixed layer where $\frac{\partial}{\partial z}\overline{v'w'} = 0$. Since $\overline{G}^z = 4/5$ m/s, the cross isobar flow angle must be 35^o which is verified in Figure 18. Although this angle is consistent with the 3-D and m-c models it is not observed. The stress profiles and mean wind corresponding to zero geostrophic wind shear derived from the m-c model are displayed in Figures 21 and 22. Apparently, within the mixed layer the mean winds are not appreciably affected by the geostrophic shear, although the minor turning with height ($\frac{\partial}{\partial z} V > 0$ in Figure 19b) is virtually eliminated. The m-c model on which the stress parameterization is based has a rigid lid at the inversion height. The $\overline{uw}$ profile in Figure 22 is linear but does not vanish at the inversion as we have assumed in Figure 9. The reason for this unexpected aberrent behavior has not been adequately explained by Wyngaard and Cote (1974). Therefore, a more sophisticated parameterization for the stress profiles, which takes into account the stress at the inversion must be developed for the plume model.

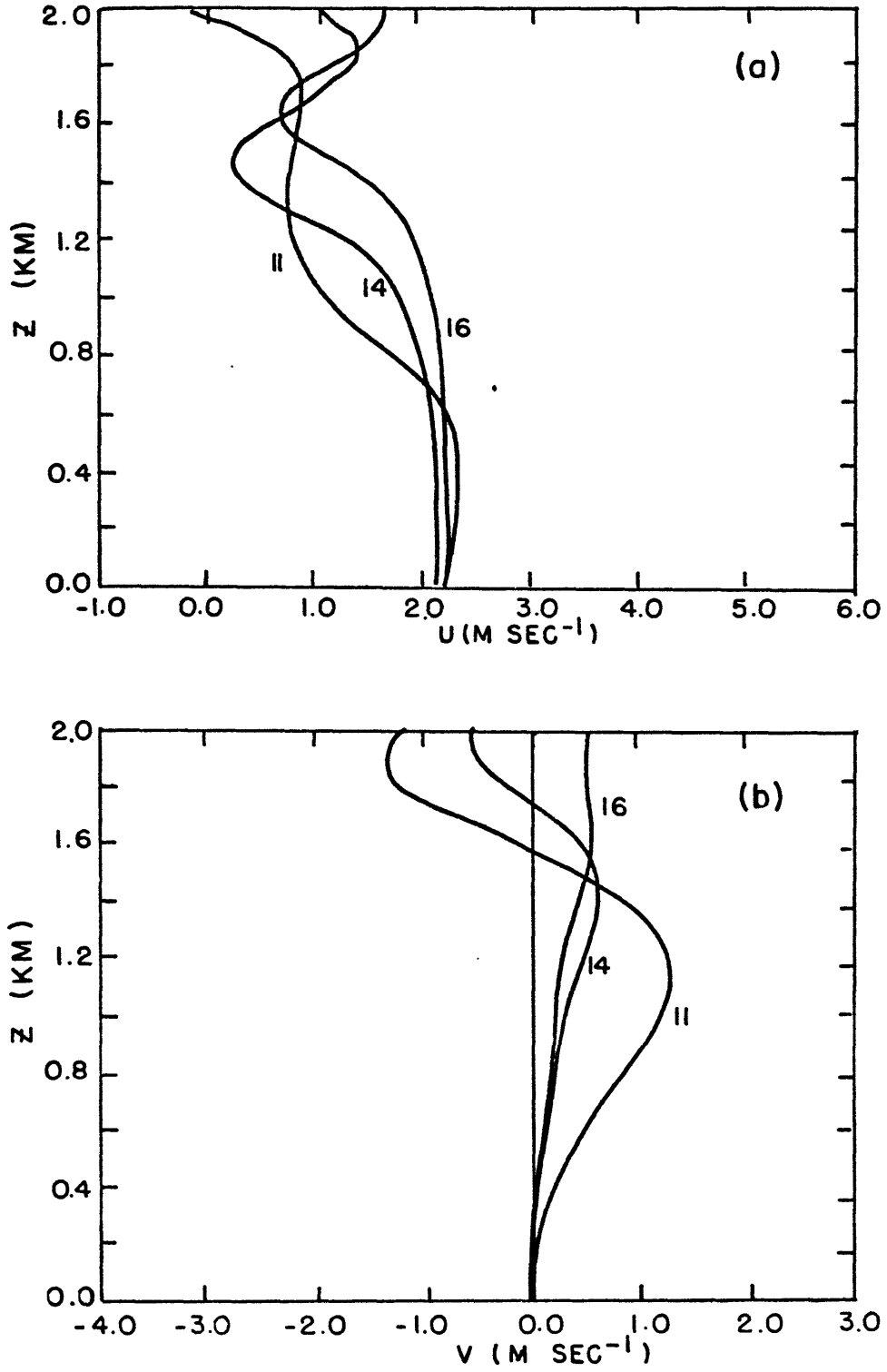

Figure 19. Calculated mean wind profile from moment-closure model, a) longitudinal component, b) transverse component (from Wyngaard and Cote, 1974).

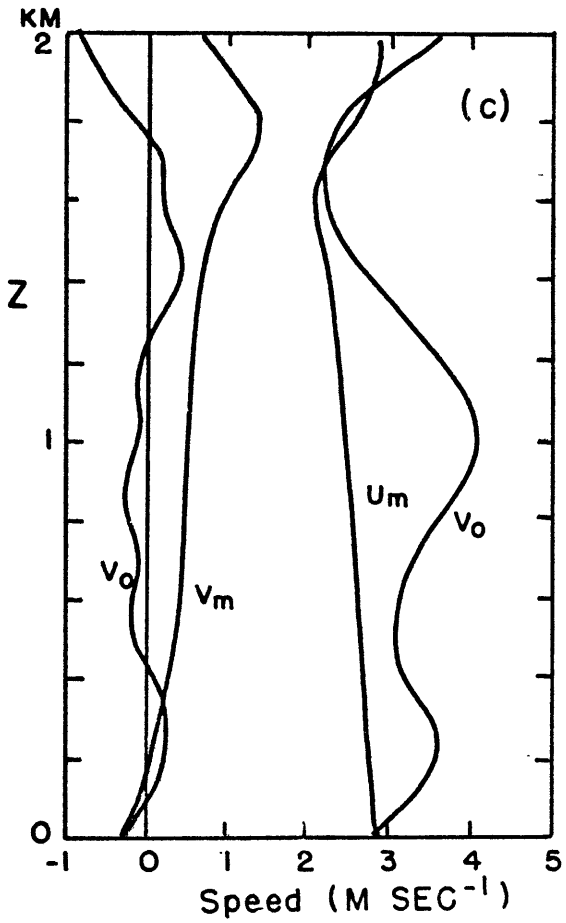

Figure 19.
c) Mean observed and calculated wind profiles for hour 15 (from Deardorff, 1974).

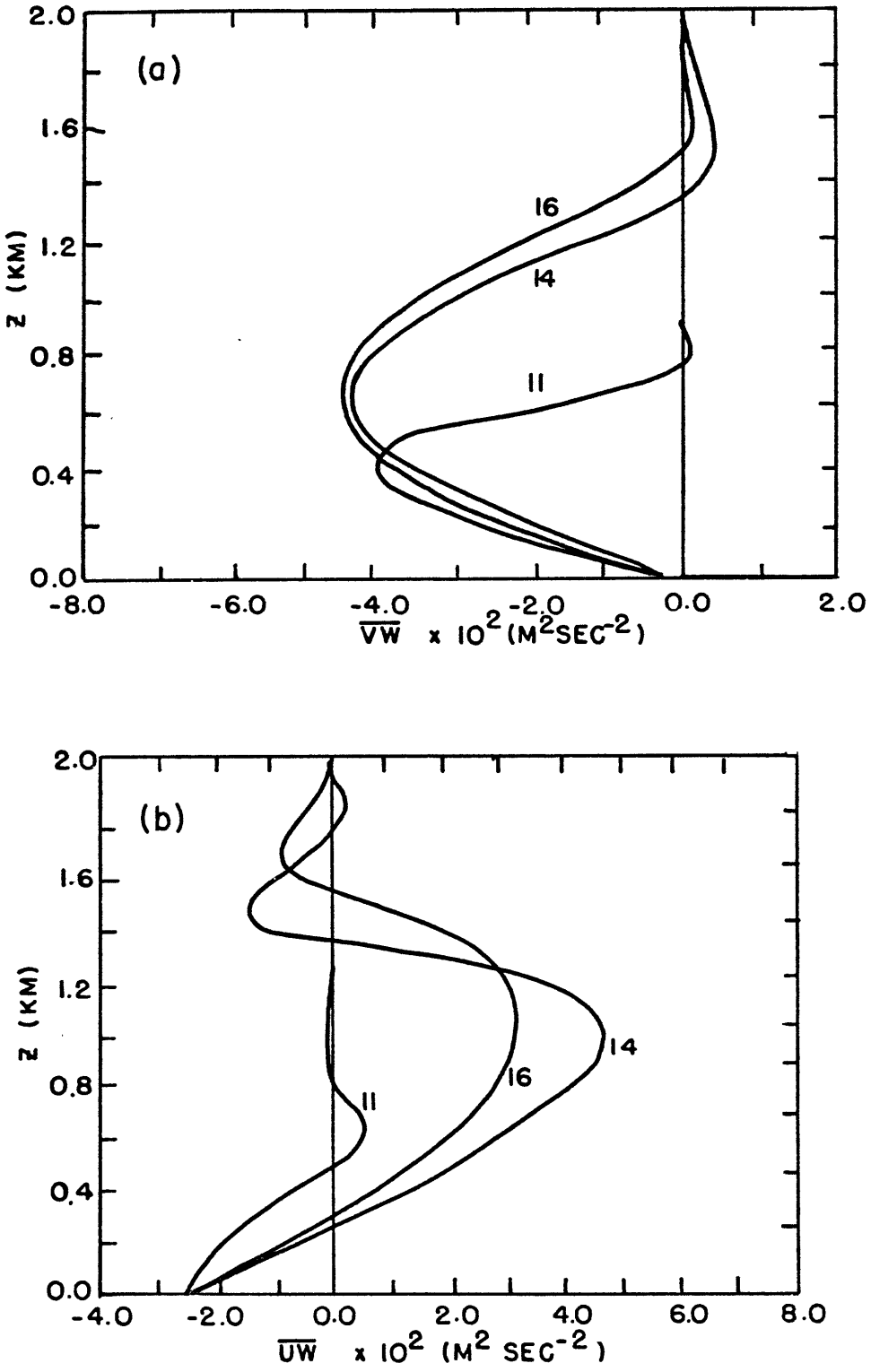

Figure 20. Calculated profiles of the a) transverse, b) longitudinal momentum flux from the moment-closure model, (from Wyngaard and Cote, 1974).

For hours 12 and 16 the magnitude of $\overline{vw}$ in Figure 21b is negligible throughout the convection layer. Therefore, the cross-isobar flow angle in the mixed layer can be obtained from:

$$\mu^2 - \frac{f z_i}{c_D G}\mu - 1 = 0 \; ; \quad \mu = v_g / G$$

where z_i is the height where a linear extrapolation of $\overline{u'w'}$ from the surface becomes zero. A cross-isobar angle of 35^o and a surface wind of 2.5 m/s implies that $u_* = 0.34$ m/s which does not agree with the quoted friction velocity of 0.17 m/s. The application of surface layer similarity to instantaneous surface stresses by Deardorff (1974) is likely to be involved in the discrepancy.

A summary of the Wangara Day 33 data that is externally imposed can be found in Table 5. In order to obtain consistency between the formulation for the drag coefficient at $z=L/2$ and the independently determined roughness-height z_o, the parameter $\alpha \left(\equiv - \frac{\partial \overline{uw}}{\partial z} / \frac{\partial \overline{vw}}{\partial z} \right)$ was set at -0.4. (The moment-closure model of Wyngaard et. al. (1974) is not particularly helpful in this case because stress profiles at only two values of z_i/L are available.) The derived quantities that serve as direct input into the model appear in Table 6. Note that the variation of the wind speed follows the observations with some accuracy. A general theory for the evaluation of α within the surface layer is required. Here, α is negative with the understanding that the wind at $z=L/2$ is likely to be sub-geostrophic. By surface layer

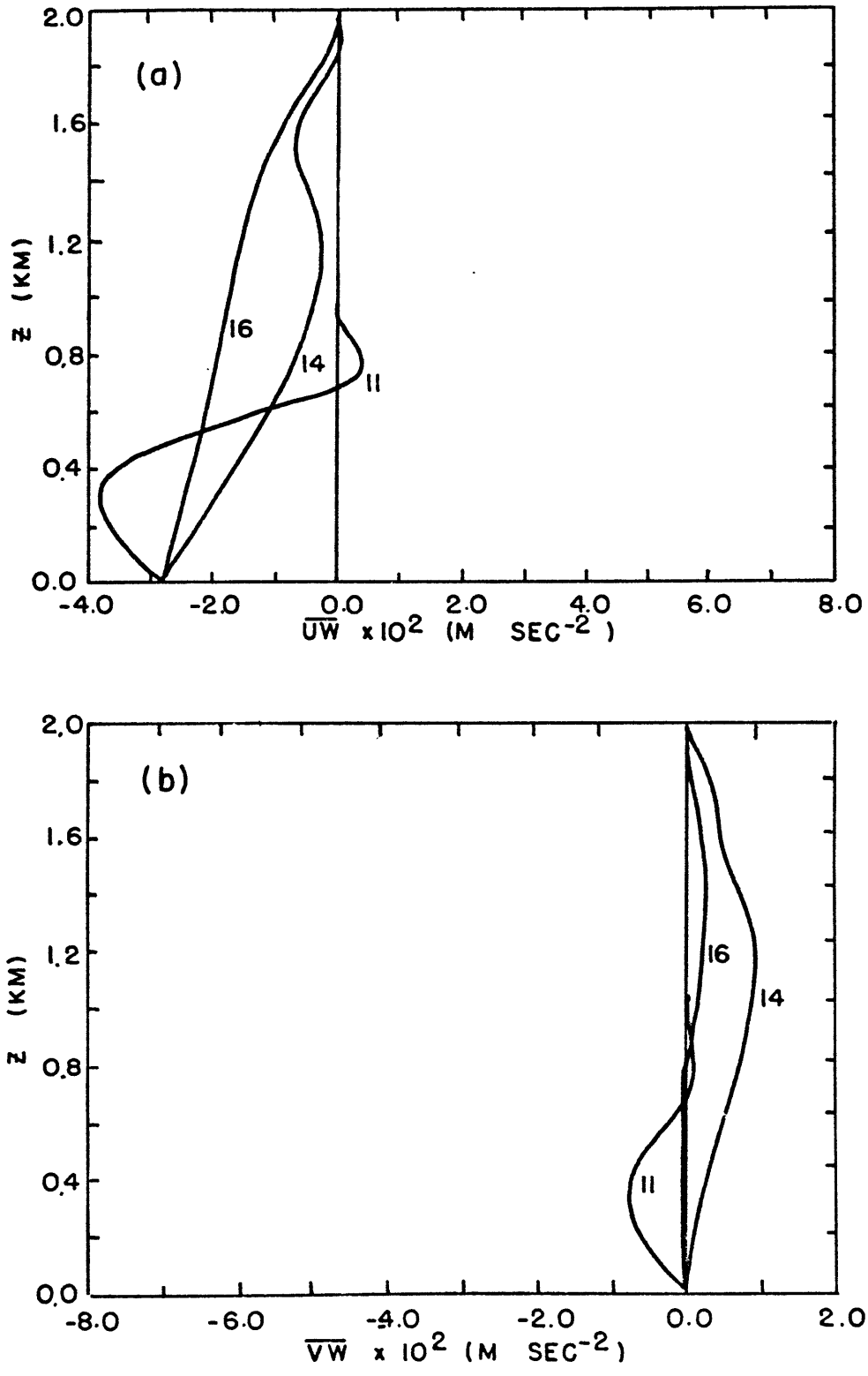

Figure 21. Moment-closure calculated profiles of a) longitudinal, and b) transverse momentum flux for Day 33 with no thermal wind (from Wyngaard and Cote, 1974).

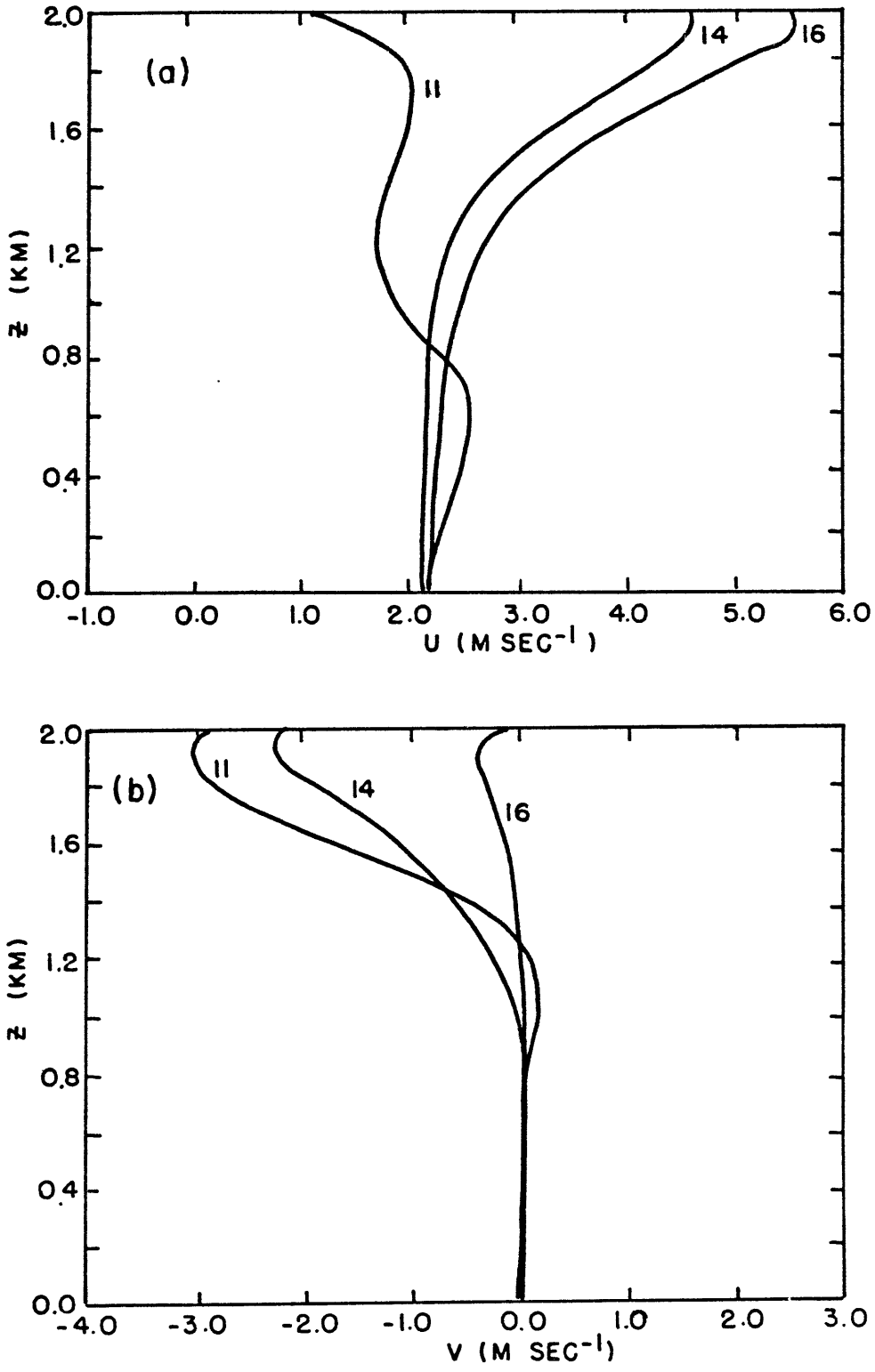

Figure 22. Moment-closure calculated mean wind profiles for a) longitudinal, and b) transverse components with no thermal wind (from Wyngaard and Cote, 1974).

TABLE 5

External data for Day 33, Wangara

	LST		
	1100	1400	1600
Inversion height, z(m)	1033	1233	1366
Surface virtual potential temperature, θ_o (^oK)	283.5	285.5	286.5
Mean boundary layer Geostrophic components			
U_g (m/s)	-3.85	-4.37	-4.71
V_g (m/s)	1.3	0.98	0.75
Average thermal wind			
U_g (m/s)	3	3.24	3.4
V_g (m/s)	-0.135	-0.19	-0.27
Roughness height, z_o(m)	6×10^{-3} to 2×10^{-2}		

TABLE 6

Derived model parameters evaluated at a height of $z = L/2$

	LST		
	1100	1400	1600
Cross isobar angle at surface, ϕ_o (deg)	8	7.2	6.9
Mean observed angle, (11-17 LST)	10	10	10
Geostrophic Components			
U_g (m/s)	4.02	4.44	4.73
V_g (m/s)	0.57	0.56	0.57
Surface wind at $z = L/2$, U(m/s)	2.60	3.04	3.34
Observed wind speed at $z = L/2$, U(m/s)	2.4	3.0	3.8
Monin-Obukov length, L(m)	6.34	6.64	8.39
Friction velocity, u_*(m/s)	0.2	0.23	0.26
Temperature scale, θ_*(^oK)	0.525	0.66	0.67

theory we have $U_{L/2} = \frac{u_*}{k}\left[\ln\left(\frac{z}{z_o}\right) - \psi_M\right]\Big|_{L/2}$ which in this case implies that $L/z_o \sim 500$. This is in reasonable agreement with the observed range of L/z_o:

$$317 < L/z_o < 1400.$$

Therefore, α is chosen such that $U_{L/2}$ calculated from the friction velocity is in fair agreement with

$$U = U_g + (1/\alpha)\, V_g.$$

The mean wind in the surface layer follows equation (33) until a height of 4L where the mixed layer stress profiles are extrapolated from Figure 9. For example, Figure 20 shows the vertical variation of the mean wind in the planetary boundary layer using $\overline{vw}$ for an easterly wind. Since the slope of the modeled longitudinal stress, $\overline{uw}$, does vary significantly with height, the transverse velocity, v, is identically zero. The highly structured observations of mean wind (Figure 19c) indicate complex structure with height that does not follow the idealized profile in Figure 23. It is apparent that the present stress parameterization is not sufficient to determine the structure of the mean wind profile. This is because the inversion is an active surface where stresses can be significantly different from zero. Here, apparently $\overline{vw}$ remains negative throughout the mixed layer so that the mean wind remains sub-geostrophic.

The potential temperature profiles at 3 hour intervals shown in Figure 24 are essentially adiabatic upwards from a few hundred meters. The height where the gradient of potential

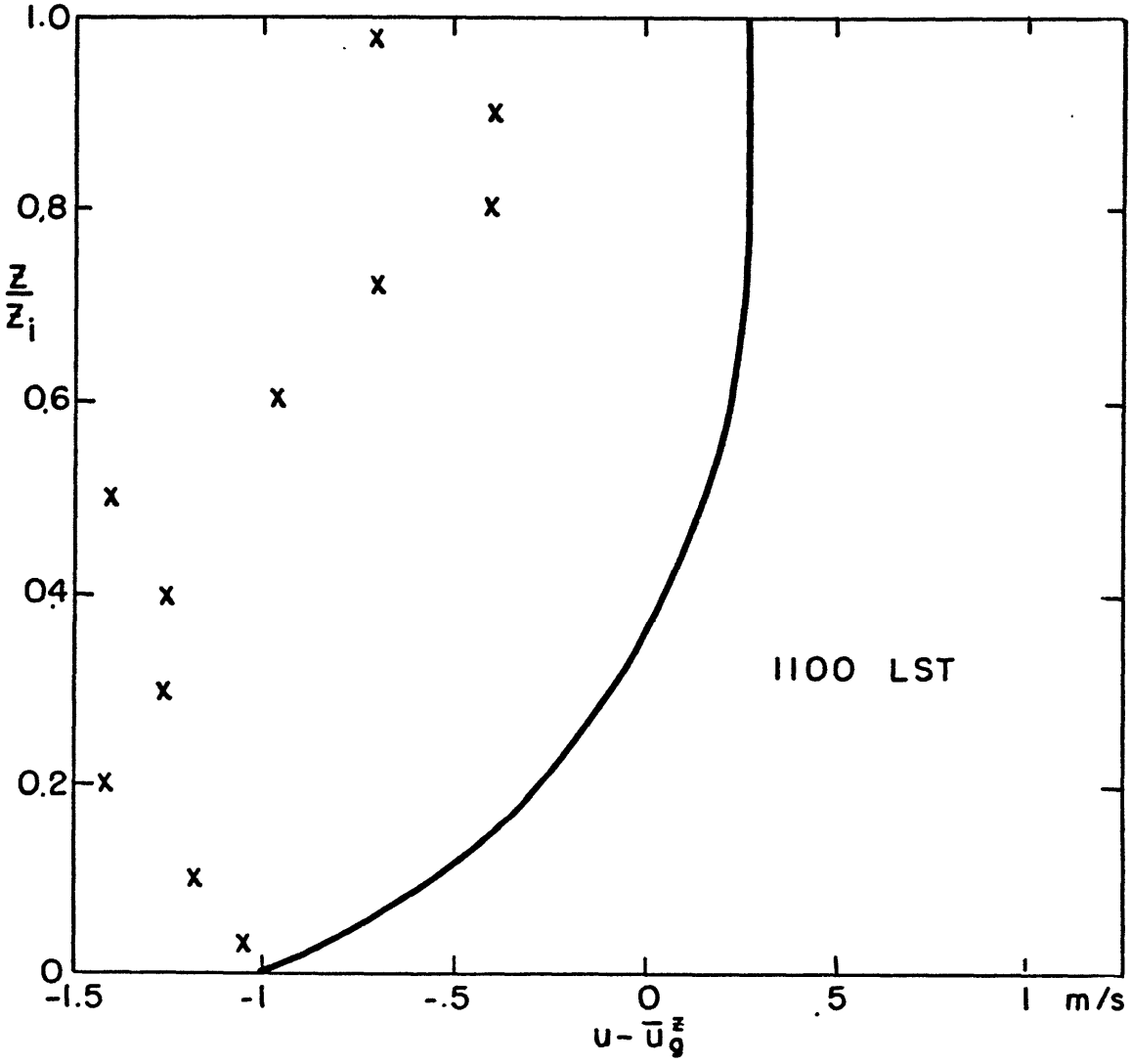

Figure 23. Comparison of model generated (solid line) and observed (X's) geostrophic departure at 1100 LST Day 33.

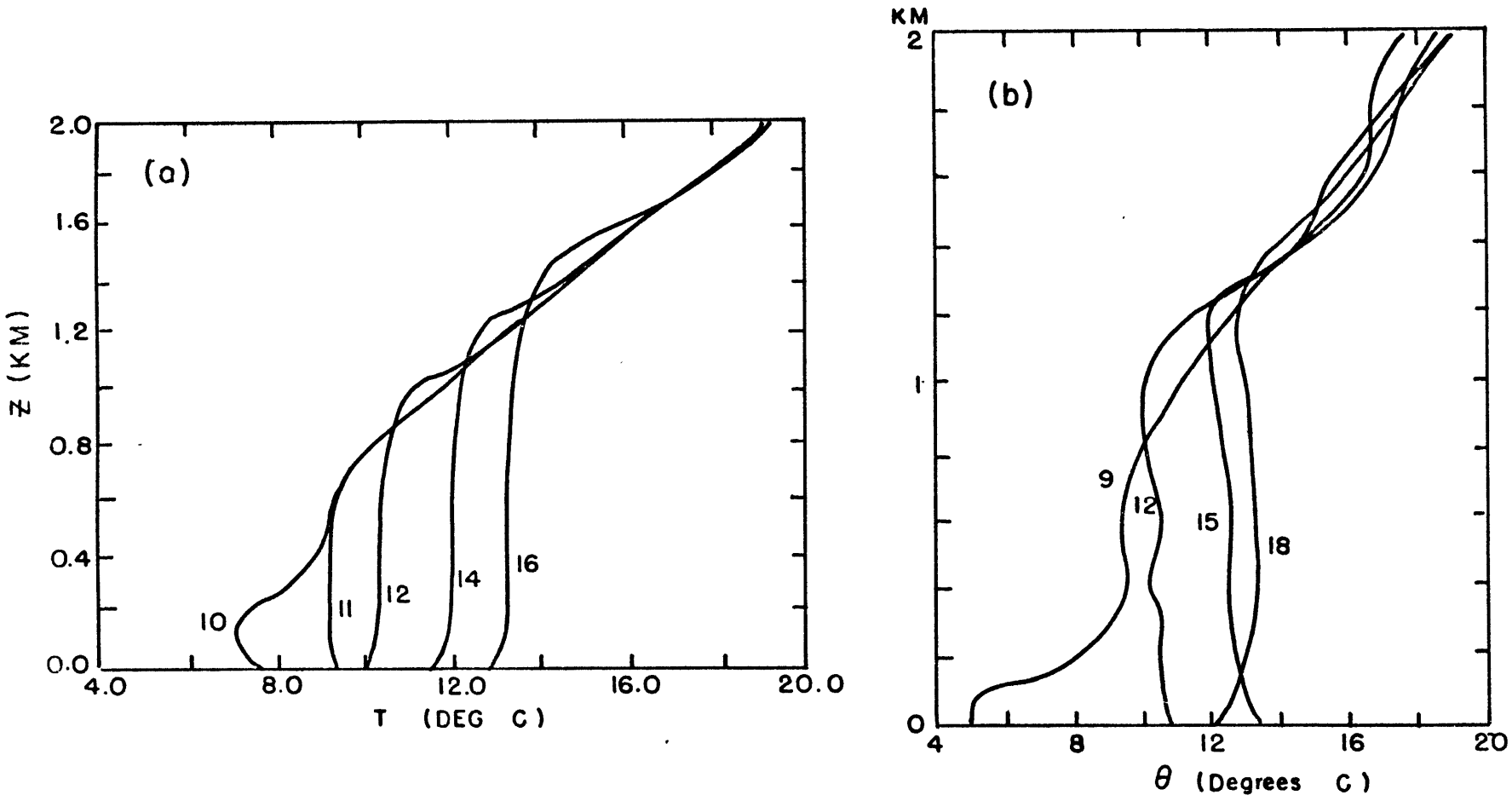

Figure 24.
a) Mean virtual potential temperature calculated from the moment-closure model for Day 33, Wangara (from Wyngaard and Cote, 1974).
b) Observed virtual potential temperature profiles for Day 33, (Clarke, et. al., 1971).

temperature vanishes marks the effective "boundary" between the surface and mixed layers. In the model this occurs at about eight Monin-Obukov lengths above the surface. For 1200 and 1500 LST, Figure 24b shows that the surface air is 1 to 1.5°K warmer than the constant mixed layer temperature. The 1200 sounding is significantly stable above 800 meters indicating that the inversion is still intensifying. The profiles derived from the model (Figure 25) are slightly stable above z=10L ($\frac{\partial \bar{\theta}}{\partial z} \sim 0.1$ °K/km) and superadiabatic in the lowest 30 meters. In comparison the moment closure model produces a slightly stable lapse rate within the mixed layer but also produces an unrealistic increase in stability near the surface.

The horizontally averaged heat flux is constant in the surface layer according to the surface convection model. The temperature and vertical velocity variances are computed from the plume variables according to:

$$\overline{(w,\theta)^2} = (w,\theta)_p^2 (1+\eta) A_p + (w,\theta)_e^2 (1+\xi)(I_e - A_p)$$

where $\eta = 0.4$, $\xi = 0.1$, $I_e = 0.83$, $A_p = 0.4$.

The surface heat flux can also be expressed as:

$$Q_o = u_* \theta_* = w_p \theta_p (1+\eta') A_p + (I_e - A_p)(1+\xi') w_e \theta_e$$

This, however, implies that η', ξ' are negative. Essentially, this means that using a top-hat plume model and assuming a perfect corellation between the vertical motion and temperature

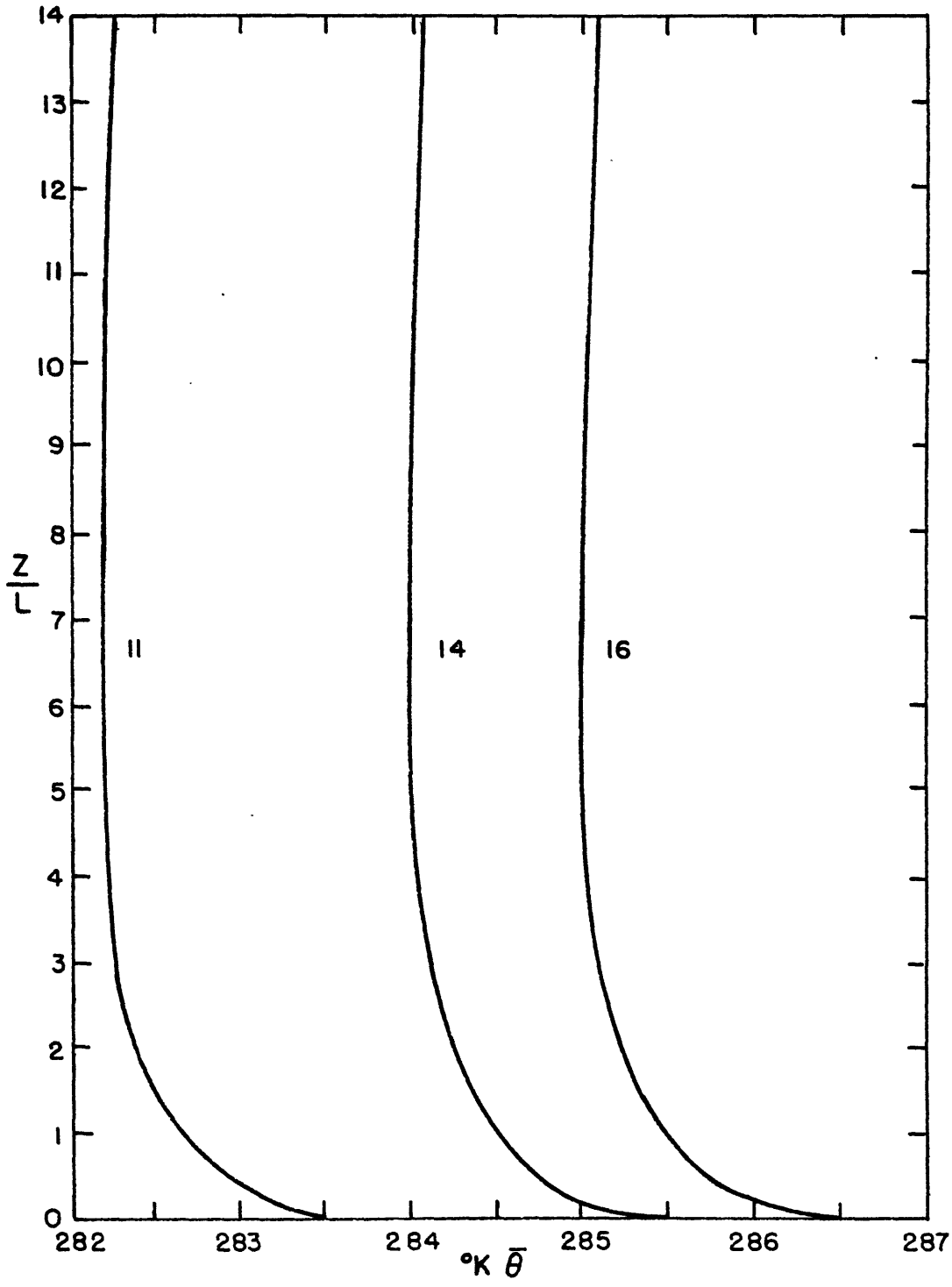

Figure 25. Temperature profiles in the lower boundary layer calculated by the plume model for Day 33, Wangara.

perturbations overestimates the heat flux. Therefore, the interaction events observed by Antonia (1977) cannot be entirely neglected.

The derived heat fluxes for the mixed layer are shown in Figure 27. The flux decreases less than 10 percent of the surface value at the inversion height. The greatest heating rate ($-\frac{\partial}{\partial z}\overline{w\theta}$) occurs in the lower portion of the mixed layer where the buoyant elements cool rapidly with height. The curvature of the $\overline{w\theta}$ profile becomes less pronounced with decreasing σ . A linear heat flux profile, an established property of convectively mixed layers, is required to maintain the nearly neutral potential temperature profile. Relative heating implied in Figure 27 results in a destabilization of the lower mixed layer. The observations in Figure 24b indicate that between 1200 and 1500 LST, a slightly unstable lapse rate develops between the surface and 0.3 km. The heat flux divergence (from Figure 23) indicates a relative heating rate of 0.5^{o}K/hour at 1400 while the observed rate is about 0.3^{o}K/hour. The paradox is that while the derived fluxes imply a destabilization, the model maintains a nearly neutral lapse rate. This is a direct result of the artificiality of the closure assumption that relates the local lapse rate and plume buoyancy through the free parameter, σ .

The heat flux profiles from the m-c and 3-D models displayed in Figure 26 are essentially linear from the top

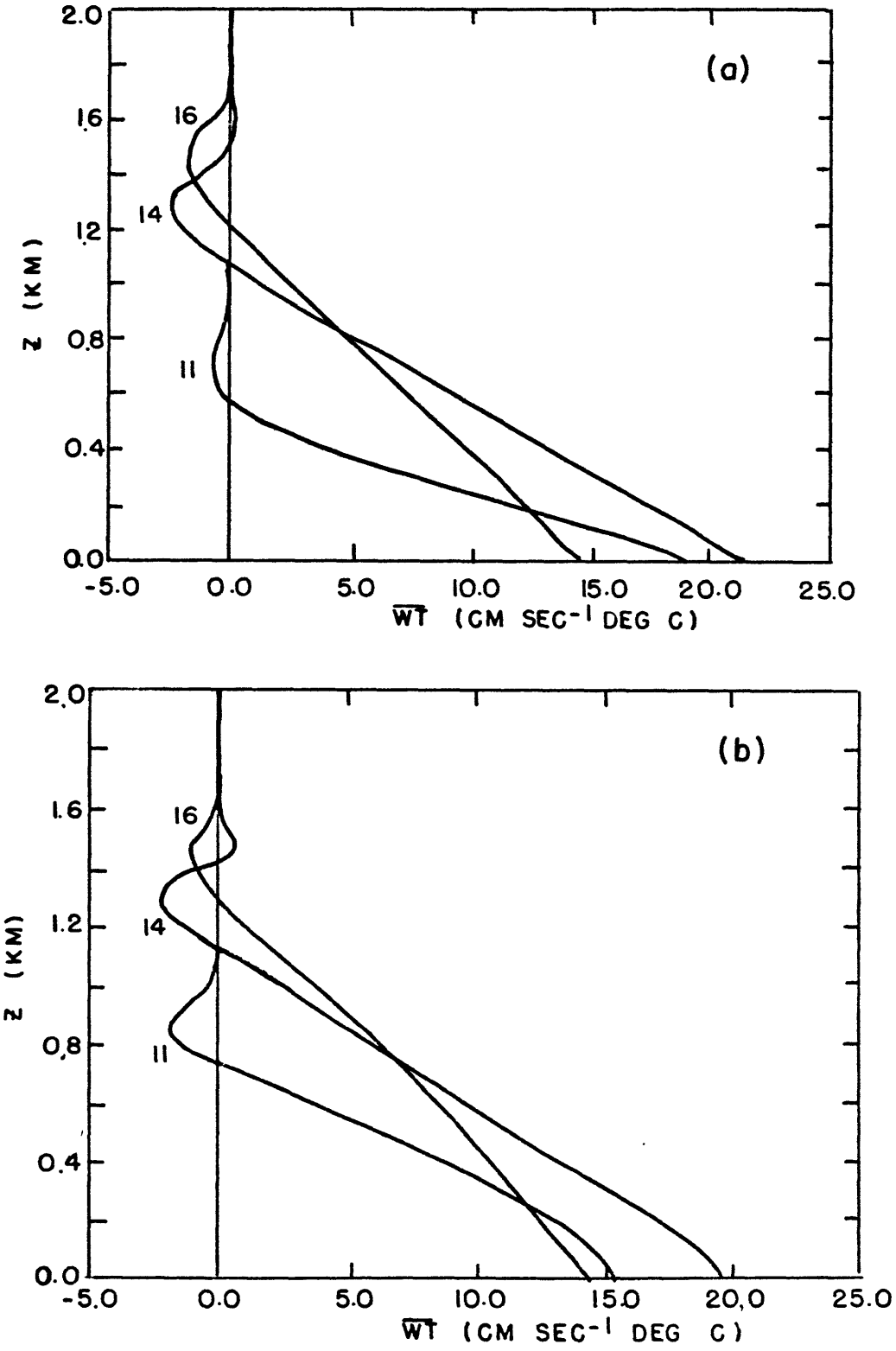

Figure 26. Calculated heat fluxes for Day 33, Wangara from (a) moment-closure model, (b) three dimensional model (from Wyngaard and Cote, 1974).

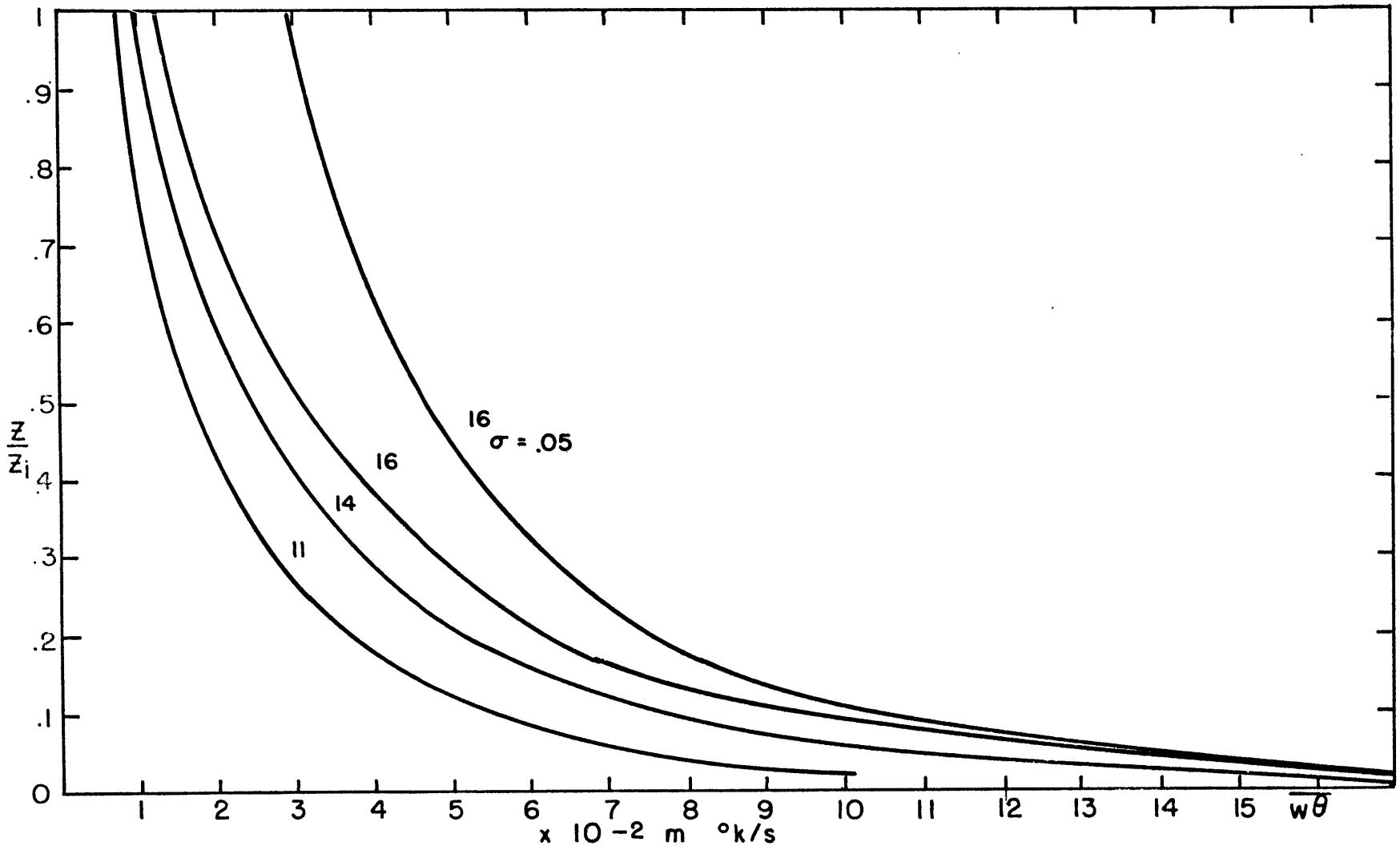

Figure 27. Plume model generated heat flux profiles for Day 33, Wangara.

of the surface layer to the inversion. Here, entrainment induces a negative (downward) heat flux as discussed in Chapter II(G). The ratio of the magnitude of the inversion to surface heat fluxes in the 3-D model is about 0.15. In order to ascertain this flux ratio and other relevant quantities at the inversion level, the values of derived quantities in Table 7 are required.

A comparison of the heat flux ratio between the models (Table 8) shows a remarkable agreement between m-c and the plume parameterization. The inversion rise rate, however, is quite exaggerated in the strong inversion limit. On the other hand, in the weak inversion limit there is no heat flux divergency contributed by the stable layer aloft such that the rise rate is too small.

The effect of this misrepresentation is likewise reflected in the inversion strength rate in Table 8. Part IV of the table indicates that the mean boundary layer heating rate is estimated well by equation (26) because the inversion heat flux is taken into account. An alternative reasonable representation of the mixed layer-inversion interface is suggested in a succeeding chapter.

B. Characteristics of Plume Variables

The predicted plume variables offer an estimate of the velocity, time, and space scales related to the major con-

TABLE 7

Input into the inversion rise rate equation from the plume model

	LST		
	1100	1400	1600
Stability above z_i, Γ (m^{-1})	9.4×10^{-5}	9.4×10^{-5}	9.4×10^{-5}
Potential Temperature below the inversion, θ_∞ (^oK)	282.2	284.0	285.0
Mean Time between successive plumes, t_* (sec)	862	443	435
Vertical plume velocity at z_i, w_p (m/s)	1.52	1.81	2.02

TABLE 8

Comparison of boundary layer heating rates

		LST		
		1100	1400	1600
I.	INVERSION/SURFACE Heat Flux Ratio			
	a. 3-D	0.15	0.15	0.15
	b. m-c	0.05	0.12	0.14
	c. Plume model	0.04	0.11	0.14
II.	INVERSION RISE RATE (m/hr)			
	a. 3-D	400 m/hr	100 m/hr	50 m/hr
	b. m-c	400 m/hr	105 m/hr	70 m/hr
	c. Plume model			
	strong inversion limit	209 m/hr	486 m/hr	550 m/hr
	weak inversion limit	14 m/hr	16 m/hr	17 m/hr
	d. observed	300 m/hr	70 m/hr	50 m/hr
III.	Rate of increase of temperature discontinuity at z_i (^{o}K/hr)			
	a. Plume model	5.1	12.4	14.1
	b. observed	0.5	0.5	0.5
IV.	Mean boundary layer heating rate (^{o}K/hr)			
	a. 3-D	0.60	0.66	0.51
	b. m-c	0.59	0.65	0.50
	c. Plume model	0.38	0.49	0.51
	d. observed	0.45	0.66	0.35

vective elements. Frisch and Businger (1973) conditionally sampled plumes in the surface layer. Their findings are plotted along with the normalized output of the plume model in Figure 28. For a given thermal stratification the vertical plume velocity increases and the plume temperature perturbation decreases linearly with height in the upper portion of the surface layer. Rapid acceleration and depletion occur simultaneously in the region of $0 < z < L$. The mean plume updraft increases steadily during the day (shown in Figures 29 and 30) from 1.44 m/s at 11 LST to 1.82 at 1600 LST midway through the mixed layer. The associated buoyancy variable, $S(\equiv \Theta_p/\bar{\Theta})$ decreases rapidly for $z < 0.2z_i$ and gradually in the upper mixed layer. The thermal elements rising in a slightly stable atmosphere retain a positive buoyancy due to the following closure assumption:

$$\frac{1}{\bar{\Theta}} \frac{\partial \bar{\Theta}}{\partial z} = S\sigma .$$

The surface layer plume model is capable of predicting the dimensions of the plumes at any level. In deep convection, however, the only restriction on individual plume area is that the fractional area covered by updrafts is constant with height or: $A_p = n a_p$.

If coalescence of thermals can be neglected then the number of plumes at various heights are related by:

$$\frac{n(z_1)}{n(z_2)} = \frac{w_p(z_2)}{w_p(z_1)}$$

This states that as the elements accelerate upward the

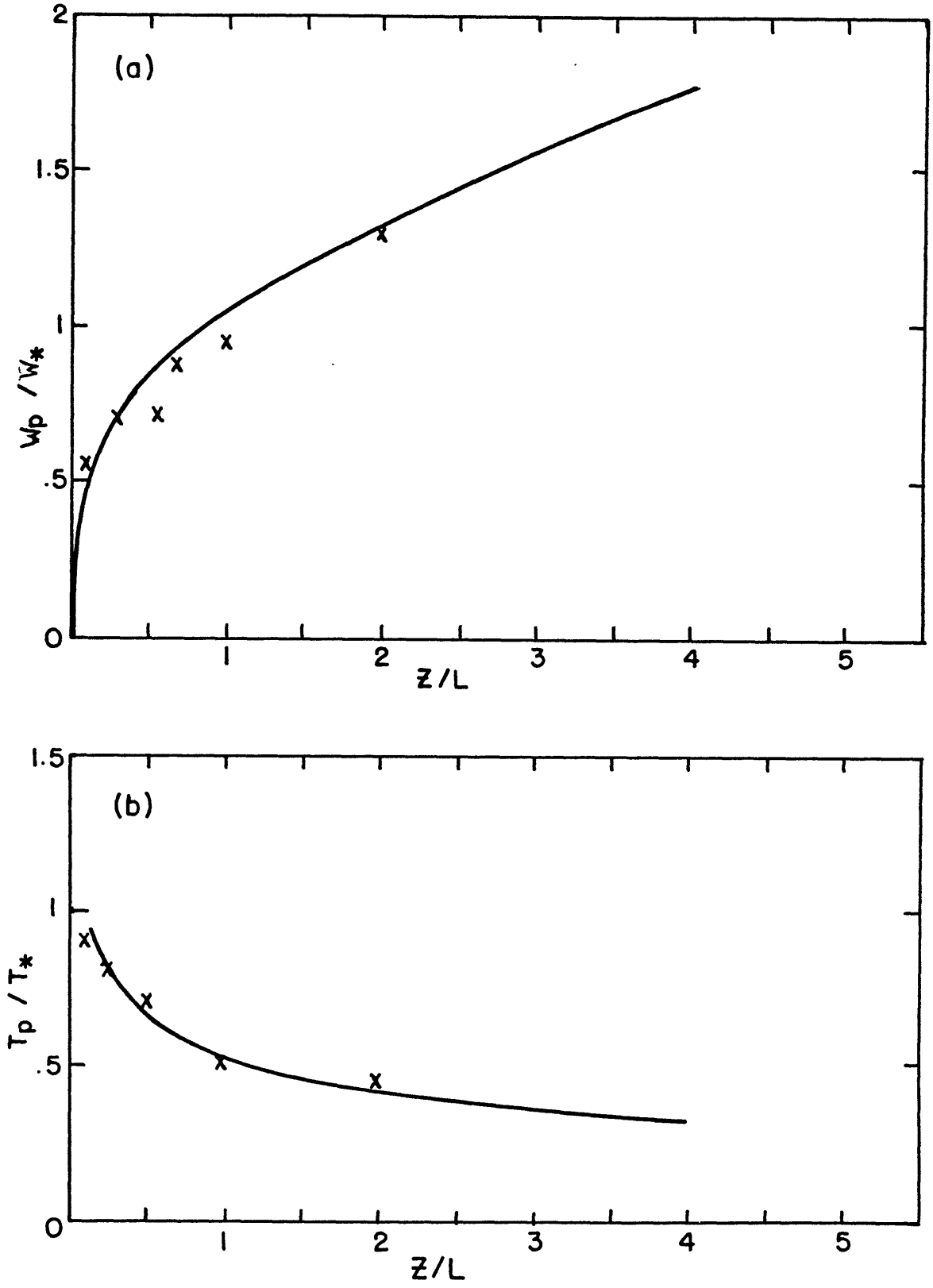

Figure 28. Comparison of normalized plume profiles of temperature (a) and vertical velocity (b) between surface layer plume model and data from Frisch and Businger, (1973), X's.

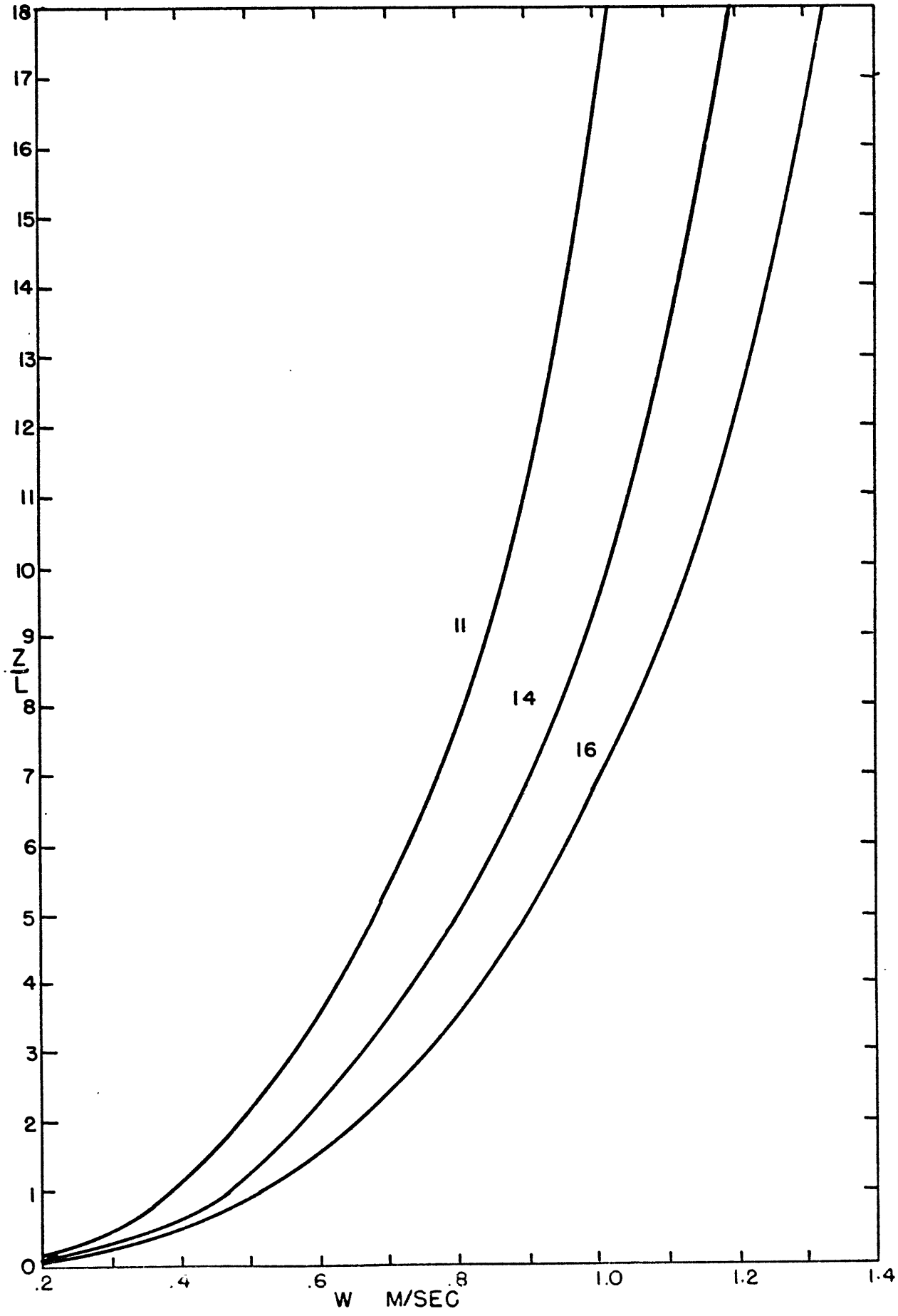

Figure 29.
a) Vertical plume velocity profiles near the surface for Day 33.

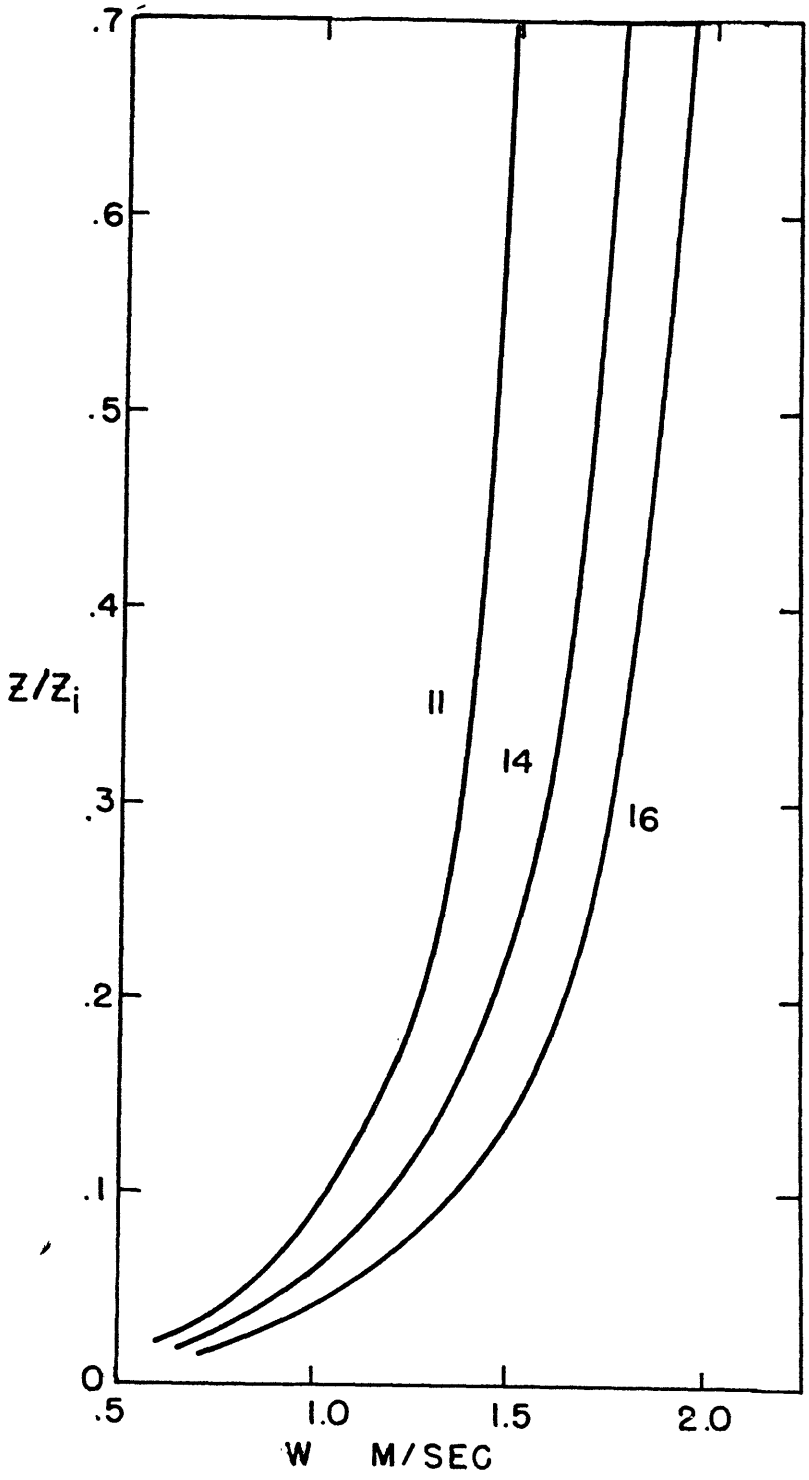

Figure 29.
b) Vertical plume velocity profiles for the mixed layer for Day 33.

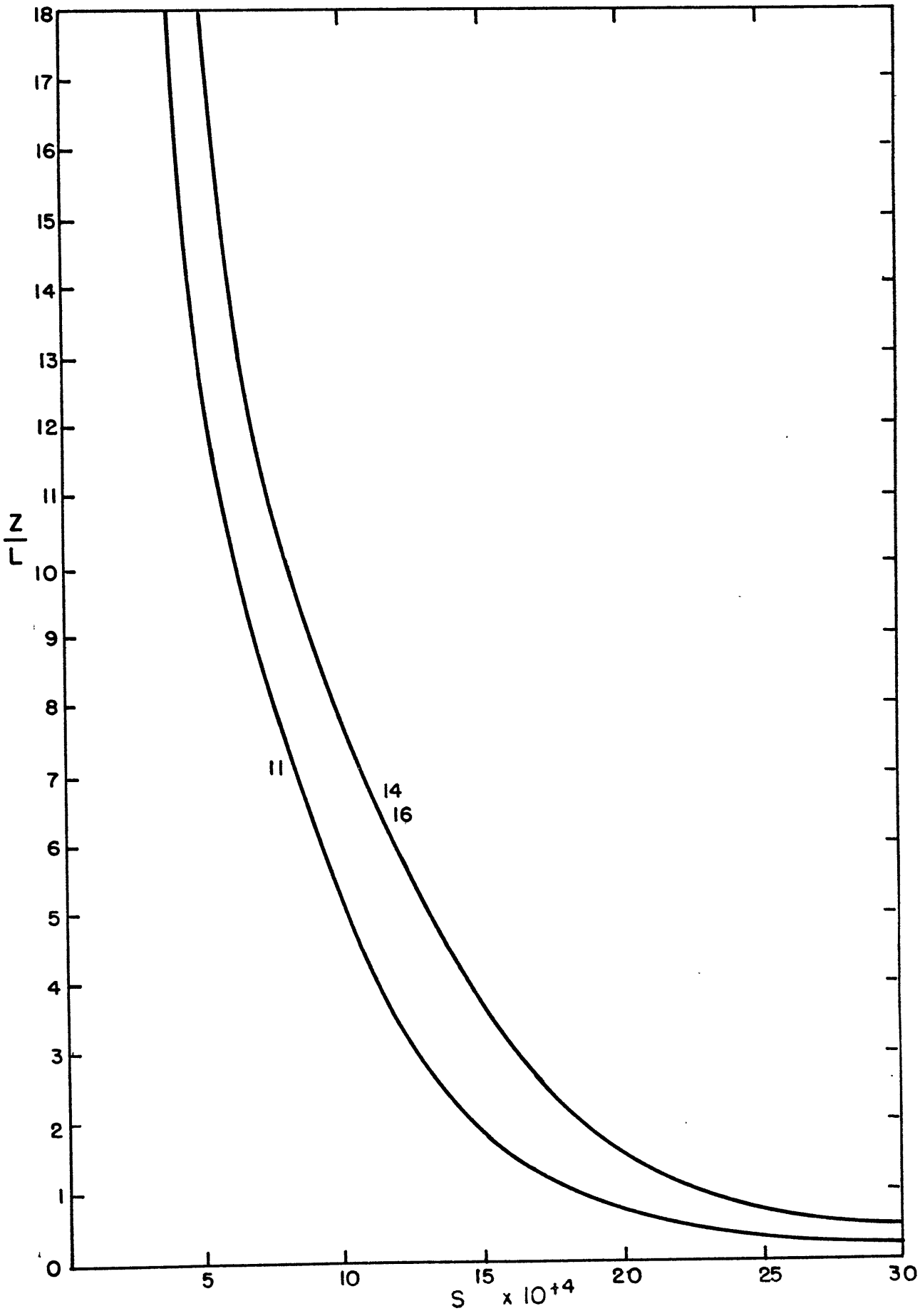

Figure 30.
a) Buoyancy factor, s, near the surface for Day 33.

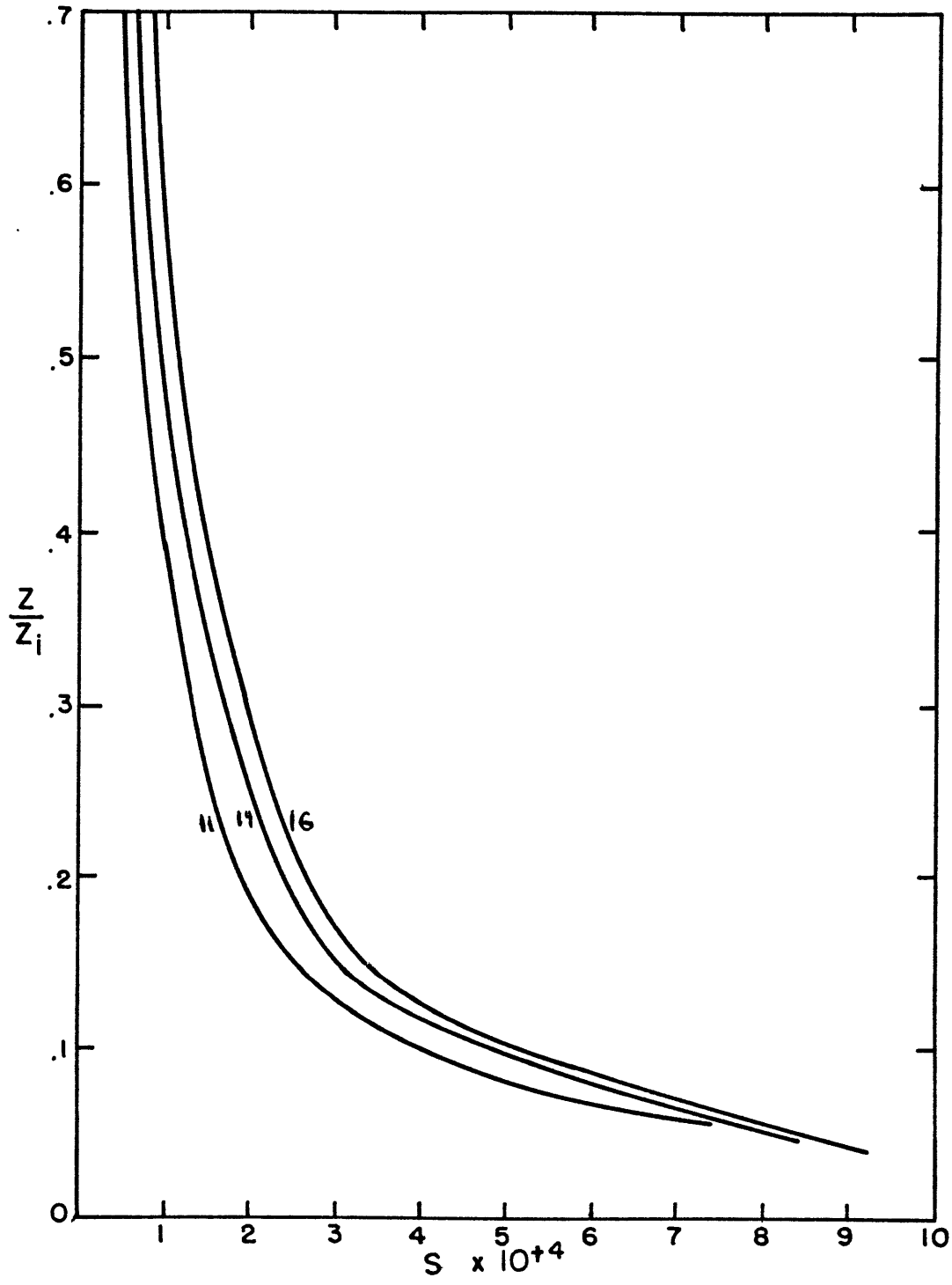

Figure 30.
b) Buoyancy factor, s, for the mixed layer.

residency time of successive levels decreases accordingly. The plume width shown in Figure 31 therefore increases rapidly near the surface where the effects of coalescence and acceleration combine,and at a slower rate in the mixed layer. That the scale of thermal turbulence varies with the Monin-Obukov length is based upon the assumption that the "plume formation zone" below a height $z=L/2$ maintains a constant aspect ratio. The plume translation speed and initial area and elongation along the shear stress vector at $z=L/2$ increase with time as shown in Table 9.

The plumes travel at the same rate as the mean flow in the lower mixed layer such that the motion of parcels within the plume is rearward. If a linear profile of longitudinal stress $\overline{uw}$ is assumed in the absence of thermal wind, then the shear profile becomes slightly curved as shown in Figure 32 when the geostrophic shear component is added. The related longitudinal velocity perturbation within the plume decreases rapidly with height. The transverse stress, $\overline{vw}$, is also distorted by the geostrophic shear (Figure 33). The related transverse perturbation velocities within the plume, although weaker than the longitudinal perturbations, are maximum in the middle of the mixed layer at 3 to 4 cm/s. Since the plumes are in the form of vertically elongated vortex rings (see Figure 6), the transverse velocity at the plume-environment boundary can be significantly larger than the mean plume velocity perturbation. Since wind variations and correlations

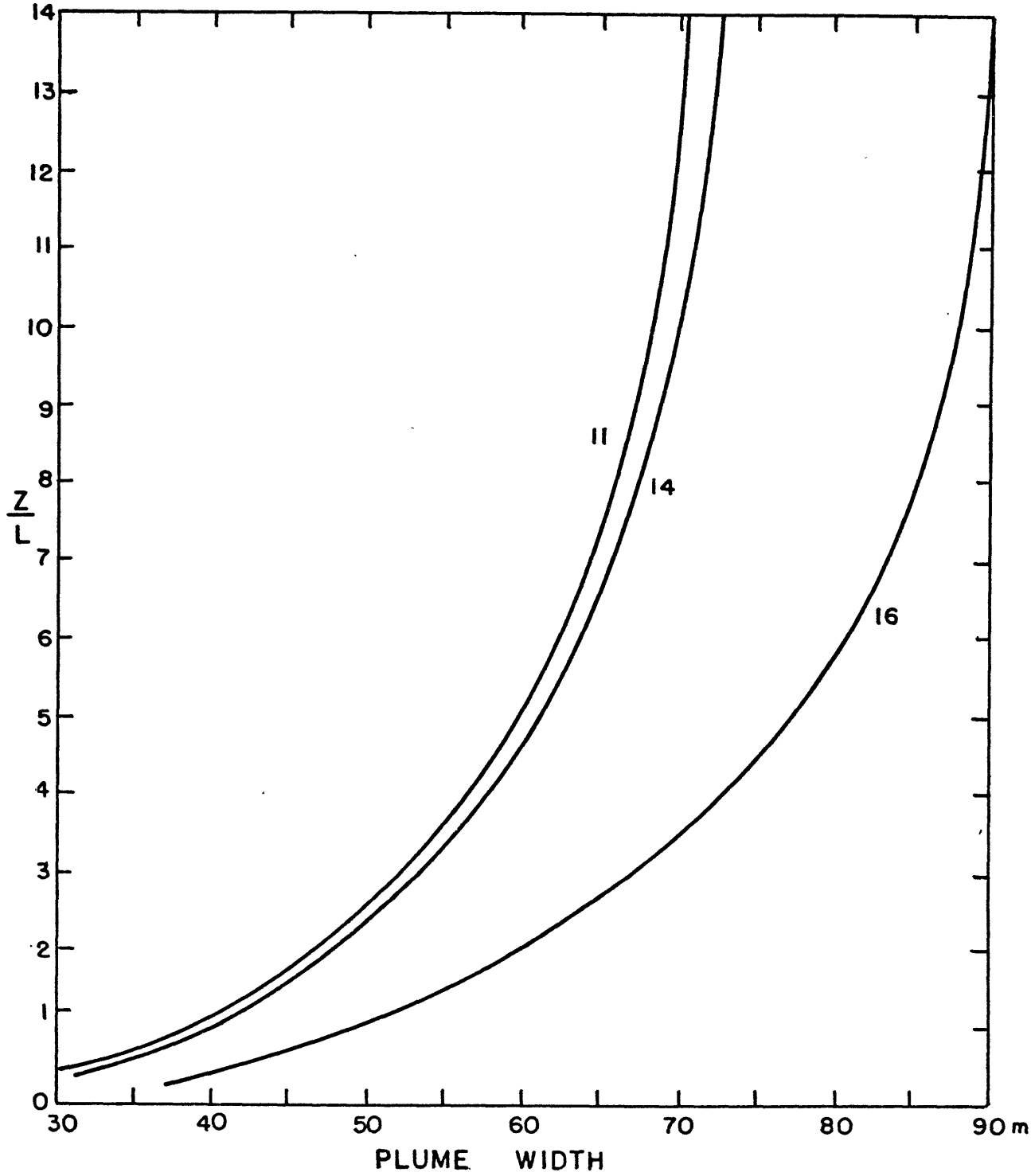

Figure 31. Profiles of plume width near the surface for Day 33.

TABLE 9

Plume characteristics at the formation height

	LST		
	1100	1400	1600
Relative plume translation speed, U_{tr} (m/s)	1.72	2.09	2.39
Eccentricity, r	1.516	1.627	1.717
Initial area, $a_{p\ L/2}$ (m^2)	2.53×10^3	2.9×10^3	4.78×10^3
Initial plume width, $b_{L/2}$ (m)	31.7	33.2	42

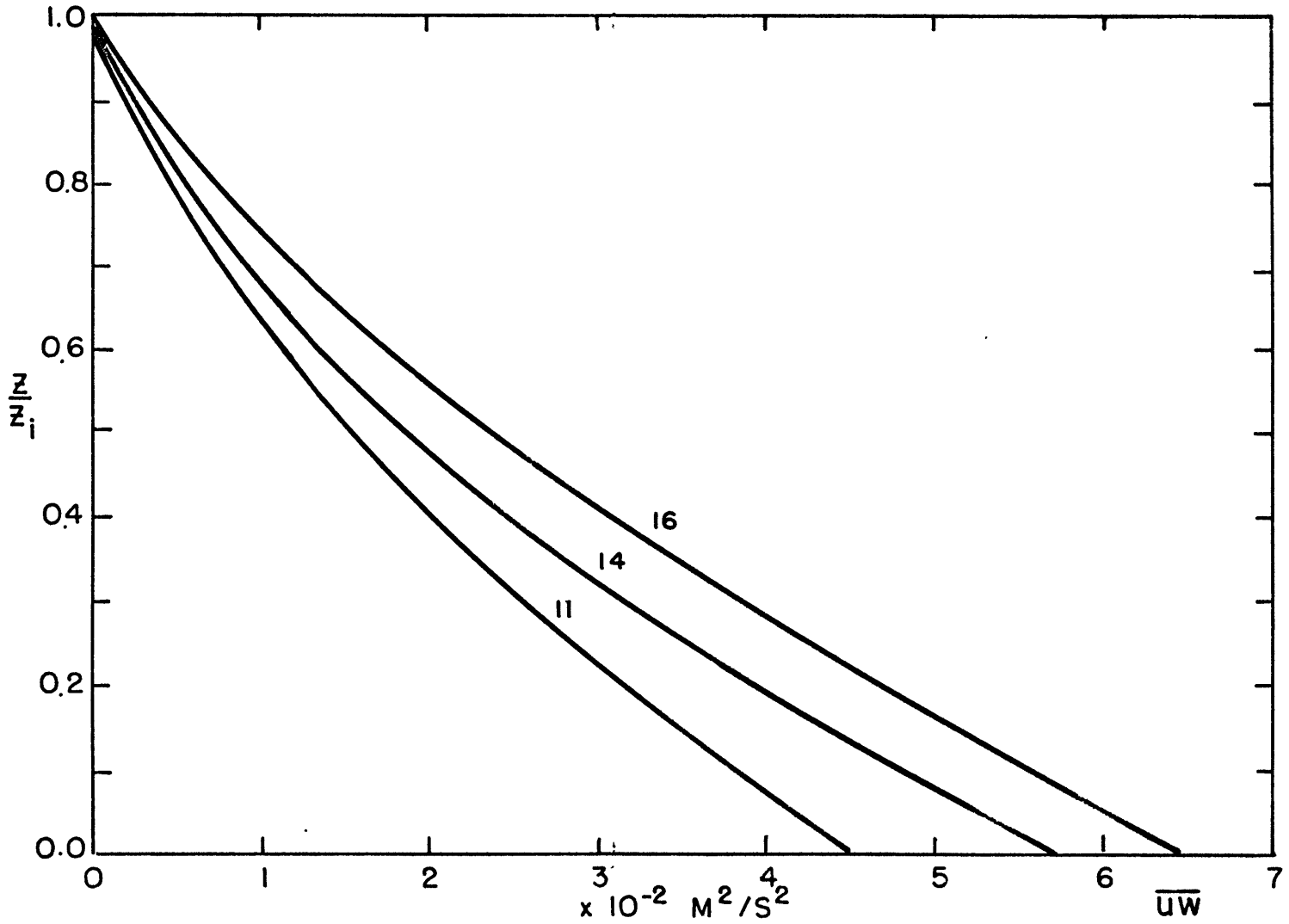

Figure 32. Model calculated longitudinal stress (uw) profile (using moment-closure parameterization) taking into account thermal wind for Day 33.

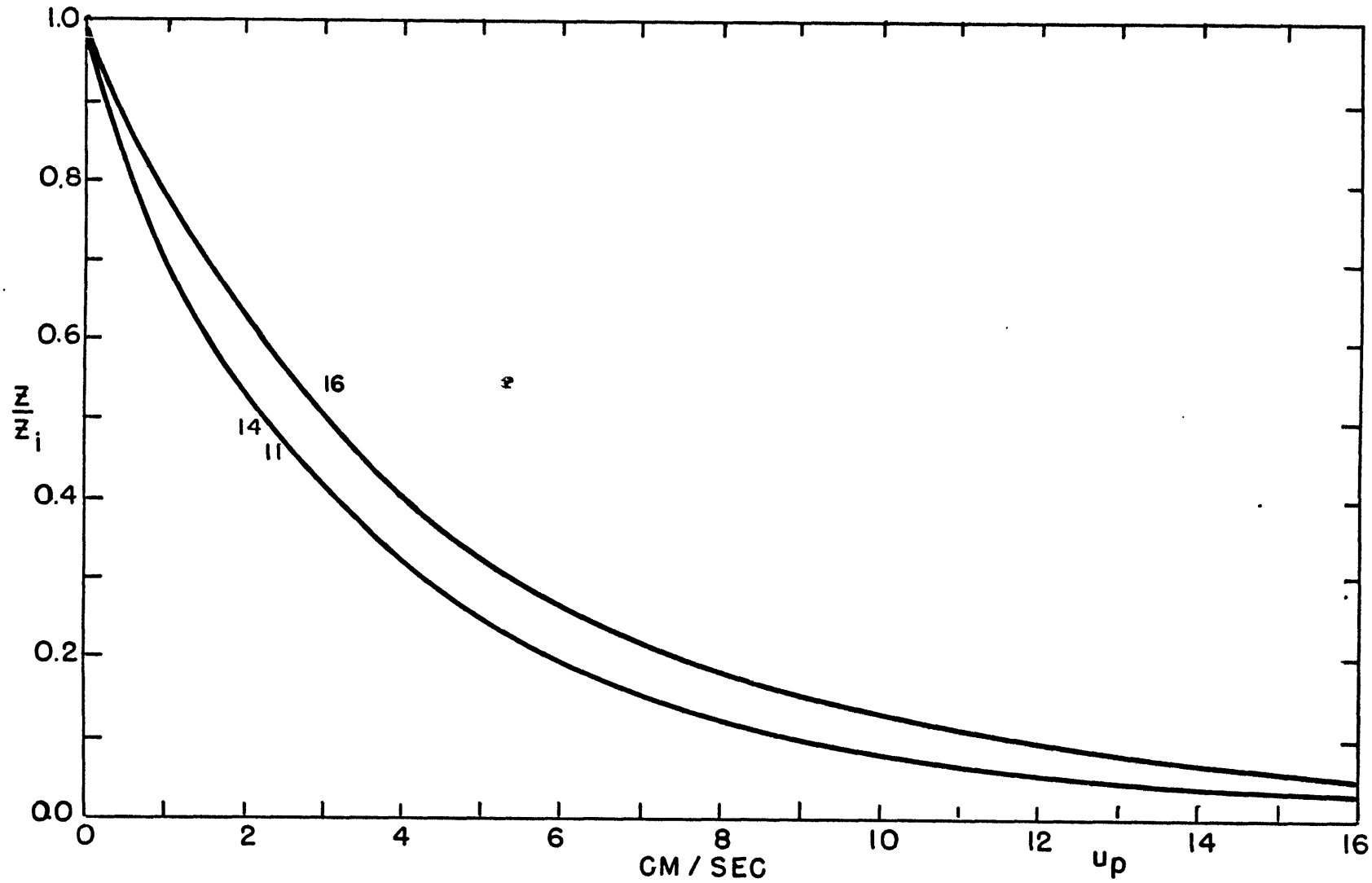

Figure 33. Mean plume longitudinal velocity, u_p, perturbation profile calculated from the stress profile in Figure 32.

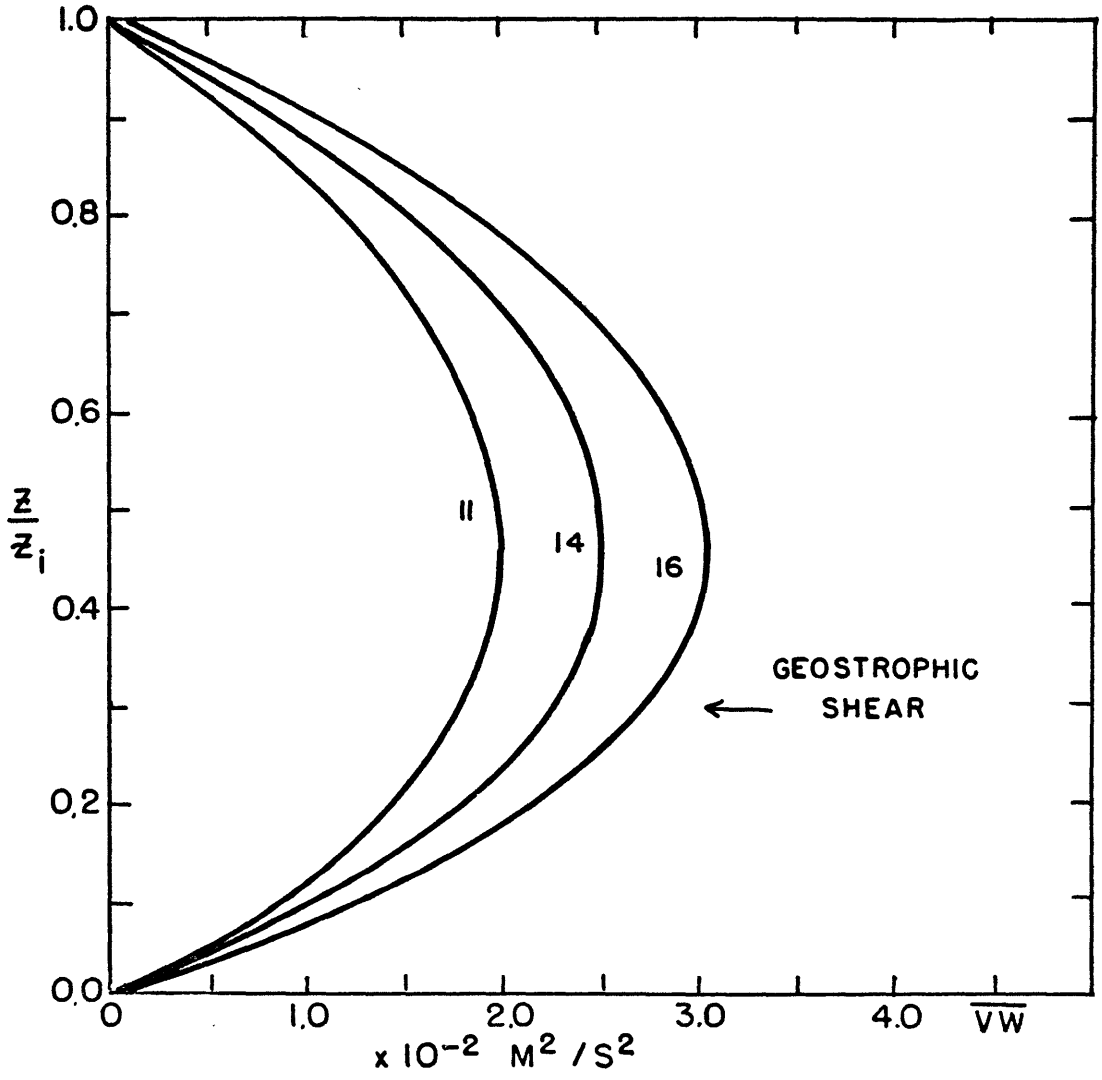

Figure 34. Model calculated transverse (vw) stress profile (using moment-closure parameterization) taking into account thermal wind for Day 33.

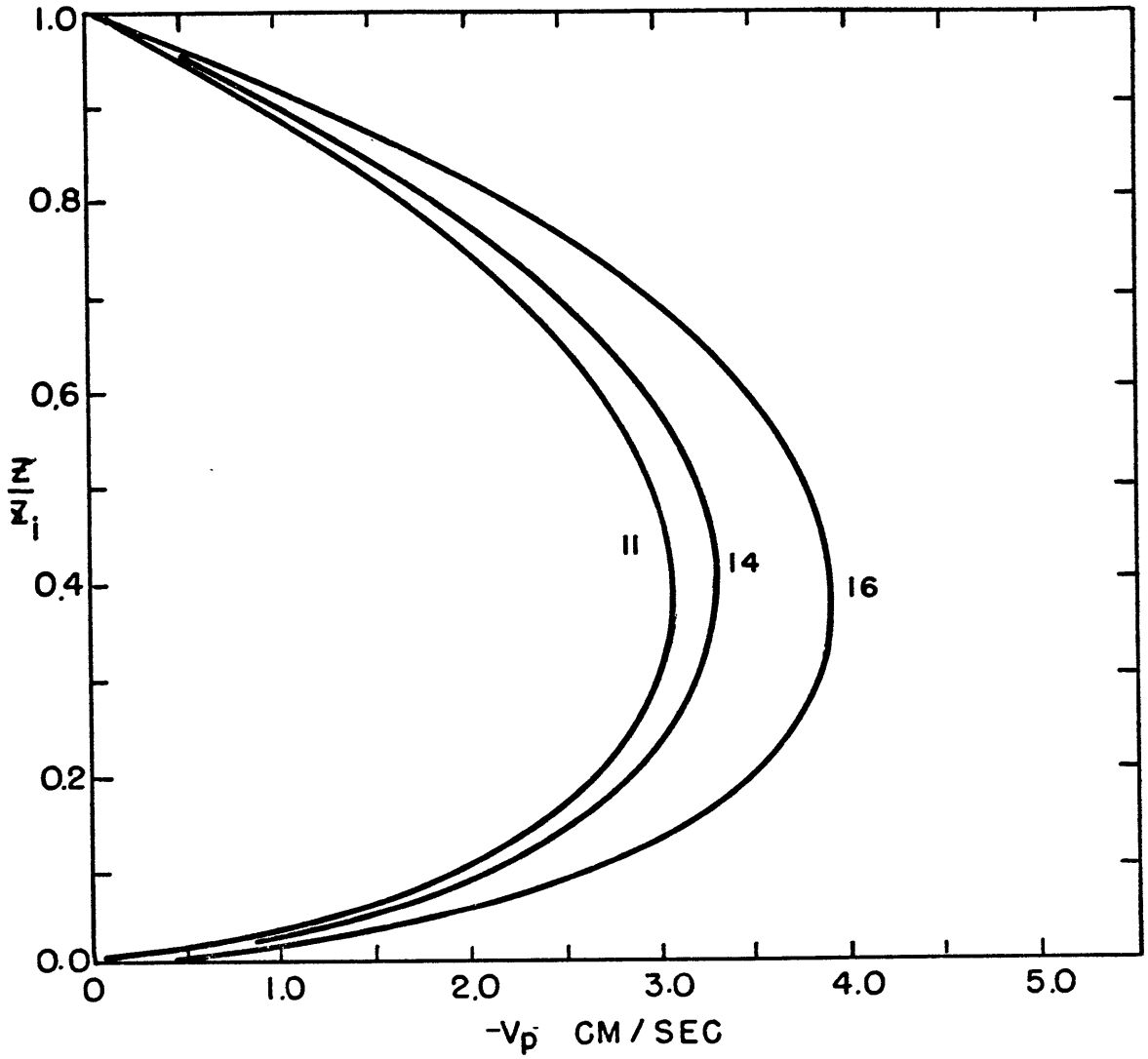

Figure 35. Mean plume transverse velocity perturbation profile calculated from the stress profile in Figure 34.

of such small magnitude are not easily measured, the direct comparison of $\overline{vw}$ with field observations is presently impractical.

The characteristic plume-scale motions in Deardorff's model range in width from 100 to 300 and lengths exceeding 600 meters. The buoyancy perturbations decrease rapidly with height. At z=0.5 km, updrafts exceeding 2 m/s accompany temperature perturbations exceeding $0.2^{o}K$. The profile of normalized vertical velocity variance (Figure 36) indicates that a maximum plume velocity occurs within the lower portion of the mixed layer in Deardorff's model. The plume model variances (based upon plume velocities), co-plotted in Figure 36, indicate an abrupt deceleration at the inversion. A portion of the decrease in the 3-D model variance may reflect a depletion of turbulent buoyant elements within the plume updrafts in the upper mixed layer. The normalized temperature variance (as the heat flux) decreases more rapidly with height than in the 3-D model. Figure 37 indicates that $\overline{\theta^2}$ is minimum at $z/z_i = 0.75$ where the mean heat flux is zero. Therefore, there is a background temperature variance whose net effect does not contribute to the vertical transport of heat. Because the plume model represents a single scale of motion, it is not possible to explicitly predict this background turbulence. The variance equation in terms of plume quantities can be written:

$$\overline{\theta^2} = \theta_p^2 A_p + (I_e - A_p)\theta_e^2 + \overline{\theta^2}_{background}$$

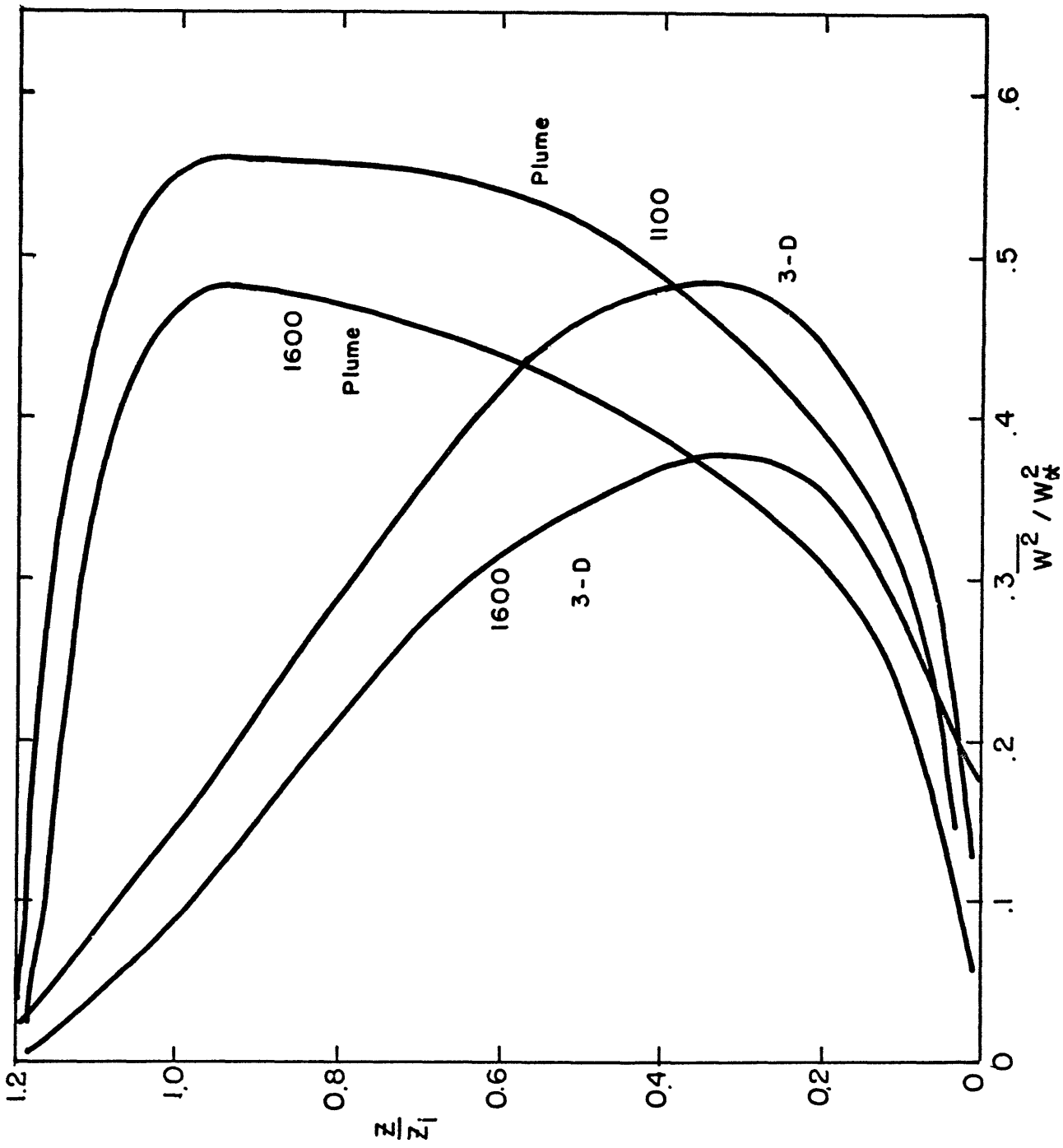

Figure 36. Profiles of normalized vertical velocity variance calculated from the plume and three dimensional models. ($w_* = (g\, u_* \theta_* z_i / \theta_0)$)

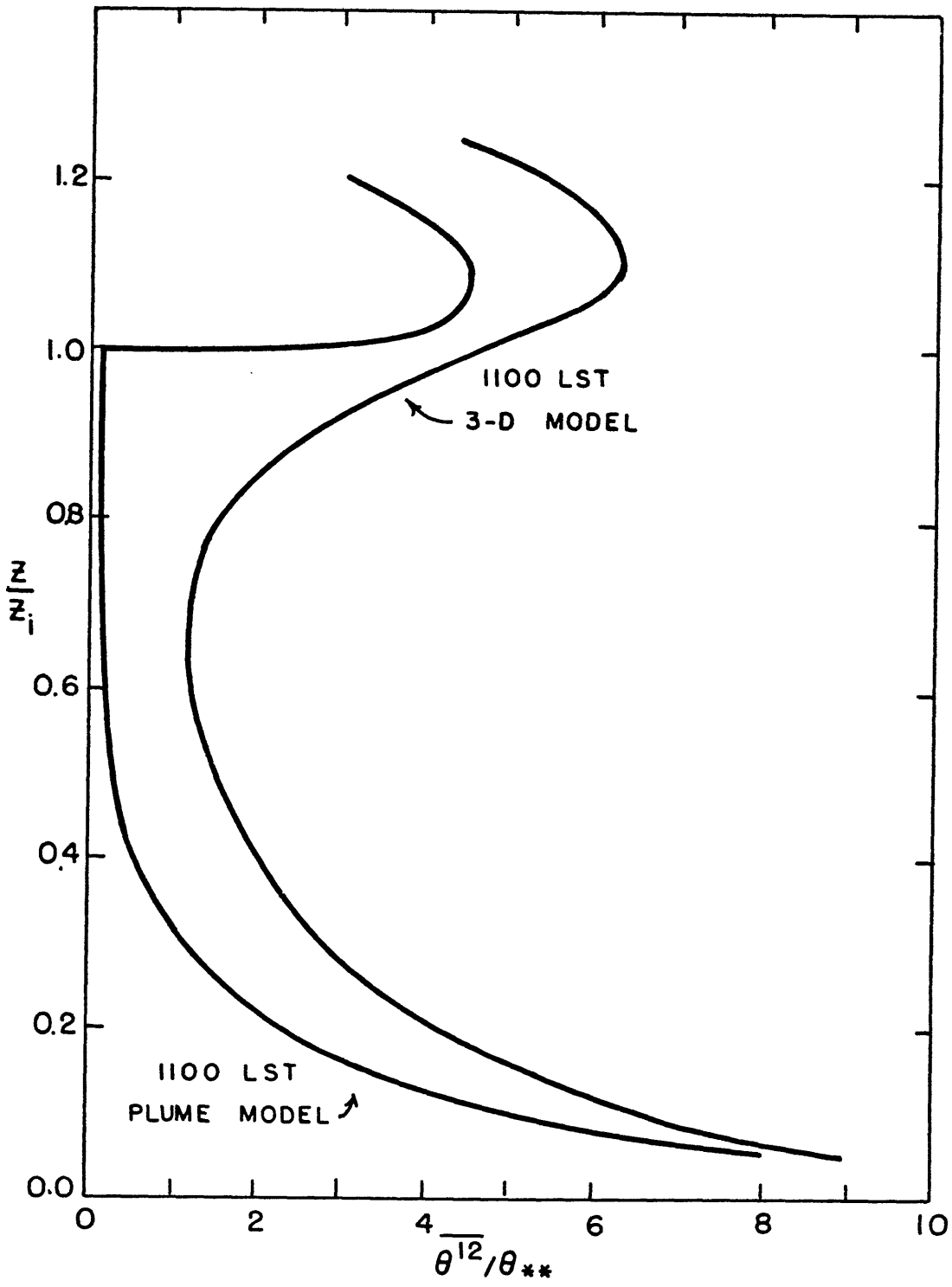

Figure 37. Profiles of normalized potential temperature variance calculated from the plume and three dimensional models. ($\theta_{**} = w_* \theta_* / w_*$)

where $\overline{\theta^2}_{bg}$ is a constant background variance. Letting $\overline{\theta^2}_{bg} = 1.6\ \theta_*^2$ in Figure 34 alligns the variance profiles to a satisfactory degree.

It is regretful that the evolution of the major eddies in the 3-D model is not discussed in detail by Deardorff (1974). The plume model computed time-scales of plume formation and residency at $z=L/2$ are shown in Table 10. The residency time decreases along with the time required to achieve the potential instability as the day passes. Because the convection becomes increasingly energetic during the day, the plumes achieve the same height when the surface available potential energy is depleted. The large aspect ratios confirm the contention of Manton (1975) that the plumes become elongated vertically in comparison to isolated thermals. Because of the conjectures that comprised the equations leading to Table 10, the magnitude and temporal variations are realistic although their accuracy is suspect. The parameters that comprise the plume model can be determined to a higher degree of confidence as the phenomenological aspects of convective turbulence continue to be studied.

TABLE 10

Temporal and Spatial Plume Scales

	LST		
	1100	1400	1600
Quiescent interplume period, t_*(sec)	862	443	435
Active plume period, t_d(sec)	388	334	290
Total plume period, (sec)	1250	777	725
Approximate maximum length of attached plume, H_p(m) at $t = t_*$	470	470	470
Approximate maximum aspect ratio of attached plume $H_p/b = 5$ at $t = t_*$	5	4.5	4

CHAPTER IV

DISCUSSION AND TENTATIVE CONCLUSIONS

In its present form the plume convection parameterization for thermally driven mixed layers has several shortcomings that merit discussion. That the representation, in terms of identical plumes is rather simplistic, however, is not a concern. The plume configuration is chosen at the onset as an expedient way to capture the most prominent physical characteristics of the observed turbulent elements.

There is no doubt that more funamental models based upon the equations of motion (Deardorff, 1974) or second order moment equations (Wyngaard and Cote', 1974) are capable of giving a less biased view of the turbulent motions. Such prognostic models are not likely candidates for boundary layer parameterizations but rather they are a means of simulating some aspects of a complex system. Their main utility is toward the development of diagnostic relations relating external parameters to highly derived quantities. In this regard, the use of moment-closure stress profiles that did not realistically account for the overlying inversion proved to be only marginally successful. That the geostrophic shear was not a major factor in determining the mean wind gives hope that a fairly straightforward stress parameterization can be formulated from the moment-closure type model.

The simplicity of the plume model will allow for

increasingly sophisticated alterations as merited through observations or numerical simulations. Improvements can be engineered so that the effects of the inevitable closure assumptions can be monitored. (In Deardorff's (1974) model diagnosis becomes impossible when every "run" is so resource consuming.) In particular, the relationship between the small scale fluctuations which produce the "saw-tooth" temporal traces and the plume scale motions represented by the "ramps" must become better understood. The interpretation of the plume field as an ensemble of turbulent elements of various sizes may be a worthwhile extension.

Before the model can be fine tuned, however, some glaring inadequacies must be confronted. In the quest for analytical solutions to the plume flux equations, an artificial closure assumption relating plume buoyancy and the lapse rate is employed. Plume velocity does approach an asymptotic limit within the mixed layer but the buoyancy decreases too rapidly below a level $z = 0.3z_i$ and too gradually above this level. This results in a non-constant vertical heat flux gradient that implies a too rapid destabilization of the lower mixed layer. One way to ameliorate this situation is to assign $\frac{1}{\theta}\frac{\partial \theta}{\partial z}$ equal to a specified function of height. The specification is determined by requiring that the heat flux profile be essentially linear. Similarity solutions most likely would no longer exist; a Runge-Kutta method would be used to numerically integrate the set of first order partial differential equations (12) upward

from the surface layer.

The negative heat flux in the present configuration is envisioned as appearing at the inversion height but not below. The dashed line in Figure 38 indicates the present interpretation of a nearly discontinuous heat flux profile. The heating rate ($-\frac{\partial}{\partial z}\overline{\omega\theta}$) is confined to the depth, $\mathcal{L}$, where the plumes decelerate (Figure 39) and lose their identity as they mix with the stable air aloft. In the new model, the air in the upper mixed layer is stabilized in response to the warm entrained air aloft. The rising plumes above a certain height become negatively buoyant and respond by decelerating before the inversion is approached. Therefore, the plume reaches the inversion with a somewhat reduced velocity so that the inversion rise rate calculated from equation (30) is more realistic. The numbered profiles of heat flux and vertical plume velocity in Figures 38 and 39 indicate that the idealized conceptualization of the present model is approached as the negative heat flux below the inversion decreases in magnitude.

It would be ideal if a theoretically justifiable closure for the static stability could be found that would lead to a closed form solution. Alternatively, the present model can be used for the lower mixed layer and joined to a model designed for the region of negative plume buoyancy in the upper mixed layer. The present model predicts the inversion heat flux ratio, Q_{z_i}, (Table 8(I)) with considerable skill. The upper model is started at a height of $z = 0.7z_i$ with

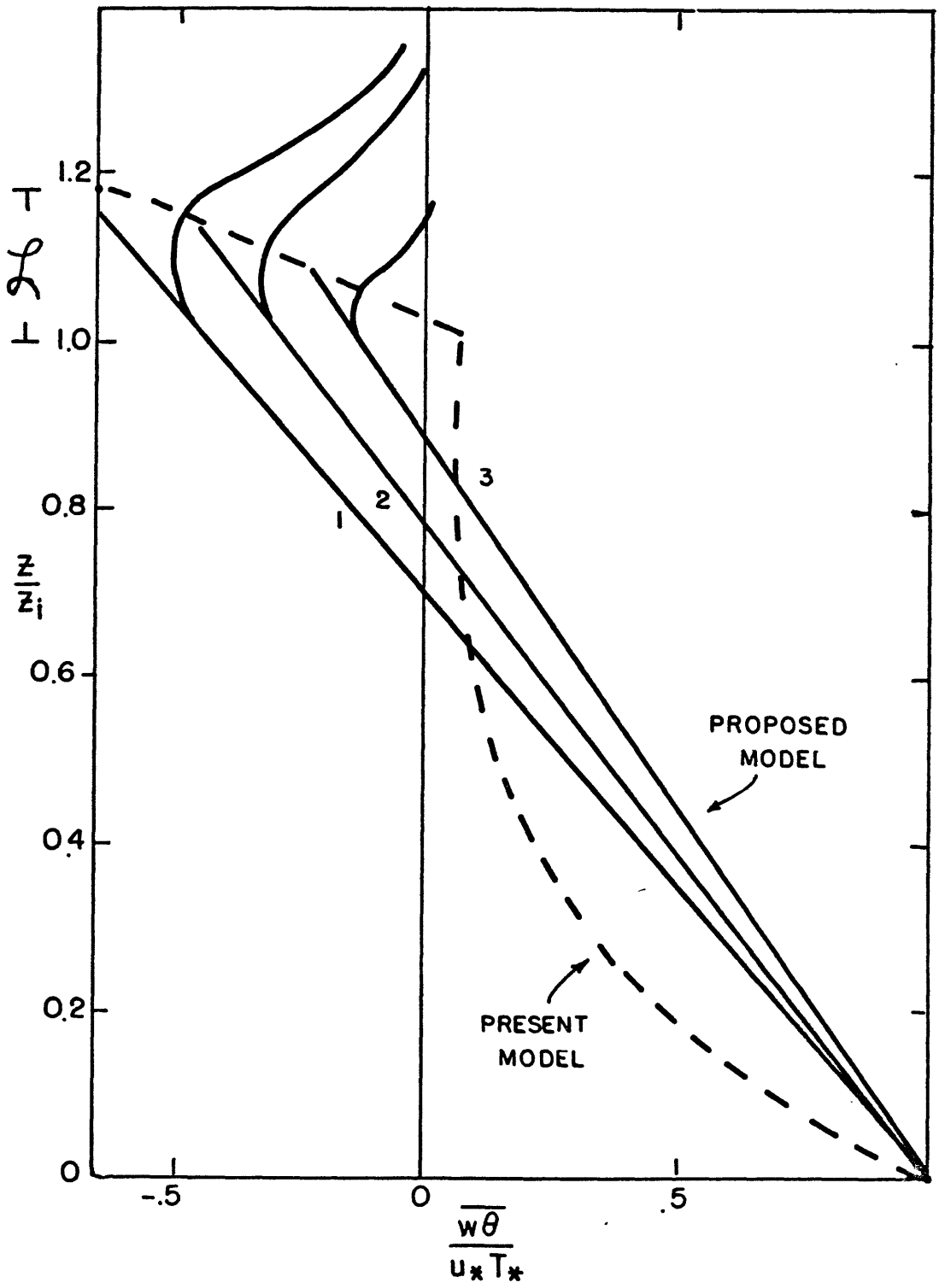

Figure 38. Comparison of normalized heat fluxes from the present and proposed model.
(1) large inversion heat flux ($|Q_H/Q_o| = 0.4$)
(2) moderate inversion heat flux ($|Q_H/Q_o| = 0.3$)
(3) small inversion heat flux ($|Q_H/Q_o| = 0.15$)

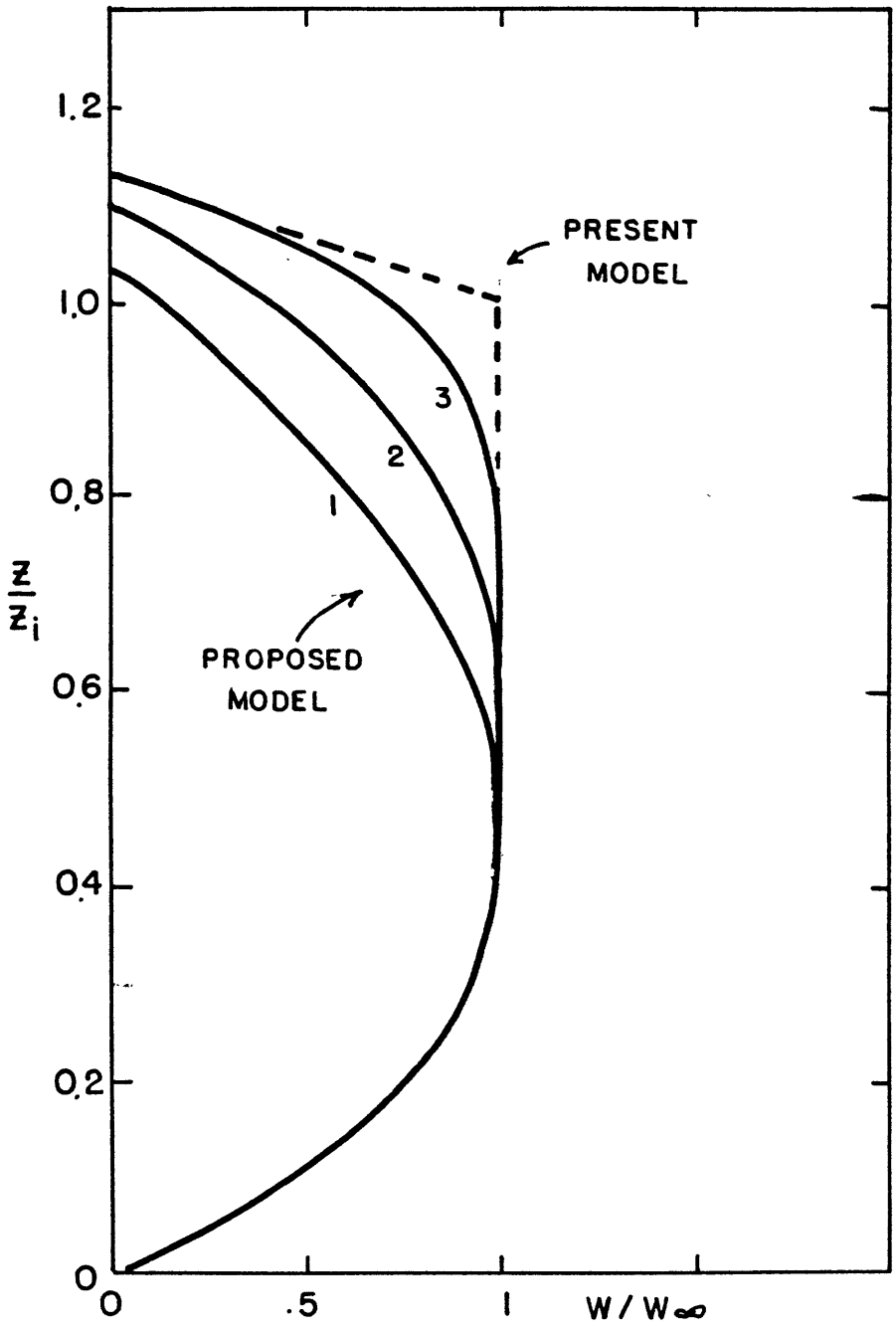

Figure 39. Same as Figure 38 but for vertical plume velocity.

an initial vertical velocity of $w_p(.7z_i)$ from the lower mixed layer solution. The initial buoyancy factor, s, in equation (12) gives a negative value that produces the desired heat flux at the top of the inversion layer. In order to avoid a mean unstable lapse rate the closure assumption is taken as $\frac{\partial \bar{\theta}}{\partial z} \propto -\bar{\theta}\sigma's$. A transition zone between the heights of $0.5z_i$ and $0.7z_i$ is constructed where the plume goes from positive to negative buoyancy. Figure 40 shows how the heat fluxes could be matched to form a nearly linear profile within the mixed layer.

Even in the absence of closed form solutions, the model is simple enough to be applied where there is interest in the nature of the turbulent elements. For instance, size, lifecycle, translation velocity and intensity of thermal plumes can provide a good measure of the dispersal of pollutants in an unstable boundary layer. The trajectories of pollutant "parcels" can be evaluated in a lagrangian framework as an array of intermittent plumes is advected over a point, line or area source.

To develop an operational convection parameterization model, much more testing and tuning is required to maximize its utility. There comes a point in the course of a complex numerical prediction model when the cost of enhancing the "accuracy" of a parameterization becomes too great. This model has potential because it is phenomenologically sound and requires few manipulations to obtain information about the turbulence and mean fields. The future in parameterizations lies in the combination

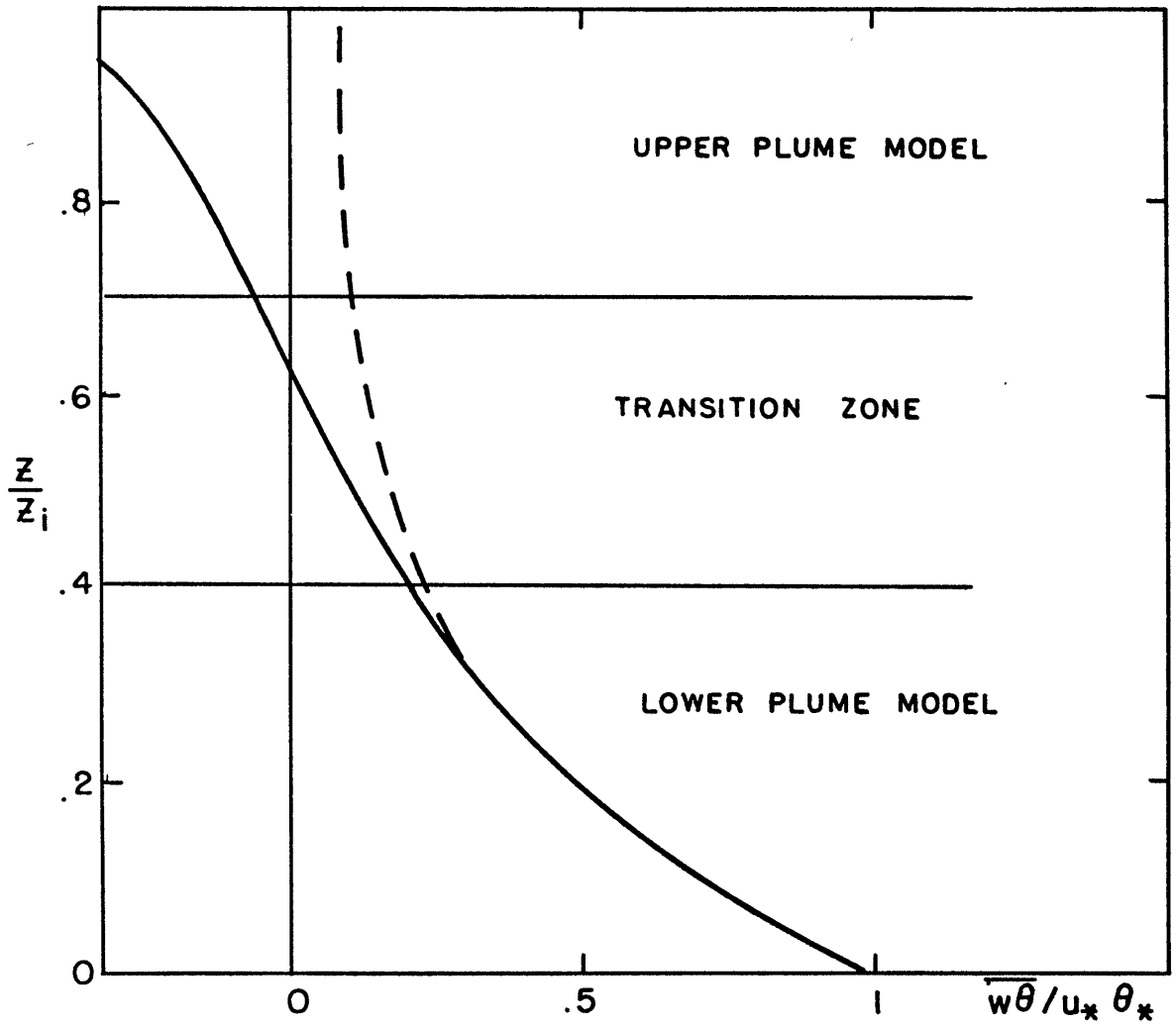

Figure 40. Heat flux profile for the linked analytic models (see text) for the lower and upper mixed layers.

of results from complex models with intuitive physical reasoning that the plume model exemplifies.

APPENDIX I

List of Symbols

SYMBOL	DEFINITION
a	Plume length
a_p	Plume cross-sectional area
A_p	Fractional plume area
A_p'	Effective fractional plume area
b	Plume width
c	Constants of variable assigned values
c_D	Drag coefficient
c_H	Heat transfer coefficients
D	Depth of the plume formation layer
D_1	Length scale for surface plume model
D_2	Length scale for mixed layer plume model
f	Coriolis force
f_o	Heat flux at $z=z_o$ between successive plumes
g	Gravitational acceleration
G	Magnitude of Geostrophic wind
I	Intermittency, I_e= effective intermittency
K	Effective mixing coefficient during plume activity
L	Negative of traditional Monin-Obukov length
n	Number density of plumes
$\mathscr{L}$	Plume inversion penetration depth
r	Plume shape, a/b
S	Normalized plume buoyancy perturbation
t_*	Interplume time interval
t_{act}	Plume residency time
T	$t_* + t_{act}$ plume cycle time
T'_b	Temperature perturbation at $z=0.1L$
T'_{bc}	Critical temperature perturbation
u_*	Friction velocity
U	Mean velocity parallel to surface stress
u	Longitudinal perturbation velocity
U_{tr}	Plume translation velocity
v	Transverse perturbation velocity
V	Mean velocity perpendicular to the surface stress
w	Vertical velocity
w_*	Buoyancy velocity
x	z/D_1
y	$(z - 4L)/D_2$
z	Geometric height above surface
z_s	Stagnation point height
z_i	Inversion height

SYMBOL	DEFINITION
$()_o$	Surface value
$()_p$	Plume quantity
$()_e$	Environmental quantity
$\overline{()}$	Horizontal plane ensemble average
$\overline{()}^z$	Total ensemble average
$()_g$	Geostrophic quantity
α	Stress gradient ratio at $z = L/2$
α_σ	Buoyancy depletion parameter
α_z	Mean lapse rate in formation zone
ϕ_*	Surface layer temperature scale
K_λ	Quiescent period mixing coefficient
σ	Thickness of convergence zone
λ	Buoyancy closure parameter
β	Effective conductivity at surface
$\Delta U, \Delta V$	Effective intermittency parameter
ρ	Thermal wind components
θ	Virtual potential density
ϕ_{ij}	Virtual potential temperature
Δ	Turbulence modulation factors
τ_i	Inversion strength
	Inversion penetration time

BIBLIOGRAPHY

Antonia, R.A., 1977: Similarity of atmospheric Reynold's shear stress and heat flux fluctuations over a rough surface. Boundary Layer Meteor., 12, 351-364.

Asai, T., 1970: Stability of a plane parallel flow with variable vertical shear and unstable stratification. J. Meteor. Soc. Japan, 48, 129-139.

Chiba, A., 1976: The scale of turbulence in the atmospheric surface layer. J. Meteor. Soc. Japan, 54, 187-190.

Clarke, R. et. al., 1971: The Wangara experiment: boundary layer data. Paper no. 19, Div. of Meteor. Physics, CISRO, Australia.

Davison, D., 1974: The translation velocity of convective plumes. Quart. J. Roy. Meteor. Soc., 100, 572-592.

Davison, D., 1975: The horizontal cross-sectional shape of convective plumes. Quart. J. Roy. Meteor. Soc., 101, 463-473.

Deardorff, J.W., 1974 a: Three-dimensional numerical study of the height and mean structure of a heated planetary boundary layer. Boundary Layer Meteor., 7, 81-106.

Deardorff, J.W., 1974: Three-dimensional numerical study of turbulence in an entraining mixed layer. Boundary Layer Meteor., 7, 363-372.

Donaldson, C.P., 1973: Construction of a dynamic model of the production of atmospheric turbulence and the dispersal of atmospheric pollutants. In: Workshop of Micrometeorology, Haugen, D., Ed., Amer. Meteor. Soc., 392 pp.

Falco, R.E., 1977: Coherent motions in the outer region of turbulent boundary layers, Phys. Fluids, 20, S 124-132.

Farmer, D.M., 1975: Penetrative convection in the absence of a mean shear. Quart. J. Roy. Meteor. Soc., 101, 869-891.

Frisch, A.S. and J. Businger, 1973: A study of convective elements in the atmospheric surface layer. Boundary Layer Meteor., 3, 317-328.

Frisch, A.S. et. al., 1976: Observations of boundary layer convection cells. Boundary Layer Meteor., 10, 65-83.

Frisch,A.S. and J. Bussinger, 1973: A study of convective elements in the atmospheric surface layer. Boundary Layer Meteor., 3, 317-328.

Garrat, J.R., 1978: Transfer characteristics of a heterogeneous surface of large aerodynamic roughness. Quart. J. Roy. Meteor. Soc., 104, 491-502.

Hall,F. et al, 1975: Convective plumes in the planetary boundary layer investigated with an acoustic sounder. J. Appl. Meteor., 14, 513-523.

Haugen, D. A. , Ed., 1973: Workshop on Micrometeorology, Amer. Meteor. Soc., 392 pp.

Howard, L.N., 1964: On turbulent convection above a heated surface. In: Proceedings of the Eleventh International Congress of Applied Mechanics, Munich, ed. H. Gortler, 1109-1115.

Jackson,R.G., 1976: Sedimentological and fluid dynamic implications of the turbulent bursting phenomena in geophysical flows. J. Fluid Mech., 77, 555-575.

Kaimal, J.C. , 1978: Horizontal velocity spectra in an unstable surface layer. J. Atmos. Sci., 35, 18-24.

Kaimal, J. and J. Businger, 1970: Case studies of a convective plume and a dust devil. J. Appl. Meteor., 9, 612-620.

Khalsa,S. and J. Businger, 1977: The drag coefficient as determined by the dissipation methos and its relation to intermittent convection in the surface layer. Boundary Layer Meteor. , 12, 273-298.

Konrad,J.G., 1970: The dynamics of the convective prosesses in clear air as seen by radar. J. Atmos. Sci., 27,1138-1147.

Kuo, H.L. and W. Y. Sun, 1976: Convection in the lower atmosphere and its effects. J. Atmos. Sci., 33, 21-40.

LeMone, M.A., 1976: Modulation of turbulence energy by longitudinal rolls in an unstable planetary boundary layer. J. Atmos. Sci., 31, 465-474.

Lenschow, D.H., 1970: Airplane measurements of planetary boundary structure. J. Appl. Meteor., 9, 874-884.

Manton, M.J. , 1975: Penetrative convection due to a field of thermals. J. Atmos. Sci., 32, 2272-2277.

Manton, M.J., 1977: On the structure of convection. Boundary Layer Meteor. , 12, 491-503.

Manton, M.J., 1976: On the structure of free convection near the surface. Boundary Layer Meteor., 10, 345-358.

Monji,N., 1973: Budgets of turbulent energy and temperature variance in the transition zone from forced to free convection. J. Meteor. Soc. Japan, 51, 133-145.

Monji, N., 1975: Characteristics of the horizontal wind fluctuations in the surface layer under strong convective conditions. J. Meteor. Soc. Japan, 53, 99-102.

Morton, J., G. Taylor and B. Turner, 1956: Turbulent gravitational convection from maintained and instantaneous sources. Proc. Roy. Soc. (A), 234, 1-23.

Offen, G.R. and S. Kline, 1974: Combined dye-streak and hydrogen-bubble visual observations of turbulent boundary layer. J. Fluid Mech., 62, 223-239.

Pennel,W. and M. Le Mone, 1974: An experimental study of turbulence s-ructure in the fair-weather trade wind boundary layer. J. Atmos. Sci., 31, 1308-1323.

Perry, A.E. and P.H. Hoffman, 1976: An experimental study of turbulent convective heat transfer from a flat plate. J. Fluid Mech. , 77, 355-368.

Priestly,C.H., 1959: Turbulent Transfer in the Lower Atmosphere. Univ. of Chicago Press, 130 pp.

Pshenay-Severin, 1970: Model of the acculation and redistribution of thermal energy in an atmospheric layer. Dokl. Akad. Nauk. SSSR, 193, 13-16.

Randall, David, 1976: The Interaction of the Planetary Boundary Layer with Large-Scale Circulations, PhD Thesis, U.C.L.A., 247 pp.

Sreenivasan, K.R. and R.A. Antonia, 1977: Skewness of temperature derivatives in turbulent shear flows. Phs. Fluids, 20, 1986-1988.

Stuart, D., 1977: A numerical investigation of layer cloud instability, S.M. Thesis, M.I.T., Cambridge, Mass. 115 pp.

Stull, R.M., 1976: Mixed layer depth model based on turbulent energetics, J. Atmos. Sci., 33, 1268-1278.

Telford, J., 1970: Convective plumes in a convective field, J. Atmos. Sci., 27, 347-358.

Tennekes, H., 1973: Similarity Laws and scale relations in planetary boundary layers, In: Workshop on Micrometeorology, D. Haugen, Ed., Amer. Meteor. Soc., 392 pp.

Townsend, A.A., 1972: Mixed convection over a heated horizontal plane, J. Fluid Mech., 55, 209-227.

Warner, J. and J. Telford, 1967: Convection below cloud base, J. Atmos. Sci., 24, 374-382.

Willmarth, W. and T. Boger, 1977: Survey and new measurements of turbulent structure near the wall. Phys. Fluids 23, S 509-521.

Willis, G.E. and J.W. Deardorff, 1974: A laboratory model of the unstable planetary boundary layer, J. Atmos. Sci., 31, 1297-1307.

Wyngaard, J.C., S. Arya, and O. Cote, 1974: Some aspects of the structure of convective planetary boundary layers, J. Atmos. Sci., 31, 747-754.

Yamada, T. and G. Mellor, 1975: A simulation of the Wangara atmospheric boundary layer data, J. Atmos. Sci., 32, 2309 2329.

Zilitinkevich, S.S., 1973: Shear convection, Boundary Layer Met., 3, 418-423.